The Pennsylvania State University
The Graduate School

ENHANCEMENTS TO THE FLOQUET METHOD FOR ANALYSIS AND DESIGN OF POWER CONVERTER SYSTEMS

A Dissertation in
Electrical Engineering
by
Mu He

Submitted in Partial Fulfillment
of the Requirements
for the Degree of

Doctor of Philosophy

August 2016

The dissertation of Mu He was reviewed and approved* by the following:

Jeffrey Mayer
Associate Professor of Electrical Engineering
Dissertation Advisor
Chair of Committee

Constantino Lagoa
Professor of Electrical Engineering

Minghui Zhu
Dorothy Quiggle Assistant Professor of Electrical Engineering

Alok Sinha
Professor of Mechanical Engineering

Victor Pasko
Professor of Electrical Engineering
Graduate Program Coordinator

*Signatures are on file in the Graduate School.

Abstract

Switch-mode power converters provide critical infrastructure for most electronic systems. As infrastructure, there are stringent demands to minimize cost and maximize performance. These conflicting goals increasingly require methods of analysis and design that are more sophisticated than conventional linear system techniques and serial design of converter subsystems. For example, linear small signal models fail to predict sub-harmonic oscillations that arise under certain operating conditions.

Most power converter systems can be modeled using a switched state space model that includes piecewise linear time invariant (LTI) state space models for each topology along with a set of switching surfaces. In addition, most converters operate in a periodic manner, so the Floquet method can be applied to assess stability. Previous work yielded a closed-form expression for the Floquet-theoretic monodromy matrix for a piecewise LTI system with piecewise constant inputs. It also provided a method for calculating the periodic steady state response of such a system. The work presented here extends the previous derivation and method to systems having multi-period behavior (sub-harmonics) and sinusoidal inputs. This permits calculation of frequency response characteristics that are more accurate than those that can be obtained from small signal models.

Tradeoffs are inevitable when one designs power converter systems. Decreasing the size of the energy storage elements - inductors and capacitors - reduces cost and volume but also reduces steady-state and transient power quality margins in ways that are difficult to determine using conventional models. To minimize cost and volume while ensuring that power quality specifications are satisfied, an automated design process based on Genetic Algorithms and extended Floquet method is presented.

Table of Contents

List of Figures viii

List of Tables x

Acknowledgments xi

Chapter 1
Introduction 1
1.1 Motivation 1
1.2 Research Contributions and Organization of Dissertation 4

Chapter 2
Power Converter System Dynamics and Modeling 6
2.1 Power Converter System Dynamics 6
2.1.1 Principle of Operation 6
2.1.2 Complexity of Dynamics 8
2.1.3 Feedback Control 11
2.1.4 Input Filter 13
2.2 Power Converter System Modeling 15
2.2.1 Switched State Space Model 16
2.2.2 Linear Continuous-Time Model (Small Signal Model) 17
2.2.3 Nonlinear Discrete-Time Model (Large Signal Model) 20
2.2.4 Periodic Steady State Model 21
2.3 Example of a Modeling of Buck Converter System 28
2.3.1 Switched State Space Model 29
2.3.2 Switching Surfaces 31

Chapter 3
Background of Design Optimization of Power Converter Systems 33
3.1 Classical Optimization Techniques . . . 35
3.2 Genetic Algorithms Technique . . . 36
3.2.1 Population Representation and Initialization . . . 37
3.2.2 Fitness Evaluation . . . 37
3.2.3 Population Reproduction . . . 38
3.2.4 Termination of Genetic Algorithms . . . 40
3.3 Discussion . . . 40

Chapter 4
Enhancements to Floquet Method for Power Converter System Analysis 42
4.1 Multi-period Solver . . . 42
4.1.1 Derivation . . . 43
4.2 Extension to Sinusoidal Inputs . . . 47
4.2.1 Redefined Poincaré Map . . . 47
4.2.2 Redefined Periodic Steady State Model . . . 49
4.2.3 Closed-Form Expressions for Zero-State Response to Bohl-type Inputs . . . 52
4.3 Results . . . 56
4.3.1 Frequency Response . . . 57
4.3.2 Exact Frequency Response at Harmonics and Sub-harmonics 60
4.4 Summary . . . 62

Chapter 5
Optimal Design of Power Converter Systems 64
5.1 Power Converter System Design Considerations . . . 64
5.1.1 Power Stage Design . . . 65
5.1.2 Compensator Design . . . 69
5.1.3 Input Filter Design . . . 71
5.2 Automated Design Process . . . 73
5.2.1 Objective Function . . . 74
5.2.2 Formulation of Optimization Problem . . . 77
5.2.3 Solution of the Optimization Problem using Genetic Algorithms . . . 79
5.3 Conventional Design Process . . . 82
5.3.1 Power Stage Design . . . 82
5.3.2 Compensator Design . . . 83
5.3.3 Input Filter Design . . . 84

5.3.4 Optimization Results using Conventional Design Process . . 86
5.4 Design of Boost and Buck-Boost Converter by Automated Design Process 88
5.4.1 Right-Half-Plane Zero 88
5.4.2 Results of Automated Design Process 88
5.5 Summary 91

Chapter 6
Conclusions and Future Work **93**
6.1 Summary 93
6.2 Future Work 95

Appendix A
Derivation of Closed-Form Expressions for Zero-State Response to Bohl-type Inputs **97**

Appendix B
Parameter Values of Power Converter Systems **100**

Appendix C
Transfer Functions of Current-mode Controlled dc-to-dc Converter **101**
C.1 Transfer Function of Current-mode Control for Boost Converter . . 101
C.2 Transfer Function of Current-mode Control for Buck-Boost Converter 102

Appendix D
Inductor Core and Capacitor Data **103**

Appendix E
Switched State Space Model of Power Converter Systems **105**
E.1 Switched State Space Model of Buck Converter Systems with Input Filter 105
E.1.1 Closed-loop Piecewise-LTI Model 106
E.1.2 Switching Surfaces 107
E.2 Switched State Space Model of Boost Converter Systems with Input Filter 108
E.2.1 Closed-loop Piecewise-LTI Model 109
E.2.2 Switching Surfaces 110
E.3 Switched State Space Model of Buck-Boost Converter Systems with Input Filter 110
E.3.1 Closed-loop Piecewise-LTI Model 112

E.3.2 Switching Surfaces 113

Bibliography **114**

List of Figures

1.1 Conventional design process. 2
1.2 Automated design process. 3

2.1 Buck converter system. 7
2.2 Typical periodic steady state waveforms of buck converter operating in continuous conduction mode. 7
2.3 Typical periodic steady state waveforms of buck converter operating in discontinuous conduction mode. 9
2.4 Transient response of buck converter to a step change in V_o^{ref} from 1 V to 1.3 V. 10
2.5 Voltage-mode control for buck converter. 11
2.6 Current-mode control for buck converter. 12
2.7 Current-mode control for buck converter with an input filter. 13
2.8 LC input filter loaded by equivalent input resistance of dc-to-dc converter. 14
2.9 Equivalent average circuit model of PWM switch for fixed duty ratio. 18
2.10 Detailed block diagram of current-mode control. 20
2.11 Flow chart of the Floquet method. 25
2.12 Flow chart of MATLAB implementation. 28
2.13 Transition between circuit topologies, where Top1 is on-state, Top2 is off-state, and Top3 is DCM state. 32

3.1 Genetic algorithms flow chart. 38
3.2 Representation of optimization parameters [113]. 39

4.1 Transition of topologies of a buck converter (2-period case). 43
4.2 Transition of topologies of a buck converter (multi-period case). . . 45
4.3 Current-mode controlled buck converter with sinusoidal disturbances. 47
4.4 Buck converter system Floquet multipliers (eigenvalues of monodromy matrix). 57
4.5 Periodic steady state response of the buck converter. 58

4.6 PSIM schematic circuit diagram of the buck converter system. . . . 58
4.7 Input voltage to output voltage frequency response of the buck converter system calculating using a commercial circuit simulation software. . . . 59
4.8 Comparison of input voltage to output voltage frequency responses of the buck converter system using different approaches. . . . 59
4.9 Input admittance of the buck converter system calculating using a commercial circuit simulation software. . . . 61
4.10 Comparison of exact input voltage to output voltage frequency responses using different approaches. . . . 62

5.1 Winding of toroid core. . . . 67
5.2 Detailed block diagram of current-mode control. . . . 70
5.3 Input filter. . . . 72
5.4 Buck converter under current-mode control with input filter and disturbance. . . . 74
5.5 Flow chart of optimization computation. . . . 79
5.6 Periodic steady state response for system designed using automated design process. . . . 81
5.7 Floquet multipliers for system designed using automated design process. . . . 81
5.8 Periodic steady state response of system designed using conventional design process. . . . 87
5.9 Floquet multipliers of system designed using conventional design process. . . . 87
5.10 Periodic steady state response of boost converter design. . . . 90
5.11 Periodic steady state response of buck-boost converter design. . . . 90

List of Tables

3.1 Terminology of genetic algorithms. 37

5.1 Design specifications. 76
5.2 Optimization results for system designed using automated design process. 80
5.3 Optimization results for power stage designed using conventional design process. 83
5.4 Optimization result for compensator designed using conventional design process. 84
5.5 Optimization results for input filter designed using conventional design process. 86
5.6 Optimization results for system designed using convention design process. 86
5.7 Optimization results for boost converter system designed using automated design process. 89
5.8 Optimization results for buck-boost converter system designed using automated design process. 89
5.9 Comparison of objective values for the conventional design process and the automated design process. 91
5.10 Comparison of design variables values for the conventional design process and the automated design process. 92

B.1 Parameter values for the buck converter in Chapter 4. 100
B.2 Parameter values for the buck converter for design optimization. . . 100
B.3 Parameter values for the boost converter for design optimization. . 100
B.4 Parameter values for the buck-boost converter for design optimization. 100

C 1 Inductor core data from Magnetics [118]. 103
C 2 Capacitor data from Vishay (voltage rating $V_r = 63$V) [119]. 104

Acknowledgments

I would like to appreciate Dr. Jeffrey S. Mayer for agreeing to advise me on area of power electronics. He has been a constant source of invaluable guidance, support, encouragement and motivation for my years at Penn State.

I want to take this opportunity to thank my parents Hui He and Hongwei Wang, who inspire and support me without hesitation. My appreciation also goes to my wife Xiaorui Yang and my daughter Olivia He, with whose support I strive through journey to search new knowledge. They make my life at Penn State very happy and meaningful.

Chapter 1

Introduction

In this introductory chapter, the motivation and objectives for the research are put forth. The accomplishments of the project and organization of the dissertation are then outlined.

1.1 Motivation

Switch-mode power converters have become as ubiquitous as the digital systems that they support in consumer electronics and myriad industrial, medical, and aerospace applications. They convert electrical power from the form available from a source to the form required by a load. For example, in a computer power supply, the 60-Hz, 120-V power available from a standard electrical outlet is converted to the dc, 3.3-V power required for the integrated circuits.

Switch-mode power converter design typically centers on the following five interrelated goals:

Power Quality A power converter must deliver power to its load within specifications for steady state voltage regulation and voltage ripple and for transient response time and overshoot. It must draw current from its source within specifications for distortion.

Efficiency A power converter must operate at high efficiency to minimize the cost of operation and thermal management.

Size A power converter should occupy minimum volume and have minimum weight.

Cost A power converter should have minimum cost.

Reliability A power converter should be reliable.

Historically, the paramount requirement of power quality has been achieved by sizing the energy storage elements - capacitors and inductors - to minimize the effects of the nonlinear/hybrid dynamics that stem from the switching process. More particularly, the energy storage elements have been selected to be large enough to provide a significant separation between the time scales associated with switching and with the circuit dynamics. This has also simplified system design as it has allowed the use of linear, continuous-time, small signal models obtained through various averaging techniques.

The increasing importance of size and cost dictates smaller energy storage elements. An attendant problem, however, is the reduction in time-scale separation to the point that conventional small signal models are not adequate. Thus, more advanced modeling, analysis, and design techniques are needed for power converter systems.

In most applications, a power converter system includes three subsystems: power stage, compensator, and input filter. The work flow for the conventional design process is illustrated in Figure 1.1. First, the power stage is designed; that is the energy storage elements are selected/designed to satisfy specified requirements on steady state power quality. Next, a compensator is designed to ensure steady state voltage regulation with acceptable transient response. Finally, a low pass input filter is added to mitigate the interaction between switching converter and power source.

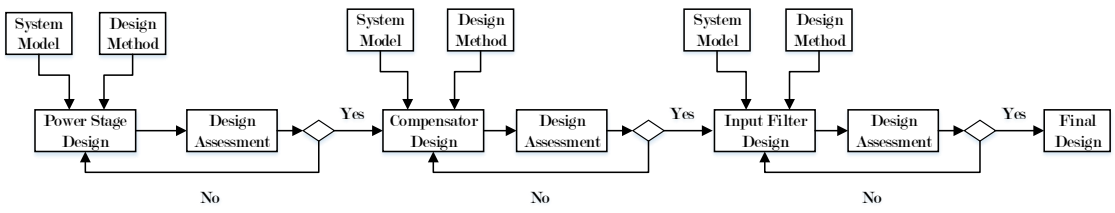

Figure 1.1. Conventional design process.

The conventional design process provides physical insight and does not require knowledge of advanced modeling and control techniques. One can use classic linear system theory to design the feedback control that regulates the converter output voltage. However, some important attributes of the converter, such as the nonlinear switching process are necessarily abstracted out of the model. Moreover, the serial design of the subsystems can lead to an overall system that is overly conservative or fails to meet specifications.

An automated design process using linear and nonlinear models and end-to-end system optimization would provide a desirable alternative to the conventional process. The work flow for such a design process is illustrated in Figure 1.2.

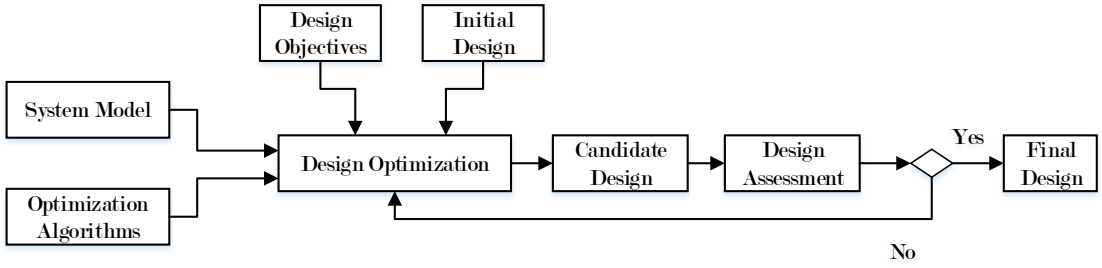

Figure 1.2. Automated design process.

In automated design process, an optimization algorithm is used to determine parameter values that minimize an overall cost function while ensuring that specifications on system performance are satisfied. The optimization algorithms could be chosen as, but not limited to, gradient methods, simulated annealing, and genetic algorithms. For each candidate design obtained via optimization, models of the entire system including power stage, compensator, and input filter are chosen and performance including steady state response and transient response is calculated and evaluated.

A large number of candidate designs would be assessed by objective function. The performance of each candidate design would be assigned a number. Within each design generation, the design with the best performance (smallest or largest number) would be selected. The termination condition for this design process is usually defined as the variation of performance between each design generation to be less than a pre-defined threshold.

The final design provides all parameter values of power converter system with

the best performance and satisfies design specifications. In power converter systems some design variables are discrete, for example core type for inductors. Such discrete variables can complicate conventional gradient-based optimization, but can be accommodated readily by more recently developed methods such as genetic algorithms.

The overarching objective of this research is an automated design process that determines optimal component parameter values for specified system performance requirements. Disturbance makes the performance of system deviate from the nominal operating point. To accurately describe the behavior of system, deriving enhancements to an analysis and design process based on the Floquet method to incorporate disturbances, which are modeled as sinusoidal signal, is another task of this research.

1.2 Research Contributions and Organization of Dissertation

This dissertation focuses on an automated design process that determines optimal parameter values for power converter systems to satisfy design specifications. The research involves enhancing the design methodology for dc-to-dc converter systems based on the Floquet method and optimization design using genetic algorithms.

In Chapter 1, the motivation and objectives for the dissertation have been explained.

In Chapter 2, essential features of power converter dynamics and modeling techniques are described with references to the relevant literature.

In Chapter 3, essential features of constrained optimization methods, both classical ones and recent ones, are described with references to the relevant literature.

In Chapter 4, extensions to the Floquet method are derived and then applied to study the performance of a buck converter system with current-mode control. We begin by investigating 2-period performance of such a system. Then the method is extended to a multi-period solver. The switched state space model and associated Floquet model are broadened to observe the influence of sinusoidal disturbance signals. Finally, the frequency response obtained by the enhanced Floquet method is

compared with those obtained using a small signal model and a commercial circuit simulation program. The results show that the frequency response characteristics obtained by the enhanced Floquet method are more accurate.

In Chapter 5, an automated design process incorporates the enhanced Floquet method of Chapter 4 is developed to determine parameter values for power converter systems. The process is demonstrated for a current-mode controlled buck converter with input filter. Methodologies of inductor and capacitor construction are provided. The core type of inductor is model as discrete variable. Due to the mixture continuous and discrete variables, genetic algorithms are used to solve the optimal solution of the design. The conventional design process is also reviewed and the results are compared with those obtained by the automated design process.

In Chapter 6, the advantages of the design method described in this dissertation is covered and potential improvements are discussed.

Chapter 2

Power Converter System Dynamics and Modeling

The switch-mode operation of power semiconductor devices at the heart of a power converter gives rise to fairly complicated dynamics that require special attention if optimal design is to be achieved. The essential characteristics of power converter system dynamics will be illustrated using the buck converter as an example, because it is the most widely used dc-to-dc converter topology with applications in dc power supplies, dc power system interface modules, and dc motor drives.

2.1 Power Converter System Dynamics

2.1.1 Principle of Operation

The circuit shown in Figure 2.1 is a buck converter connecting a source network represented by a Thevenin equivalent circuit (V_{oc}, Z_{th}) to a load network represented by a resistor (R_{load}).

The output voltage v_o is to be regulated to a desired value V_o^{ref} even if there are variations in the input voltage v_d, load resistance R_{load}, and internal parameter values. The output voltage v_o is made to track the reference voltage V_o^{ref} by controlling the duty ratio of the MOSFET through a binary-valued gating signal $q(t)$. Duty ratio D is defined as the ratio of the on-duration t_{on} to the switching period T_s. When the MOSFET is on, the diode is off. The pulse-width modulation

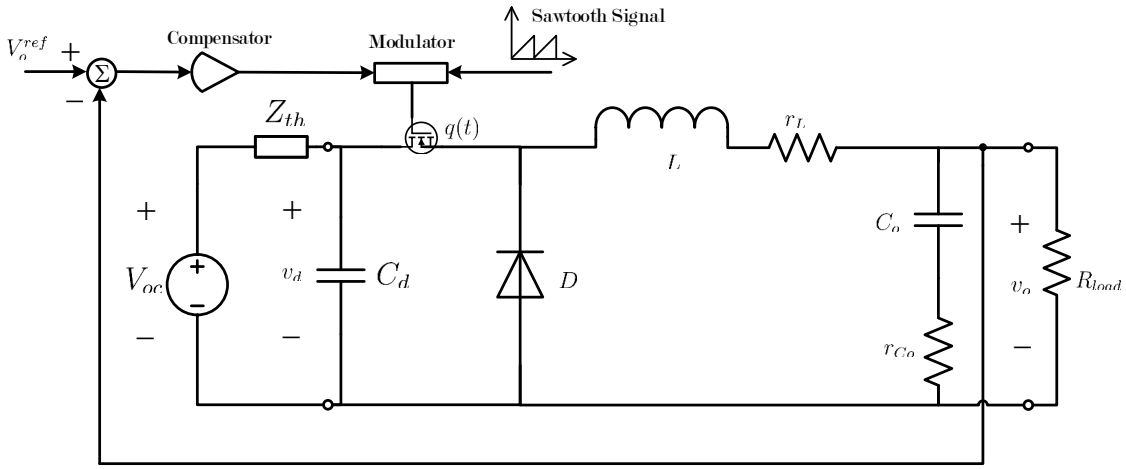

Figure 2.1. Buck converter system.

adjusts the on-duration of the switch, hence duty ratio, to control the output voltage in an average sense.

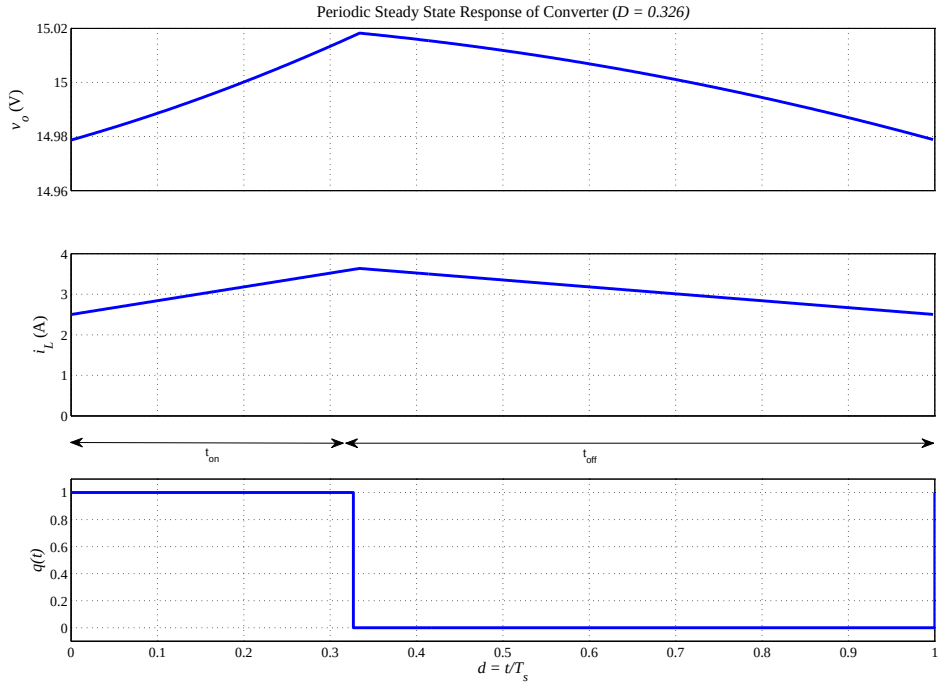

Figure 2.2. Typical periodic steady state waveforms of buck converter operating in continuous conduction mode.

Figure 2.2 illustrates typical periodic steady state waveforms for key variables

of the buck converter system shown in Figure 2.1. In pulse-width modulation with constant switching frequency, the gate signal $q(t)$ is usually generated by comparing a control signal to a sawtooth carrier signal. The control signal is obtained from a compensator amplifier acting on the difference between the actual output voltage and the reference output voltage. When the compensator signal is greater than the carrier signal, the gate signal is 1, indicating that the switch should be on. With the switch on, the voltage across the inductor is positive and the current through the inductor rises. When the compensator signal is less than the carrier signal, the gate signal is 0, indicating that the switch should be off. With the switch off, the inductor acts as an energy source continuing supplying power to the load and the current through the inductor falls. The diode acts as a free-wheel path for the current and stays on when the switch is off.

There are two operating modes for the buck converter: continuous conduction mode (CCM) and discontinuous conduction mode (DCM). CCM operation is illustrated in Figure 2.2; DCM operation is illustrated in Figure 2.3. When the buck converter operates in DCM, the current through inductor decreases in the interval t_{off1} and remains at zero in the interval t_{off2} due to blocking by the diode. In practical applications, the buck converter may operate in both modes, although CCM operation is more desirable.

2.1.2 Complexity of Dynamics

Several aspects of power converter dynamics complicate modeling, analysis, and control design for these systems. More specifically, nonlinear and hybrid dynamics require special attention.

Nonlinear Dynamics Power converters are inherently nonlinear dynamical systems due to switching. In many cases, it can be assumed that switching is an ideal process, which implies that there is zero voltage across an on-state switch, zero current through an off-state switch, and transitions between on and off states are instantaneous. Under this assumption, the power converter system can be modeled as a multi-topology system. The nonlinear dynamics are manifest in the presence of switching frequency harmonics.

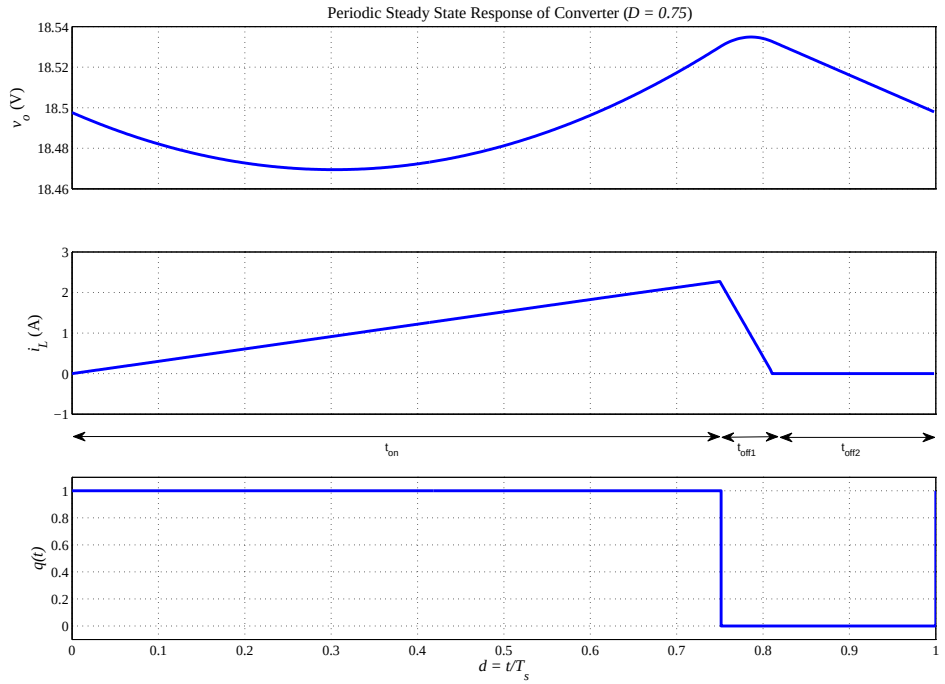

Figure 2.3. Typical periodic steady state waveforms of buck converter operating in discontinuous conduction mode.

Hybrid Dynamics The challenges of hybrid dynamics for such systems are twofold. The instants at which switch transitions occur are determined by either discrete event or continuous time signals. A directly controllable switch (MOSFET) is the discrete event command for gating signal, for instance, on-state or off-state. Discrete event could be triggered by one of the following continuous time signals: the state or the input of power converter system becomes equal to reference value, a specific time instant is reached which usually is switching period T_s, and the current through inductor i_L decreases to 0 leading to DCM operation.

Figure 2.4 shows the transient response of a buck converter to a step change in V_o^{ref} from 1 V to 1.3 V at the fifth switching period with current-mode control. The power converter system starts adjusting itself to increase output voltage v_o to the reference value. The instants at which switches transitions are triggered by either current limit, output voltage v_o reaching V_o^{ref}, or specific time instant T_s and the buck converter needs to transit between different topologies. These complexities make the buck converter settle down in more than 15 switching periods.

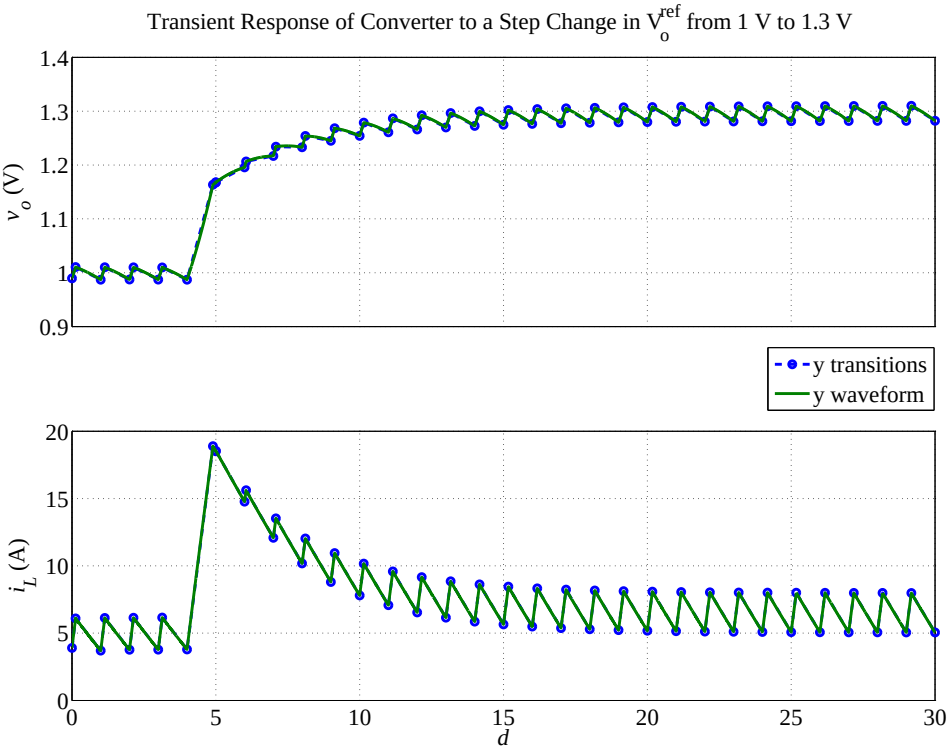

Figure 2.4. Transient response of buck converter to a step change in V_o^{ref} from 1 V to 1.3 V.

Typically, both low-frequency and high-frequency behavior of the system must be considered. This usually requires two different models. A low-frequency averaged model is used for feedback control design, while a separate high-frequency model is used for predicting sub-harmonic oscillations or ripple instability.

Historically, complications arising from the nonlinear and hybrid dynamics have been somewhat mitigated by the multiple-time scale nature of the system. Switching occurs on a fast time scale (order of 1 μs) while the most important part of the circuit response, variation of the output voltage, occurs on a slow time scale (order of 10 μs to 100 μs). This separation between time scales has allowed utilizing separate models for different purpose. Pressure to decrease the size of converter components, however, is pushing the slow time scale towards the fast time scale. Consequently, an advanced methodology incorporating different time scales must be developed.

2.1.3 Feedback Control

Many control strategies have been proposed and used to regulate power converter systems. The most common strategy historically is now referred as voltage-mode control (VMC) which is illustrated as Figure 2.5. In VMC, a compensator acts on the error between the reference value of the converter output voltage and the actual value of that voltage. The compensator output signal is compared to a sawtooth signal to generate a gate signal.

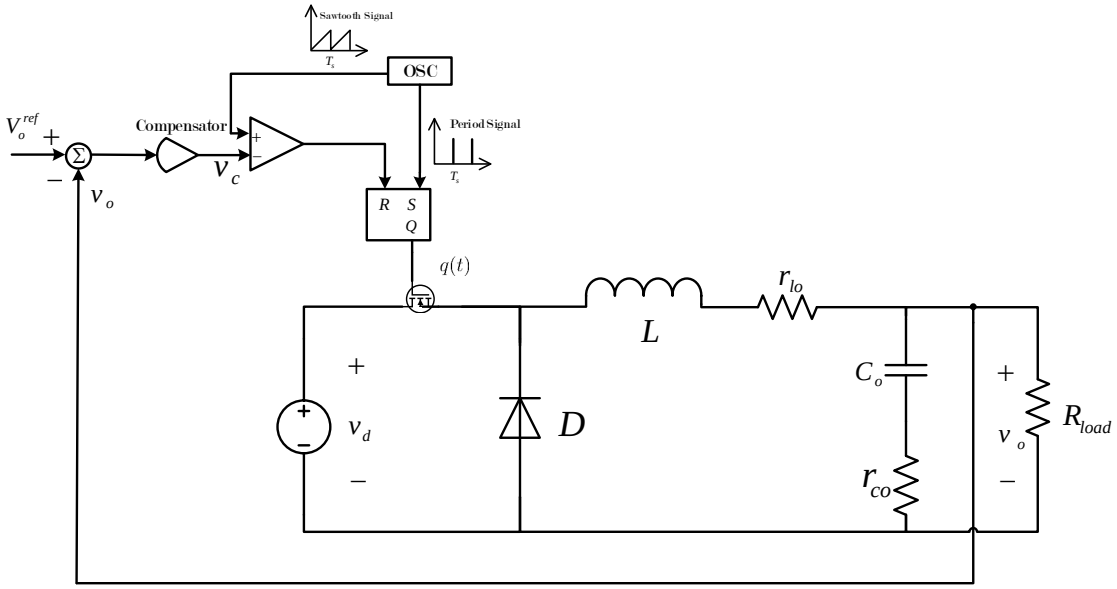

Figure 2.5. Voltage-mode control for buck converter.

Current-mode control (CMC), which is illustrated in Figure 2.6, is the most common strategy today. It aims to regulate the output voltage by controlling the output inductor current. A current sensor r_s is used to measure the output inductor current. Once this current exceeds the compensator signal v_c, the flip flop resets the gate drive signal. If the buck converter is operated with a duty cycle $D > 0.5$, a problem of sub-harmonic oscillations arises and causes the converter system to become unstable. This instability can be avoided by adding an external stabilizing ramp or slope compensation to the output inductor current, shown as v_{sc} in Figure 2.6, with whose help the switch turns off before the current waveform intersecting with compensator signal v_c and thus eliminates sub-harmonic oscillations. Under this control strategy, the inductor can be viewed as an independent

current source which results in the order reduction of the plant model and simplification of controller design. Current-mode control can also provide good audio susceptibility of buck converters compared to voltage-mode control. The current loop provides extra attenuation of input noise. It is even possible to eliminate audio susceptibility of buck converters operating in current-mode control if a proper sawtooth ramp is chosen [1]. These advantages make current-mode control well accepted in practical application of converter systems.

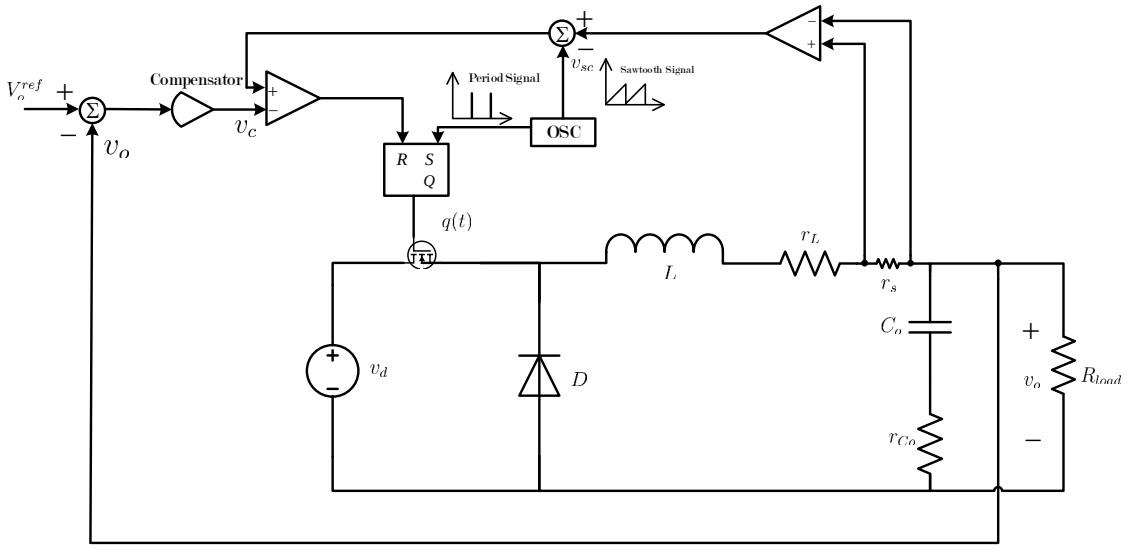

Figure 2.6. Current-mode control for buck converter.

Holland [2] systematically analyzed and modeled current-mode control of converter systems. Middlebrook [3] explained why the output of current control approximates a current source and complicates the behaviors of power converters using y-parameter model. In [4, 5], the authors investigated time-varing effects and explored high-frequency behaviors in both CCM and DCM operations. A feedforward loop was proposed to improve the stability and transient performance in [6] and [7]. In addition to transfer function of converter systems with current-mode control, the transfer function of converter systems with a feedforward term was presented [8, 9]. Researchers [10–12] focused on designing the current-mode controller of power converters using advanced control algorithms such as adaptive control, LQR control, and nonlinear control. With increasing popularity of computer-aided design, current-mode control of power converter was implemented digitally in [13–15].

2.1.4 Input Filter

To meet power quality requirements at the input to a power converter system, an input filter is often employed between the source network and the converter input, as shown in Figure 2.7. With such a filter, the voltage and current ripple caused by switching have less impact on the source network. Also, performance degradation of the converter due to some source transients can be avoided.

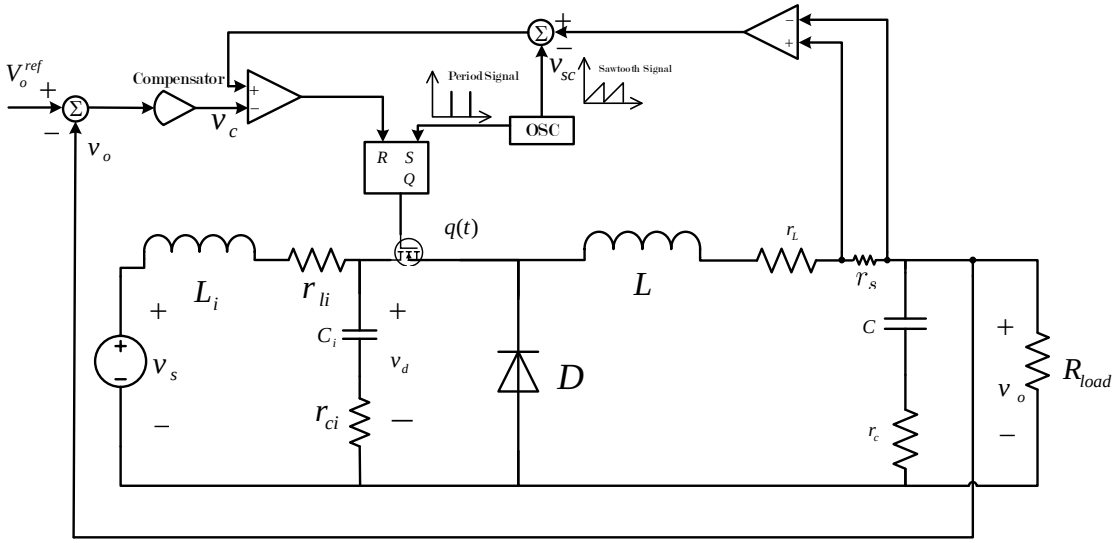

Figure 2.7. Current-mode control for buck converter with an input filter.

Classical Explanation of Origin of Input Filter Instability

Consider a switching converter system shown in Figure 2.7 and define voltage conversion ratio as $\mu = \frac{V_d}{V_o}$. For a given resistance load R_{load}, the control strategy manipulates the conversion ratio μ to maintain constant output voltage. Assuming the switching converter is ideal, it follows that the average input current decreases as input voltage rises, and vice versa. Therefore an ideal switching regulator behaves like a negative dynamic resistance. More specifically, the equivalent input resistance of the converter can be expressed as

$$R_i = \frac{dV_d}{dI_d} = \frac{d}{dI_d}\frac{P}{I_d} = -\frac{P}{I_d^2} = -\frac{V_d}{I_d} = -\mu^2\frac{V_o}{I_o} = -\mu^2 R_{load}.$$

This is the low-frequency value of the input impedance. For the basic buck converter shown in Figure 2.7, the conversion ratio $\mu = \frac{1}{D}$, so that $R_i = -\frac{R_{load}}{D^2}$ where D is the duty ratio of the converter. In small signal analysis around an operating point, R_i can be considered as a constant and LC input filter with dc-to-dc converter as load can be treated as a linear as shown in 2.8. The transfer function

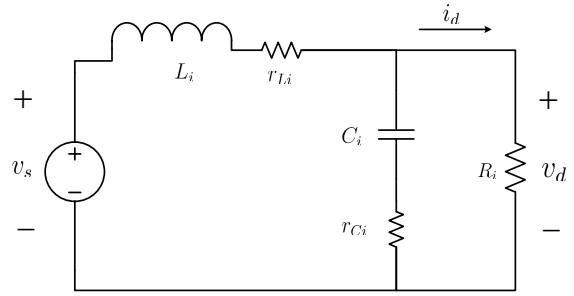

Figure 2.8. LC input filter loaded by equivalent input resistance of dc-to-dc converter.

from v_s to v_d is:

$$\begin{aligned}\frac{v_d(s)}{v_s(s)} &= \frac{(\frac{1}{sC_i} + r_{ci}) \parallel R_i}{(\frac{1}{sC_i} + r_{ci}) \parallel R_i + sL_i + r_{li}} \\ &= \frac{\frac{r_{ci}C_iR_i}{L_i(C_iR_i+C_ir_{ci})}s + \frac{R_i}{L_i(C_iR_i+C_ir_{ci})}}{s^2 + \frac{L_i+r_{ci}C_iR_i+r_{li}C_iR_i+r_{li}C_ir_{ci}}{L_i(C_iR_i+C_ir_{ci})}s + \frac{R_i+r_{li}}{L_i(C_iR_i+C_ir_{ci})}}\end{aligned}$$

The characteristic polynomial is:

$$P(s) = s^2 + \frac{L_i - \mu^2 r_{ci}C_iR_{load} - \mu^2 r_{li}C_iR_{load} + r_{li}C_ir_{ci}}{L_i(C_ir_{ci} - \mu^2 C_iR_{load})}s + \frac{r_{li} - \mu^2 R_{load}}{L_i(C_ir_{ci} - \mu^2 C_iR_{load})}.$$

The coefficients in $P(s)$ could result in positive real part roots which transform to positive exponential modes in the time domain and destabilize the power converter system. Thus the input filter interacts with negative resistance characteristics of the converter and behaves as a negative resistance oscillator. This is the origin of instability caused by external input filter.

Input Filter Design Criteria

Interaction between the input filter and the converter control loop can cause a reduction in loop gain that may result in the transient response degrading from

well-damped to oscillatory.

Much research effort has been devoted to characterizing the instability and creating design methods for the filter. Middlebrook [16] was one of the first to investigate the input filter design problem for pulse-width modulation converter systems. The origin of the instability introduced by input filter was described in terms of negative incremental input resistance. An exact eigenvalue analysis [17] predicted the instability for large values of inductance used in converter systems. The input and output dynamics of the converter with input filter was examined using linear system analysis in [18–20]. Nonlinear stability analysis on both fast and slow scales was studied in [21] but was limited to simple systems.

Input filter design criteria were formulated using a y-parameter small signal model to ensure stability and performance [22–24]. The filter output impedance transfer functions were designed to be small enough such that the effects of current loop became negligible [25, 26]. Parallel damping resistances were added to the input filter to minimize its negative effects and design conditions for stability were proposed using control-to-output transfer function of averaged model [27]. A virtual resistor method was proposed to damp the transient oscillations of the input filter [28]. Kelkar and Lee [29, 30] proposed an input filter compensation scheme using a feedforward loop to cancel the effect of output impedance peak of the input filter. An input voltage feedback compensation [31] was presented to actively stabilize the input filter via current-mode control. Using state feedback and pole placement technique was shown to be feasible and guaranteed adequate level of performance by a varying gain in [32]. All these design criteria were formulated using small signal models.

2.2 Power Converter System Modeling

Accurate models of the converter system are indispensable for system design. There are three major approaches to the modeling and analysis of power converter systems: switched state space model, linear continuous-time or small signal model, and nonlinear discrete-time or large signal model. Each of these is described briefly in this section.

2.2.1 Switched State Space Model

Most power converter systems can be modeled using a switched state space model (SSSM) that includes a piecewise linear time invariant (piecewise-LTI) state space model for each topology along with a set of switching surfaces and transition maps to determine when and in what manner transitions from one topology to another occur. The LTI model for each topology is simply:

$$\dot{\mathbf{x}}_m = \mathbf{A}_m\mathbf{x}_m + \mathbf{B}_m\mathbf{u} \tag{2.1}$$

$$\mathbf{y} = \mathbf{C}_m\mathbf{x}_m + \mathbf{D}_m\mathbf{u} \tag{2.2}$$

where m is the topology index, and $\mathbf{x}_m$ is the state variable vector for circuit topology m . The input variable vector $\mathbf{u}$ and output variable vector $\mathbf{y}$ are assumed to be independent of topology. Switching instants between different topologies of the system can be determined by switching surfaces defined by equation (2.3), where $\boldsymbol{\sigma}_m$ denotes a set of switching surfaces that determine the instant $d_m T_s$ at which system transitions from topology m to topology n; T_s is the switching period and $d_m \in [0, 1)$. Equation (2.4) relates the state vector for topology n to the state vector for the topology m using map $\mathbf{R}_{nm}$.

$$\mathbf{0} = \boldsymbol{\sigma}_m(\mathbf{x}_m, \mathbf{u}, d_m) \tag{2.3}$$

$$\mathbf{x}_n = \mathbf{R}_{nm}\mathbf{x}_m \tag{2.4}$$

The switched state space model, equations (2.1)-(2.4), is suitable for simulating the transient response of a power converter starting from a specified initial topology $m = m_0$ and state vector $\mathbf{x}_m = \mathbf{x}_0$ and given the input signal $\mathbf{u}(t)$ for $t > 0$. Such simulation is useful for examining converter response in particular cases, such as start-up or changes in reference values. It is less suitable for studying stability due to the stiff nature of the system dynamics. The model also serves as an input to algorithms for so-called state space averaging and the Floquet method.

2.2.2 Linear Continuous-Time Model (Small Signal Model)

The most common control design practices for power converter systems utilize linear continuous-time models that are derived using various averaging techniques. They are considered to be a good compromise between accuracy and simplicity. Middlebrook and Cúk [33] proposed the so-called state-space averaging method for deriving equivalent small signal models of dc-dc converters and a comprehensive analysis was explained in detail in [34]. Low frequency characteristics and DCM operation were investigated using averaged modeling technique for switched dc-dc converters in [35] and [36] respectively. Researchers [37–39] also managed to use generalized state space averaging approach to analyze power converter systems. A circuit-oriented method of small signal modeling based on averaging of the PWM switch was put forth in [40, 41]. Tan and Middlebrook [42] developed a unified model for current-mode modulator that included the sampling effect. Properties of current-mode controlled power converters were examined [43] for averaged and sampled-data models. A new, continuous-time model for current-mode control [1] was derived based on sampled-data modeling technique. To incorporate the sample and hold effect, a state space model that was two order higher than that of power stage was provided [44]. These modeling techniques can be categorized into the following groups.

State Space Averaging In [33], a small signal model for the buck converter system was presented based on the state space averaging approach. A state space form of small signal model for a converter operating in CCM is described as equation (2.5).

$$\begin{aligned} \dot{\mathbf{x}} &= \mathbf{A}\mathbf{x} + \mathbf{B}v_d + [(\mathbf{A}_1 - \mathbf{A}_2)\mathbf{X} + (\mathbf{B}_1 - \mathbf{B}_2)V_d]d \\ \mathbf{y} &= \mathbf{C}\mathbf{x} + (\mathbf{C}_1 - \mathbf{C}_2)\mathbf{X}d \end{aligned} \tag{2.5}$$

where D is the operating point duty cycle, d is the small signal perturbation of duty cycle generated by the control compensator, and v_d is the small signal perturbation of input voltage V_d. The matrices $(\mathbf{A}_1, \mathbf{B}_1, \mathbf{C}_1)$ and $(\mathbf{A}_2, \mathbf{B}_2, \mathbf{C}_2)$ represent the state space model for the switch-on and switch-off topologies respectively. The matrices

$(\mathbf{A}, \mathbf{B}, \mathbf{C})$ are obtained by time weighted averaging of the respective topology state matrices:

$$\begin{aligned} \mathbf{A} &= D\mathbf{A}_1 + (1-D)\mathbf{A}_2 \\ \mathbf{B} &= D\mathbf{B}_1 + (1-D)\mathbf{B}_2 \\ \mathbf{C} &= D\mathbf{C}_1 + (1-D)\mathbf{C}_2 \\ \mathbf{X} &= -\mathbf{A}^{-1}\mathbf{B}V_d. \end{aligned}$$

The control-to-output transfer function of the small signal model can be derived from equation (2.5) as

$$\frac{v_o(s)}{d(s)} = \mathbf{C}[s\mathbf{I} - \mathbf{A}]^{-1}[(\mathbf{A}_1 - \mathbf{A}_2)\mathbf{X} + (\mathbf{B}_1 - \mathbf{B}_2)V_d] + (\mathbf{C}_1 - \mathbf{C}_2)\mathbf{X}. \tag{2.6}$$

Circuit Averaging In [40] and [41], a circuit averaging approach was proposed using an average equivalent circuit model of a PWM switch. This averaging technique can be used to analyze small signal characteristics of a large class of PWM power converters in both CCM and DCM. A small signal model of PWM switch is shown in Figure 2.9. The transformer is used to describe the voltage and current relationships between ports ap and cp, where D represents the duty cycle of the PWM switch.

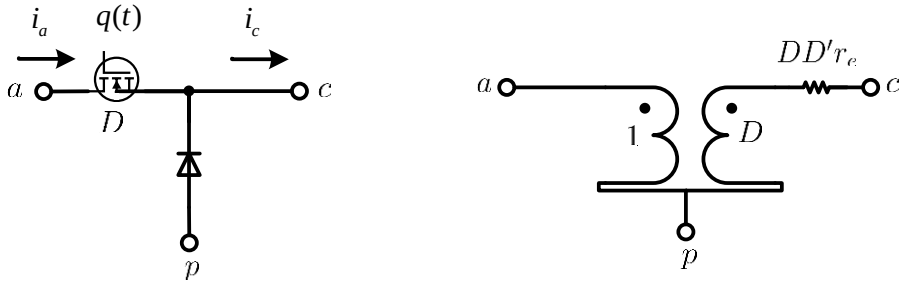

Figure 2.9. Equivalent average circuit model of PWM switch for fixed duty ratio.

Then the small signal model is described as follows:

$$\begin{aligned} i_a &= Di_c + I_c d \\ v_{ap} &= \frac{v_{cp}}{D} + i_c r_e D' - [V_{ap} + I_c(D - D')r_e]\frac{d}{D} \end{aligned}$$

where $D' = 1 - D$. r_e is in general a function of the capacitor equivalent series resistant (ESR) and the load resistor R_{load}. From this point, one can substitute this small signal model for the PWM switch into the overall converter model and analyze any single-switch PWM power converter.

Average models, obtained either by state space averaging or circuit averaging, provide accurate low frequency response but fail to predict sub-harmonic oscillations. Ridley's model [1] is based on a discrete sampled data model and predicts characteristics including sub-harmonic oscillation. But the analysis is limited to frequency from dc to half the switching frequency. The main limitation with of small signal models in analyzing current-mode controlled converter systems results from the modeling of its nonlinear part and the switching operation. Due to the nonlinear property inherited in discontinuous conduction mode and switching behavior, small signal models become even less impressive when converter systems operate in this region. To observe sub-harmonic oscillation, researchers usually perform simulation in time domain which can be very time consuming and subject to numerical problems.

Small Signal Modeling of Modulators A new small signal model for current-mode control was developed in [1]. The model takes into account the sampling effect due to switching. This method is based on sampled data modeling and has good accuracy up to half the switching frequency. Figure 2.10 shows a detailed block diagram of current-mode control presented in [1]. $T_c(s)$ represents compensator transfer function of voltage loop. The author managed to derive transfer function of current loop $T_i(s)$ that captures sampled data nature of the inductor current loop by $T_{sd}(s)$. Then the closed-loop transfer function from v_o^{ref} to v_o can be derived, starting from where classic linear analysis can be applied. This small signal analysis model is referred as Ridley's model in this dissertation.

All of these small signal models are obtained by using small perturbation and linearization of the nonlinear model around an operating point. When a large signal perturbation occurs, these models fail to provide insights into system performance. Switching operation of converter systems make it a nonlinear system. As switching frequency increasing, such nonlinear effects, which are responsible for sub-harmonics of converter systems and could cause bifurcations, cannot be ne-

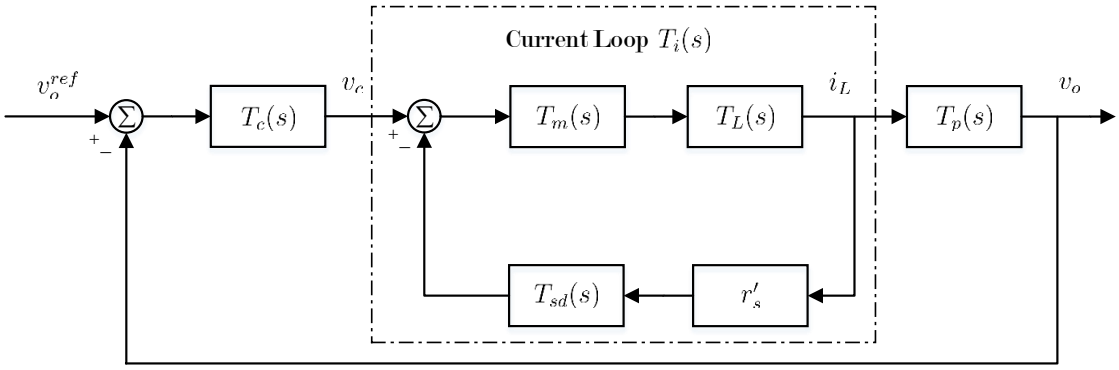

Figure 2.10. Detailed block diagram of current-mode control.

glected. Therefore, it is important to analyze converter systems using a nonlinear model.

2.2.3 Nonlinear Discrete-Time Model (Large Signal Model)

Equation (2.1)-(2.4) is also referred as large signal model or switching model in the literature. It is a nonlinear model due to switching. It can be transformed to a nonlinear discrete-time switched state space model [45] of the form:

$$\mathbf{x}[k+1] = \mathbf{f}(\mathbf{x}[k], \mathbf{p}[k], \mathbf{d}[k]; k) \tag{2.7}$$

$$\mathbf{0} = \boldsymbol{\sigma}(\mathbf{x}[k], \mathbf{p}[k], \mathbf{d}[k]; k) \tag{2.8}$$

where $\mathbf{x}[k]$ is a vector of state variables at the start of the k^{th} switching period, $\mathbf{p}[k]$ is a vector of parameters used to characterize the input during the k^{th} switching period, and $\mathbf{d}[k]$ is a vector of the transition instants within the k^{th} switching period. This model combines a state space model with constraint functions as described by equation (2.8) which is also called a switching surface. Given $\mathbf{x}[k]$ and $\mathbf{p}[k]$, one can solve equation (2.8) for $\mathbf{d}[k]$ and substitute the result into equation (2.7) to determine $\mathbf{x}[k+1]$. This usually requires an initial guess of the solution and iterative numerical calculations.

2.2.4 Periodic Steady State Model

Switched power converter systems usually exhibit periodic behavior with the period being equal to the switching period T_s. Poincaré map is a useful tool for studying the stability of a periodic system. By computing the Jacobian of the Poincaré map periodic performance of a diode bridge rectifier circuit was studied in [46]. Nonlinear dynamics and exact formula for the Jacobian of the Poincaré map were derived in [47,48] but were limited to simple switching circuit. The Floquet method and the harmonic balance method were suggested to analyze the stability and response of periodic systems [49]. Frequency response of piecewise-LTI periodic systems were investigated in [50, 51]. More recently, research has focused on using Floquet method [52] to analyze and design power converter systems. Stability of power converter systems was studied in [53, 54]. Both the fast-scale and slow-scale instabilities of particular converter systems were investigated using the Floquet method in [55–58].

The Floquet method makes it possible to reduce the study of the original periodic system to that of a time-invariant one. It converts the stability analysis of periodic system as equation (2.7) and (2.8) to that of a discrete-time linear time-invariant one described as equation (2.9).

$$\mathbf{x}[k+1] = \mathbf{H}_x\mathbf{x}[k] + \mathbf{H}_u\mathbf{u}[k] \tag{2.9}$$

where $\mathbf{H}_x$ is referred to as the monodromy matrix. The eigenvalues of $\mathbf{H}_x$ are named Floquet multipliers. Kriventsov [59] derived closed-form expressions for the monodromy matrix of a system with piecewise constant inputs; the system may include multiple topologies, discontinuous conduction mode, and PWM control.

Bifurcation and chaos were studied by simulation or analytical analysis for converter systems in [55, 56, 60, 61]. A proposition in [62] states that the system 2.9 is stable if and only if the Floquet multipliers of $\mathbf{H}_x$ have modulus less than 1. Floquet multipliers also provide bifurcation information. In [56] the relationship between bifurcation type and modulus of Floquet multipliers was described.

- If one of the Floquet multipliers exits the unit circle through +1, then either a cyclic-fold, or a symmetry breaking, or a transcritical bifurcation occurs.

- If a Floquet multiplier exists the unit circle through -1, a period doubling or flip bifurcation occurs.
- If two of the Floquet multipliers exit the unit circle as complex conjugates, a secondary Hopf bifurcation occurs.

Background on Floquet Method

Poincaré Map Consider the periodic system defined by the following piecewise-LTI model as follows.

$$\begin{aligned} \dot{\mathbf{x}}_m(t) = \mathbf{A}_m\mathbf{x}_m(t) + \mathbf{B}_m\mathbf{u}(t) \qquad & (k + d^k_{m-1})T_s \le t \le (k + d^k_m)T_s \\ & 0 \le d^k_m \le 1 \qquad m = 1, 2, \ldots, M \end{aligned} \tag{2.10}$$

Here $\mathbf{x}_m(t) \in \mathbb{R}^{N_m}$ and $\mathbf{u}(t) \in \mathbb{R}^{N_p}$ are column vectors of state variables and piecewise constant inputs; and $\mathbf{A}_m \in N_m \times N_m$ and $\mathbf{B}_m \in N_m \times N_p$ are state matrices and control matrices in m^{th} topology respectively, where N_m is the number of states and N_p is the number of inputs. The integer variable k is the switching period number; T_s is the switching period; and M is the number of circuit topologies during each switching period. The system is assumed to go through the same sequence of topologies during each switching period. The value of d^k_m is the switching time instant at which the system jumps from m to $m + 1$ topology in the k^{th} switching period and is usually determined by control strategies. We define $d^k_0 = 0$ and $d^k_M = 1$; that is each period starts at $t = kT_s$ and ends at $t = (k+1)T_s$.

For introductory purposes, assume that all switching time instants d^k_m are known when the trajectory of the time-domain response is calculated. In each topology, the system is defined as a linear time-invariant system and the trajectory of response can be determined using linear system theory. Let us focus on the first topology of k^{th} period, that is $kT_s \le t \le (k + d_1)T_s$. The response of the system $\mathbf{x}_1(t)$ is governed by $\mathbf{A}_1$ and $\mathbf{B}_1$, given initial condition $\mathbf{x}^0_1$ and $t_0 = kT_s$. The input signal $\mathbf{u}$ is presumed to be piecewise constant.

$$\mathbf{x}_1(t) = \mathbf{\Phi}_1(t, t_0)\mathbf{x}^0_1 + \mathbf{\Psi}_1(t, t_0) \tag{2.11}$$

where

$$\begin{aligned}\mathbf{\Phi}_1 &= e^{\mathbf{A}_1(t-t_0)} \\ \mathbf{\Psi}_1 &= \int_{t_0}^{t} \mathbf{\Phi}_1(t,\tau)\mathbf{B}_1\mathbf{u}(t-\tau)d\tau \\ &= \int_{t_0}^{t} \mathbf{\Phi}_1(t,\tau)\mathbf{B}_1 d\tau\mathbf{u}\end{aligned}$$

So at the last time instant within first topology, that is $t = (k+d_1)T_s$,

$$\mathbf{x}_1[(k+d_1)T_s] = \mathbf{\Phi}_1[(k+d_1)T_s, kT_s]\mathbf{x}_1^0 + \mathbf{\Psi}_1[(k+d_1)T_s, kT_s]$$

Then, taking $\mathbf{x}_2^0 = \mathbf{x}_1[(k+d_1)T_s]$ as the new initial condition for the second topology and using equation (2.11) with 1 replaced by 2, the response at the final time instant of second topology can be calculated as

$$\begin{aligned}\mathbf{x}_2[(k+d_2)T_s] &= \mathbf{\Phi}_2[(k+d_2)T_s, (k+d_1)T_s]\mathbf{x}_2^0 + \mathbf{\Psi}_2[(k+d_2)T_s, (k+d_1)T_s] \\ &= \mathbf{\Phi}_2(\Delta_2)\mathbf{\Phi}_1(\Delta_1)\mathbf{x}_1^0 + \mathbf{\Phi}_2(\Delta_2)\mathbf{\Psi}_1(\Delta_1) + \mathbf{\Psi}_2(\Delta_2)\end{aligned}$$

where $\Delta_i = d_i - d_{i-1} \quad i \in \{1, 2, \ldots, M\}$.

Then, taking $\mathbf{x}_3^0 = \mathbf{x}_2[(k+d_2)T_s]$ as the new initial condition for the third topology and using an equation similar to equation (2.11) for all the remaining topologies, the response at the end of k^{th} period is determined by the following equation.

$$\mathbf{x}_M[(k+1)T_s] = \mathbf{\Pi}_1^M\mathbf{x}_1^0[kT_s] + \mathbf{\Theta}_M\mathbf{u} \tag{2.12}$$

where

$$\mathbf{\Pi}_p^q = \prod_{i=p}^{q} \mathbf{\Phi}_i(\Delta_i) \tag{2.13}$$

$$\mathbf{\Theta}_q = \sum_{i=1}^{q} \mathbf{\Pi}_{i+1}^q \mathbf{\Psi}_i(\Delta_i) \tag{2.14}$$

In equation (2.13), if the upper index is smaller than the lower index, that is $p > q$, the value of the product is assumed to be an identity matrix. The values of state variables at the end of the k^{th} period also equal to those at the beginning of the first topology of $k+1$ period. So the mapping function of state variables over one

switching period is established .

$$\begin{aligned} \mathbf{x}_1[k+1] &= \mathbf{f}(\mathbf{x}_1[k], \mathbf{u}[k], \mathbf{d}) \\ &= \mathbf{\Pi}_1^M \mathbf{x}_1[k] + \mathbf{\Theta}_M \mathbf{u}[k] \end{aligned} \tag{2.15}$$

where $\mathbf{x}_1[k] = \mathbf{x}_1(kT_s)$ is the value of state vector at the beginning of the k^{th} period, by time-periodic sampling. Equation (2.15) is also referred as Poincaré map of the system, assuming switching instants d_m^k are known. The periodic solution for this discrete LTI map is obtained as

$$\mathbf{X}_1 = (\mathbf{I} - \mathbf{\Pi}_1^M)^{-1} \mathbf{\Theta}_M \mathbf{U} \quad \text{if } | \mathbf{I} - \mathbf{\Pi}_1^M | \neq 0.$$

Thus, by Poincare map, the analysis of a periodic system with period T_s described by equation (2.10) is converted to the analysis of discrete-time LTI system described as equation (2.15).

Floquet Method on Periodic Systems with Constant Inputs In this section, the switching instants d_k^m are assumed to be known. But in practical systems, especially in feedback controlled systems, switching is controlled dynamically and depends on state variables, input variables, and clock signals. Usually, the switching instants can be determined by solving for the instant at which the system response reaches a switching surface:

$$\boldsymbol{\sigma}(\mathbf{x}[k], \mathbf{p}[k], \mathbf{d}[k]; k) = \mathbf{0}. \tag{2.16}$$

Given $\mathbf{x}[k]$ and $\mathbf{p}[k]$, one can solve equation (2.16) for $\mathbf{d}[k]$ and substitute the result into equation (2.15) to determine $\mathbf{x}[k+1]$. In the periodic steady state solution, the values of state variables remain the same for each period; that is $\mathbf{x}_1[k+1] = \mathbf{x}_1[k]$. Usually, this periodic solution must be found numerically. The most popular approach is to apply a Newton-Raphson-like algorithm to equation (2.15).

$$\mathbf{x}_1[k+1] = \mathbf{x}_1[k] - \left(\mathbf{I} - D_x \mathbf{f}(\mathbf{x}_1[k], \mathbf{d}, \mathbf{u})\right)^{-1} \left(\mathbf{x}_1[k] - \mathbf{f}(\mathbf{x}_1[k], \mathbf{d}, \mathbf{u})\right) \tag{2.17}$$

where $D_x\mathbf{f}(\mathbf{x}_1[k], \mathbf{d}, \mathbf{u})$ is constant and known as the monodromy matrix. Its eigenvalues are referred as Floquet multipliers. By investigating the locations of the Floquet multipliers, one can assess the stability of a periodic system; that is, if and only if the Floquet multipliers are located within the open unit circle, the system is stable and has a periodic steady state solution. A flow chart showing the steps of the Floquet method appears in Figure 2.11

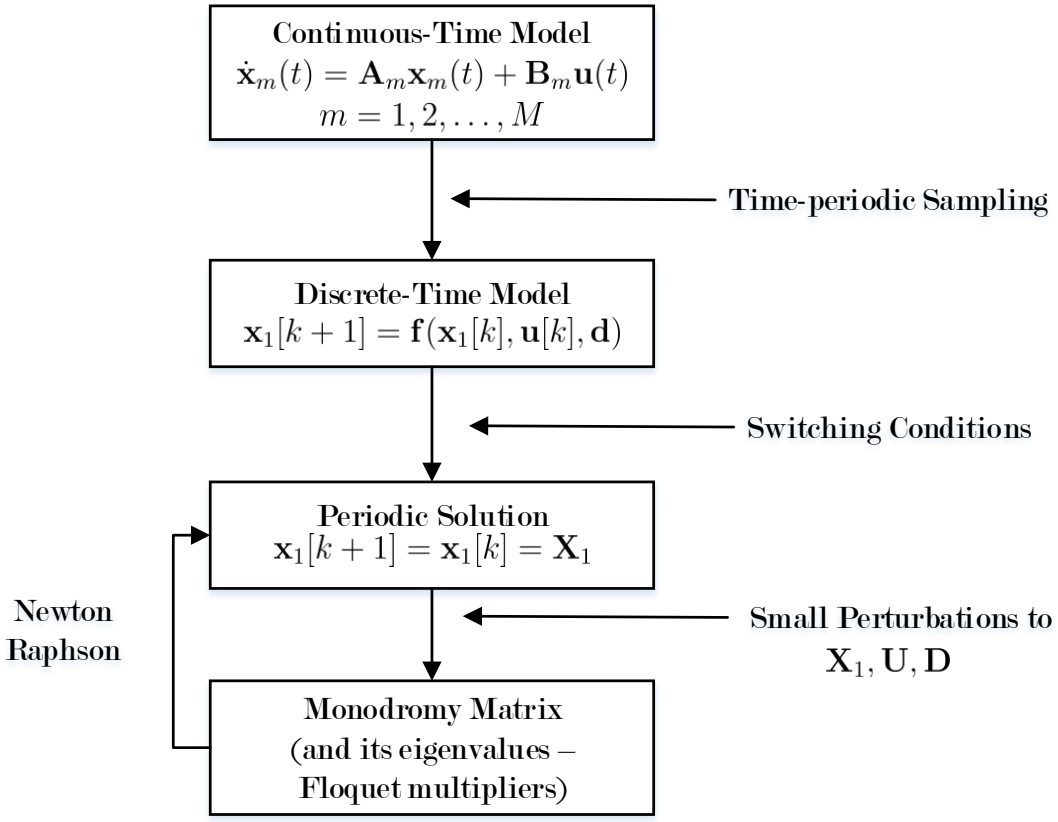

Figure 2.11. Flow chart of the Floquet method.

In [59, 60], Kriventsov merged Poincaré map and the switching surfaces by defining switching surfaces in equation (2.16) in the following form.

$$\boldsymbol{\sigma}_m(\mathbf{x}_m, \mathbf{u}, d_m) = \boldsymbol{\sigma}_{xm}\mathbf{x}_m + \boldsymbol{\sigma}_{um}\mathbf{u} + \boldsymbol{\sigma}_{dm}d_m + \boldsymbol{\sigma}_{cm} \tag{2.18}$$

This equation defines a set of switching surfaces that indicate the switching conditions for transitions out of topology m. $\boldsymbol{\sigma}_{xm}$ and $\boldsymbol{\sigma}_{um}$ are constant matrices that define how state variables and input variables influence determing the m^{th}

switching instant, $\boldsymbol{\sigma}_{dm}$ and $\boldsymbol{\sigma}_{cm}$ are constant vectors for various switching cases at the m^{th} switching instants.

By choosing switching surfaces in this way, Kriventsov was able to derive closed-form expressions for the monodromy matrix $\mathbf{H}_x$ and the control matrix $\mathbf{H}_u$ in the periodic steady state equation for a power converter system with piecewise constant inputs.

$$\mathbf{x}[k+1] = \mathbf{H}_x\mathbf{x}[k] + \mathbf{H}_u\mathbf{u}[k] \tag{2.19}$$

Closed-form expressions for the monodromy matrix $\mathbf{H}_x$ and the control matrix $\mathbf{H}_u$ of a general system with a constant input were obtained [60].

$$\mathbf{H}_x = \frac{\partial \mathbf{f}}{\partial \mathbf{x}} + \sum_{m=1}^{M-1} \sum_{\substack{\alpha_1>\cdots>\alpha_m \\ \alpha_i=1,\cdots M-1}} \left[\frac{\frac{\partial \mathbf{f}}{\partial d_{\alpha_m}} \cdot \prod_{k=1}^{m-1} \left(\frac{\partial \boldsymbol{\sigma}_{\alpha_k}}{\partial d_{\alpha_{k+1}}} \right) \cdot \frac{\partial \boldsymbol{\sigma}_{\alpha_m}}{\partial \mathbf{x}}}{(-1)^{m+1} \prod_{k=1}^{m} \left(\frac{\partial \boldsymbol{\sigma}_{\alpha_k}}{\partial d_{\alpha_k}} \right)} \right] \tag{2.20}$$

$$\mathbf{H}_u = \frac{\partial \mathbf{f}}{\partial \mathbf{u}} + \sum_{m=1}^{M-1} \sum_{\substack{\alpha_1>\cdots>\alpha_m \\ \alpha_i=1,\cdots M-1}} \left[\frac{\frac{\partial \mathbf{f}}{\partial d_{\alpha_m}} \cdot \prod_{k=1}^{m-1} \left(\frac{\partial \boldsymbol{\sigma}_{\alpha_k}}{\partial d_{\alpha_{k+1}}} \right) \cdot \frac{\partial \boldsymbol{\sigma}_{\alpha_m}}{\partial \mathbf{u}}}{(-1)^{m+1} \prod_{k=1}^{m} \left(\frac{\partial \boldsymbol{\sigma}_{\alpha_k}}{\partial d_{\alpha_k}} \right)} \right] \tag{2.21}$$

The derivative terms in equation (2.20) and (2.21) are expressed as follows.

$$\begin{aligned}
\frac{\partial \mathbf{f}}{\partial \mathbf{x}} &= \mathbf{\Pi}_1^M \\
\frac{\partial \boldsymbol{\sigma}_\alpha}{\partial \mathbf{x}} &= \boldsymbol{\sigma}_{x\alpha}\mathbf{\Pi}_1^\alpha \\
\frac{\partial \mathbf{f}}{\partial \mathbf{u}} &= \sum_{i=1}^{M} \mathbf{\Pi}_{i+1}^M \mathbf{\Psi}(\mathbf{A}_i, \mathbf{B}_i, \Delta_i) \\
\frac{\partial \boldsymbol{\sigma}_\alpha}{\partial \mathbf{u}} &= \boldsymbol{\sigma}_{x\alpha} \left[\sum_{i=1}^{\alpha} \mathbf{\Pi}_{i+1}^\alpha \mathbf{\Psi}(\mathbf{A}_i, \mathbf{B}_i, \Delta_i) \right] + \boldsymbol{\sigma}_{u\alpha} \\
\frac{\partial \mathbf{f}}{\partial d_\alpha} &= \mathbf{\Pi}_{\alpha+1}^M \left[\dot{\mathbf{X}}(\tau_\alpha^-) - \dot{\mathbf{X}}(\tau_\alpha^+) \right] \\
\frac{\partial \boldsymbol{\sigma}_\beta}{\partial d_\alpha} &= \begin{cases} \boldsymbol{\sigma}_{x\beta}\mathbf{\Pi}_{\alpha+1}^\beta \left[\dot{\mathbf{X}}(d_\alpha^-) - \dot{\mathbf{X}}(d_\alpha^+) \right] & \beta > \alpha \\ \boldsymbol{\sigma}_{x\alpha}\dot{\mathbf{X}}(d_\alpha^-) + \boldsymbol{\sigma}_{d\alpha} & \beta = \alpha \\ \mathbf{0} & \beta < \alpha \end{cases}
\end{aligned}$$

where

$$\begin{aligned}
\dot{\mathbf{X}}(d_\alpha^-) &= \mathbf{A}_\alpha \mathbf{X}_\alpha + \mathbf{B}_\alpha \mathbf{U} \\
\dot{\mathbf{X}}(d_\alpha^+) &= \mathbf{A}_{\alpha+1} \mathbf{X}_\alpha + \mathbf{B}_{\alpha+1} \mathbf{U} \\
\mathbf{\Pi}_p^q &= \prod_{i=p}^{q} \mathbf{\Phi}_i = \mathbf{\Phi}_q \cdot \mathbf{\Phi}_{q-1} \cdot \ldots \cdot \mathbf{\Phi}_p \\
\mathbf{\Phi}_i &= e^{\mathbf{A}_i \Delta_i} \\
\Delta_i &= \tau_i - \tau_{i-1} \\
\mathbf{\Psi}(\mathbf{A}, \mathbf{B}, t) &= \int_0^t e^{\mathbf{A}\tau} \mathbf{B} d\tau = \left(\mathbf{I}t + \frac{\mathbf{A}t^2}{2!} + \frac{\mathbf{A}^2 t^3}{3!} + \frac{\mathbf{A}^3 t^4}{4!} + \cdots \right) \mathbf{B}.
\end{aligned}$$

Based on the computation of these expressions, the monodromy matrix $\mathbf{H}_x$ and the control matrix $\mathbf{H}_u$ in equation (2.20) and (2.21) can be obtained for piecewise constant inputs. Then the switched state space model is converted to the discrete-time large signal model as equation (2.9) which can be used to calculate the periodic steady state response and analyzing its stability. Thus, the Floquet method provides a fast and accurate way of determining the switching sequence and stability of power converter systems via eigensystem analysis.

The existing Floquet method [54–56, 58, 59, 63] only applies to periodic system with piecewise constant inputs and provides steady state solution over one switching period. A late chapter focuses on extending the Floquet method to multi-period solver and systems with sinusoidal inputs.

Floquet Method Implementation in MATLAB A set of MATLAB codes for calculating the periodic steady state solution and monodromy matrix for SSSM was provided from previous research. Figure 2.12 shows the flow chart of the MATLAB implementation.

These codes require an SSSM, input signals, and initial guess of steady state solution. Then Newton-Raphson technique as described by equation (2.17) is used to calculate the switching sequence and monodromy matrix for each iteration. At the end of each iteration, the p norm of $\boldsymbol{\delta}$ is calculated, where $\boldsymbol{\delta}$ represents the difference of state variable vector between each iteration. Newton-Raphson iteration stops if $\| \boldsymbol{\delta} \|_p$ is less than a pre-defined value δ_0.

When calculating the switching sequence and monodromy matrix, there are

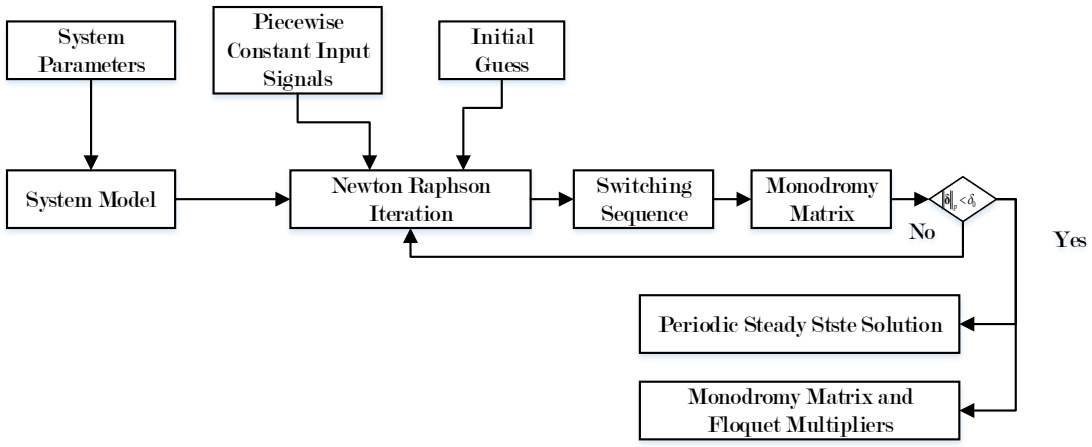

Figure 2.12. Flow chart of MATLAB implementation.

several methods for solving the state equation. A closed-form solution is derived in this project. This method is faster than the numerical routines provided in MATLAB, especially for sinusoidal input signals. The derivation of this closed-form solution appears in chapter 4.

2.3 Example of a Modeling of Buck Converter System

The buck converter system operating with current-mode control is shown in Figure 2.6. In many cases, it can be assumed that switching is an ideal process, which implies that there is zero voltage across an on-state switch, zero current through an off-state switch, and transitions between on and off states are instantaneous. Under this assumption, the power converter system can be modeled as a multi-topology system. Therefore it is desirable to use a switched state space model that includes an LTI model for each circuit topology along with a set of switching surfaces to determine when and in what manner transitions from one topology to another occur.

2.3.1 Switched State Space Model

Since the buck converter could operate in both CCM and DCM in practical applications, for generality, assume the power stage operates in DCM. So there are three circuit topologies: an on-state when the switch is closed, an off-state when the switch is open, and a DCM when the current through inductor becomes zero. These topologies are indicated as Top1, Top2, and Top3 in Figure 2.13.

Power Stage Model

Choose the state vector for the buck converter as $\mathbf{x}_p = [i_L \quad v_c]^T$ and the input vector as $\mathbf{u}_p = [v_d]$, then the buck converter during one switching cycle is modeled by a piecewise-LTI model as

$$\begin{aligned} \dot{\mathbf{x}}_p &= \mathbf{A}_{pm}\mathbf{x}_p + \mathbf{B}_{pm}\mathbf{u}_p \\ \mathbf{y}_p &= \mathbf{C}_p\mathbf{x}_p + \mathbf{D}_p\mathbf{u}_p \end{aligned} \tag{2.22}$$

where $m \in \{1, 2, 3\}$ is the topology index, and $\mathbf{A}_{pm}$ and $\mathbf{B}_{pm}$ are the state matrices and control matrices for the m^{th} circuit topology. The input variable vector $\mathbf{u}_p$ and output variable vector $\mathbf{y}_p$ are assumed to be independent of topology. The matrices $\mathbf{A}_{pm}$, $\mathbf{B}_{pm}$, $\mathbf{C}_p$, and $\mathbf{D}_p$ are expressed

$$\mathbf{A}_{p1} = \begin{bmatrix} -\frac{R_{load}r_{co}+R_{load}r_L+r_{co}r_L}{L(R_{load}+r_{co})} & -\frac{R_{load}}{L(R_{load}+r_{co})} \\ \frac{R_{load}}{C_o(R_{load}+r_{co})} & -\frac{1}{C_o(R_{load}+r_{co})} \end{bmatrix} \qquad \mathbf{B}_{p1} = \begin{bmatrix} \frac{1}{L} \\ 0 \end{bmatrix}$$

$$\mathbf{A}_{p2} = \begin{bmatrix} -\frac{R_{load}r_{co}+R_{load}r_L+r_{co}r_L}{L(R_{load}+r_{co})} & -\frac{R_{load}}{L(R_{load}+r_{co})} \\ \frac{R_{load}}{C_o(R_{load}+r_{co})} & -\frac{1}{C_o(R_{load}+r_{co})} \end{bmatrix} \qquad \mathbf{B}_{p2} = \begin{bmatrix} 0 \\ 0 \end{bmatrix}$$

$$\mathbf{A}_{p3} = \begin{bmatrix} 0 & 0 \\ 0 & -\frac{1}{C_o(R_{load}+r_{co})} \end{bmatrix} \qquad \mathbf{B}_{p3} = \begin{bmatrix} 0 \\ 0 \end{bmatrix}$$

$$\mathbf{C}_p = \left(\frac{R_{load}}{R_{load}+r_{co}}\right) \begin{bmatrix} r_c & 1 \end{bmatrix} \qquad \mathbf{D}_p = 0$$

Compensator Model

In order to regulate the output voltage against changes in reference value or the load, lead or lag compensators are used. A lead compensator can increase the stability or speed of response of a system; a lag compensator can reduce the steady-state error. These compensators are usually designed using a transfer function model for the system. Since the Floquet method uses a switched state space model as input, the compensator transfer function is converted into a state space model.

The phase-lead/lag compensator takes the difference between the reference output voltage v_o^{ref} and the actual output voltage v_o to generate a control signal v_c. Define the compensator state as $\mathbf{x}_c = [x_{ctr}]$ and input vector as $u_c = v_o^{ref} - v_o$, then the compensator is modeled as :

$$\begin{aligned} \dot{\mathbf{x}}_c &= \mathbf{A}_c\mathbf{x}_c + \mathbf{B}_c v_o^{ref} - \mathbf{B}_c\mathbf{C}_p\mathbf{x}_p \\ v_c &= \mathbf{C}_c\mathbf{x}_c + \mathbf{D}_c v_o^{ref} - \mathbf{D}_c\mathbf{C}_p\mathbf{x}_p \end{aligned} \tag{2.23}$$

where $\mathbf{A}_c$, $\mathbf{B}_c$, $\mathbf{C}_c$, and $\mathbf{D}_c$ are state space matrices of the compensator.

Closed-loop Model

Next, the state space model of closed-loop system is derived by combining equation (2.22) and equation (2.23). Choose state vector $\mathbf{x} = [\mathbf{x}_p^T \quad \mathbf{x}_c^T]^T$, input vector $\mathbf{u} = [v_d \quad v_o^{ref}]^T$, and output vector $\mathbf{y} = [v_o \quad i_L \quad v_{co} \quad v_c \quad \mathbf{x}_c^T]^T$. Then the closed-loop system of one switching cycle is modeled as

$$\begin{aligned} \dot{\mathbf{x}} &= \mathbf{A}_m\mathbf{x} + \mathbf{B}_m\mathbf{u} \\ \mathbf{y} &= \mathbf{C}\mathbf{x} + \mathbf{D}\mathbf{u} \end{aligned} \tag{2.24}$$

where

$$\mathbf{A}_m = \begin{bmatrix} \mathbf{A}_{pm} & \mathbf{0} \\ -\mathbf{B}_c\mathbf{C}_p & \mathbf{A}_c \end{bmatrix}$$

$$\mathbf{B}_m = \begin{bmatrix} \mathbf{B}_{pm} & \mathbf{0} \\ \mathbf{0} & \mathbf{B}_c \end{bmatrix}$$

$$\mathbf{C} = \begin{bmatrix} \mathbf{C}_p & 0 \\ \mathbf{I}_{2\times 2} & \mathbf{0}_{2\times 1} \\ -\mathbf{D}_c\mathbf{C}_p & \mathbf{C}_c \\ \mathbf{0}_{1\times 2} & 1 \end{bmatrix}$$

$$\mathbf{D} = \begin{bmatrix} \mathbf{0}_{3\times 1} & \mathbf{0}_{3\times 1} \\ \mathbf{0} & \mathbf{D}_c \\ 0 & 0 \end{bmatrix}$$

$m \in \{1, 2, 3\}$ is the topology index, representing on-state, off-state, and DCM state. $\mathbf{A}_m$ and $\mathbf{B}_m$ are the state matrices and control matrices for the m^{th} circuit topology.

2.3.2 Switching Surfaces

Switching instants between different topologies of the system are determined by one or more switching surfaces. These switching surfaces are defined as

$$\boldsymbol{\sigma}_m(\mathbf{x}, \mathbf{u}, d_m) = \mathbf{0} \tag{2.25}$$

where $\boldsymbol{\sigma}_m$ denotes a set of switching surfaces that indicate the instant $d_m T_s$ at which the system transitions from the m^{th} topology; T_s is the switching period and $d_m \in [0, 1)$ is the duty cycle. Possible transitions between topologies during one switching period are illustrated in Figure 2.13. σ_{ij} denotes the corresponding switching surface for the power converter transferring from i^{th} topology to j^{th} topology.

A linear choice of $\boldsymbol{\sigma}_m$, defined by Equation (2.26), supports many practical systems and allows for closed-form expressions for the monodromy matrix and the control matrix.

$$\boldsymbol{\sigma}_m(\mathbf{x}, \mathbf{u}, d_m) = \boldsymbol{\sigma}_{xm}\mathbf{x} + \boldsymbol{\sigma}_{um}\mathbf{u} + \boldsymbol{\sigma}_{dm}d_m + \boldsymbol{\sigma}_{cm} \tag{2.26}$$

$\boldsymbol{\sigma}_{xm}$ and $\boldsymbol{\sigma}_{um}$ are constant matrices that define which state variables and inputs are used to determine the m^{th} switching instant, $\boldsymbol{\sigma}_{dm}$ and $\boldsymbol{\sigma}_{cm}$ are constant column vectors for various switching cases at the m^{th} switching instants. For example, the

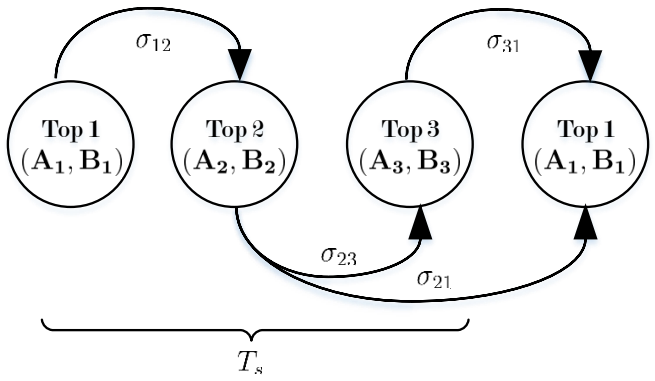

Figure 2.13. Transition between circuit topologies, where Top1 is on-state, Top2 is off-state, and Top3 is DCM state.

switching surfaces of the closed-loop system are derived as

$$\begin{aligned}
\sigma_1 &= v_c - m_{sc}T_s d_1 - r'_s i_L \\
&= \left[\begin{array}{c|c} \left[\left(\begin{array}{cc} -r'_s & 0 \end{array}\right) - \mathbf{D}_c\mathbf{C}_p\right] & \mathbf{C}_c \end{array}\right]\mathbf{x} + \left[\begin{array}{c|c} 0 & \mathbf{D}_c \end{array}\right]\mathbf{u} - m_{sc}T_s d_1 \\
\boldsymbol{\sigma}_2 &= \left[\begin{array}{ccc} 1 & 0 & 0 \\ 0 & 0 & 0 \end{array}\right]\mathbf{x} + \left[\begin{array}{cc} 0 & 0 \\ 0 & 0 \end{array}\right]\mathbf{u} + \left[\begin{array}{c} 0 \\ -1 \end{array}\right] d_2 + \left[\begin{array}{c} 0 \\ 1 \end{array}\right] \\
\sigma_3 &= 1 - d_3
\end{aligned} \tag{2.27}$$

where r'_s is the product of current sense resistor r_s and the gain of op-amp and m_{sc} is the slope of the slope compensation signal v_{sc} in Figure 2.6. The SSSM of the current-mode controlled power converter is derived by combining piecewise-LTI models defined by equation (2.24) and switching surfaces defined by equation (2.27). This SSSM works as the input to the Floquet method, which returns the periodic steady state response and monodromy matrix.

Chapter 3

Background of Design Optimization of Power Converter Systems

The tension between increasing performance and efficiency while decreasing volume is the major concern in power converter system design. To achieve a good balance, the design of power converter systems can be treated as constrained optimization problems that can be formulated as:

$$\min_{\mathbf{x}} f(\mathbf{x}) \tag{3.1}$$

subject to

$$\begin{aligned} \mathbf{g}(\mathbf{x}) &= \mathbf{0} \\ \mathbf{h}(\mathbf{x}) &\leq \mathbf{0} \end{aligned}$$

where $\mathbf{x} \in \mathbf{R}^n$ is the state variable vector of the power converter system, $f : \mathbf{R}^n \rightarrow \mathbf{R}$ is the objective function, $g : \mathbf{R}^n \rightarrow \mathbf{R}^m$ and $h : \mathbf{R}^n \rightarrow \mathbf{R}^p$ represent equality constraints and inequality constraints respectively.

Broadly speaking, optimization algorithms can be categorized into two groups: classical algorithm and more recent evolutionary algorithms. With the help of classical optimization, performance of power converter systems can be optimized using Newton-like algorithms given relatively uncomplicated models. First, researchers were dedicated to power stage optimizing design [64–66], where effi-

ciency or maximum power was the design objective. The sequential unconstrained minimization technique and the augmented Lagrangian penalty function technique for power converter design optimization were discussed in [67, 68]. Monte Carlo search method was used in [69] to speed up the design process of dc-to-dc converters. The optimal efficiency and switching frequency of power stage was obtained by minimizing a third-order equation of switching frequency in [70]. Optimizing designs for continuous-conduction mode and discontinuous-conduction mode were separately derived [71] using fixed frequency regulation and variable frequency regulation respectively. Acceptability boundary curves [72] were used to characterize the tradeoff between performance and volume of system. Instead of focusing on design of power stage, some research concentrated on using control theory to regulate the power converter system and achieve optimal performance. By adding feedback path of output current and feedforward path of input voltage, near-optimum dynamics of a dc-dc converter is obtained in [73]. Using control theory, the controller could be chosen as phase-lead/lag, PID, adaptive controllers. The gains of such controllers were optimized to achieve best transient responses of various power converter systems [74–77]. The performance of the converter system would be changed by introducing the input filter, since it interacts with feedback loop. The detrimental effect of an input filter is a function of filter parameters and supply voltage. Design criteria for parameters were provided in [22, 25–27]. However, these criteria only provide upper or lower bounds for input filter design. Optimal selection of input filter and damping resistance was determined in [27, 78]. Raggl, et al. [79] presented optimization for compliance with EMC standards of input filter. Besides volume, other factors such as converter efficiency, input voltage ripple, and switching frequency are expected to be optimized when designing power converter systems. To obtain the optimal performance for converter systems, engineers usually refer to aforementioned papers or conduct a parameter study of input filter that is very time consuming.

Evolutionary optimization algorithms have emerged as a powerful tool for optimization problems since the 1960's. Evolutionary algorithms have advantages that they can find a global optimum, can convergence quickly, and are robust. They have become a well developed methodology for optimization problems. Particle swarm optimization was applied to optimize the performance of different types

of controllers for power converter systems in [80–85]. Neural network was used to optimize the performance of dc-dc boost converter system in [86, 87]. Ant colony optimization model [88] was proposed to optimize the control of rectifier systems. Some researchers comnined these optimization techniques to improve the performance of these systems in [89–91]. Genetic algorithms (GAs) have received attention in power system optimization, since they have the ability to deal with discrete variables. Helali, et al. [92] minimized a discrete cost function for dc-dc buck converter systems. Parameters of different types of controller were optimized using GAs for various power converter systems in [93–98]. Multi-objective optimization was examined using GAs in [99–101] for dc-dc converter systems. But a meaningful explanation of weight coefficients were hardly provided. Optimal dynamic response was achieved [102] by using GAs to LQR control. Optimization of inductor based on GAs was presented for a H-bridge multilevel converter [103]. In [104, 105], optimal input filters were designed based on GAs for ac-ac converter systems. Therefore, a fast and optimal design procedure by intelligent algorithms is favorable when designing converter systems.

3.1 Classical Optimization Techniques

Lagrange is one of the most important contributors to the theory of optimization in the presence of constraints. The concepts of Lagrange multipliers, the necessary and the sufficient Kuhn-Tucker conditions for optimality are central to discussions on constrained optimization problems [106–108].

The methods of solving constrained optimization problem are categorized into two groups. The first group focuses on transforming a constrained problem into unconstrained problems. They are (exact or sequential) penalty function methods and (exact or sequential) augmented Lagrangian methods. Sequential methods find the solution from a sequence of subproblems. The exact methods find the optimal solution of the original problem the same as the optimal solution of an unconstrained problem under suitable assumptions. Another category of methods discover the optimal solutions of the original problem by transforming it into a sequence of constrained quadratic problems. So it is necessary to use unconstrained optimization routines to locate the optimal solution of constrained optimization

problems.

In practical implementations, it is important to analyze the complexity of the algorithms such as inversion of matrices and the speed of convergence. It is easy to implement sequential penalty functions methods, but it suffers from large penalties. Sequential augmented Lagrangian functions calculate solutions with a faster speed of convergence. The exact penalty function methods require the inversion of a matrix of dimension equal to the number of constraints, hence are limited to a small number of constraints. Recursive quadratic programming methods need to find the solution of a constrained quadratic programming problem at each step. Each method has its own advantages and disadvantages. The selection of method for solving constrained optimization problems depends on the nature of the problem.

3.2 Genetic Algorithms Technique

For power electronic systems, the classical optimization techniques discussed in Section 3.1 face difficulties. In particular the type of the inductor core leads to different inductance curve and volume of capacitor is discrete valued, hence $\mathbf{f}(\mathbf{x})$, $\mathbf{g}(\mathbf{x})$ or $\mathbf{h}(\mathbf{x})$ in equation (3.1) may not be differentiable and the gradient information may be impossible to obtain and objective function may be complicated with several local optima. It turns out that some evolutionary algorithms may be appropriate for these problems, particularly genetic algorithms (GAs). They are search procedures mimicking the mechanisms of natural genetic selection and reproduction. Unlike gradient searches, GAs optimizers can handle discontinuous and non-differentiable functions. It has been proved successful when one tries to solve engineering design problems including power electronic systems, electromagnetic systems, and communication systems. The basics of GAs [109–112] are summarized as follows.

In GAs, a population of potential solutions evolves toward to global optimum using operators inherited from Darwinian concepts. This evolution generates individuals that are better suited to the problem as a result of a fitness-weighted selection, recombination and mutation of the existing population. Some important terminology and concepts of GAs are shown in Table 3.1. There are four major stages in GAs: representation, evaluation, reproduction, termination as illustrated

Gene	Coded Optimization parameters
Chromosome	Individual solution consisting of genes
Population	Set of trial solutions
Generation	GAs iteration
Parent	Population of current generation
Child	Population of next generation
Fitness	Objective values of individuals

Table 3.1. Terminology of genetic algorithms.

in Figure 3.1.

3.2.1 Population Representation and Initialization

GAs do optimization search using chromosomes that are usually encoded in binary or gray coding. The chromosome values are uniquely mapped onto the problem domain (optimization variables). Each design variable is analogous to gene. Each individual represents a point in a search space and a possible solution. Figure 3.2 represents the mechanism of encoding and decoding of optimization parameters.

Having encoded the optimization parameters as genes and created chromosomes as a string of genes, an initial population is generated randomized manner that uniformly distributes numbers in the desired range. Subsequently, the population of individuals is sent to the process of evaluation.

3.2.2 Fitness Evaluation

In this process, the encoded chromosomes are first decoded into the solution domain. An objective function is used to quantify how each individual performs in the solution domain. This is only used as an intermediate stage to determine the performance of an individual in GAs. Then, another function called the fitness function $F(\mathbf{x})$ maps the value of the objective function to a non-negative number that is referred to as the fitness value.

$$F(\mathbf{x}) = g(f(\mathbf{x}))$$

where $f(\cdot)$ is the objective function. The common choices of $g(\cdot)$ are proportional fitness assignment and linear transformation.

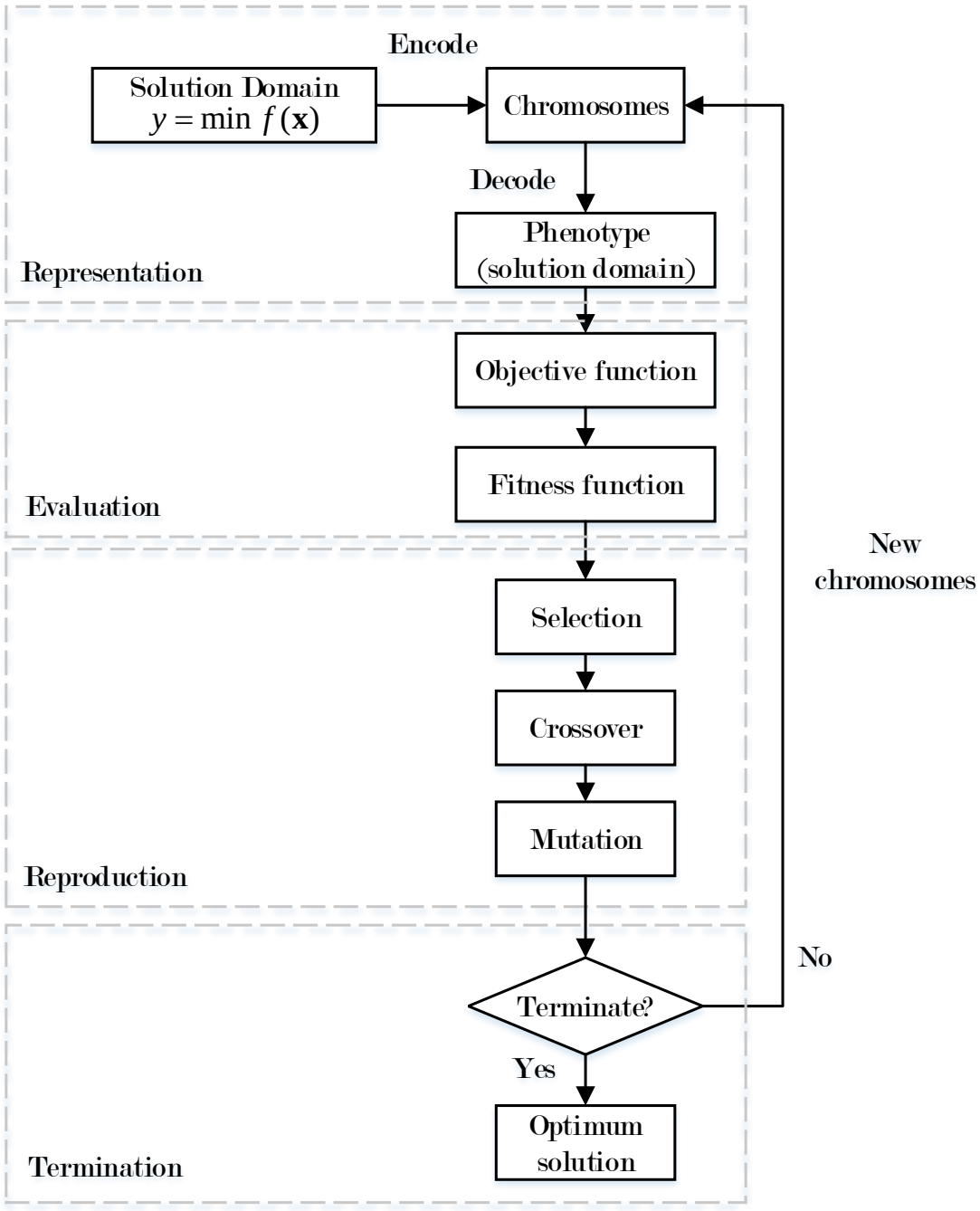

Figure 3.1. Genetic algorithms flow chart.

3.2.3 Population Reproduction

With the help of objective function and fitness function, a fitness score is assigned to each solution representing the abilities of an individual. Once the individuals

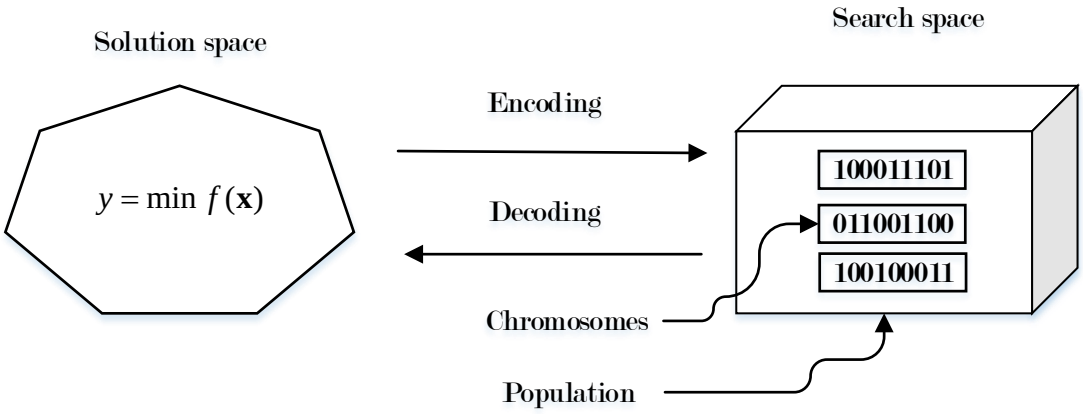

Figure 3.2. Representation of optimization parameters [113].

have been assigned a fitness value, they can be chosen from the population, with a probability according to their relative fitness values. Individuals with good fitness values have a greater chance to be selected. Consequently, highly fit solutions are given more opportunities to reproduce. Children inherit characteristics from each parent by combining information from parents' chromosomes. The frequently used operators for selection are roulette wheel selection, stochastic sampling with replacement, and stochastic universal sampling.

Then GAs reproduce the next generation through the fitness-weighed selection of individuals from the population. Parents are selected to mate based on their fitness values. Individuals with low fitness values in the population die and are replaced by the new solutions, eventually creating new children. The basic operator for producing children in GAs is crossover. It is used to exchange genetic information between pairs of individuals, thus new individuals have partial genetic information of their parents'. Multi-point crossover is one of the most popular reproduction mechanisms. It encourages wider exploration of the search space, thus making the GAs more robust. Single-point crossover, uniform crossover, shuffle, intermediate recombination, and line recombination are among other reproduction operators.

Mutation is randomly applied with low probability and modifies elements in the chromosomes. The role of mutation is to recover good genetic information that may be lost through the action of selection and crossover and to ensures that

the probability of searching a particular subspace of the problem space is never zero. This tends to keep GAs from converging to a local optimum. In general, it is good to have both crossover and mutation. Crossover makes a big jump to an area somewhere in between two parent areas, while mutation creates random small diversions, thereby staying near the parent. Trade mutation and reorder mutation are also used to increase diversity in search space.

3.2.4 Termination of Genetic Algorithms

New generations of solutions are produced containing more good genes than that in a previous generation. So the average performance of individuals is expected to improve. This process is repeated until a termination condition is met. Common practice to terminate GAs are

- A specified number of generations is reached.
- A specified running time of Genetic Algorithm is reached.
- Objective value is lower than a threshold.
- Solution has converged and deviation between generations is lower than a threshold.

Eventually, once the population has converged and is not producing children noticeably different from parents, the algorithm is said to have converged to a set of solutions to the problem.

3.3 Discussion

In this section, two substantially different groups of approaches, classical optimization techniques and GAs, are discussed to solve constrained optimization problems. GAs is a stochastic search for solutions in parallel based on an encoding of optimization parameters. Classical optimization techniques are highly dependent on the initial conditions, while GAs are largely independent of the starting point. In fact, initial guess are randomized for GAs. Traditional optimization algorithms can locate the minimum with relatively fast convergence. However, this usually comes

at the cost of placing constraints, such as differentiability and continuity, which are hard to deal with in practice. Quite on the contrary, GAs are independent of these constraints, which means they are more robust at dealing with discontinuity and constrained parameters. The disadvantage is the slower convergence as they do not take the advantage of gradients during the search process.

In power electronics design, the ultimate goal is to find the best solution or global minimum and the whole design process is off-line. Convergence rate is not as important as finding a solution. Thus GAs are favored over classical methods. They can yield either a global or near-global minimum and find solutions where classical methods cannot.

Chapter 4

Enhancements to Floquet Method for Power Converter System Analysis

Switched power converter systems are usually periodic and can be modeled using a switched state space model (SSSM) as described in Section 2.2.1. A given system transitions among the various circuit topologies according to the switching behavior defined by the controller/modulator and the diode switch characteristics. The Floquet method [52, 62] is a useful technique to analyze such systems and has been used to assess stability and steady state performance in previous research [54–60,63]. The main emphasis of this chapter is on extending the existing Floquet method to include a multi-period solver and admit sinusoidal input signals.

4.1 Multi-period Solver

The previously developed Floquet method is limited to calculating the periodic steady state response and monodromy matrix of a system over a single period. Thus, for problems such as sub-harmonic oscillation in current-mode controlled converters it does not determine the actual periodic steady state response but rather a 1-period periodic steady state solution. The solution itself is of limited significance but eigenanalysis of the associated monodromy matrix can be used to reveal the lack of 1-period stability.

A multi-period solver permits determination of the actual periodic steady state response at sub-harmonic frequencies. A multi-period solver also permits

calculation of the system response to input signals or disturbance signals that are sub-harmonic to the switching frequency. To find multi-period solutions, the SSSM in equation (2.24) and (2.27) must be modified to incorporate more topologies, as well as the set of switching surfaces over more than one switching period T_s.

4.1.1 Derivation

To derive a general multi-period SSSM we consider the particular case of a current-mode controlled buck converter shown in Figure 2.6 as an example. Let us first study the transitions between topologies for a 2-period solver, which are illustrated in Figure 4.1. The new switching period is defined as $T_s^* = 2T_s$.

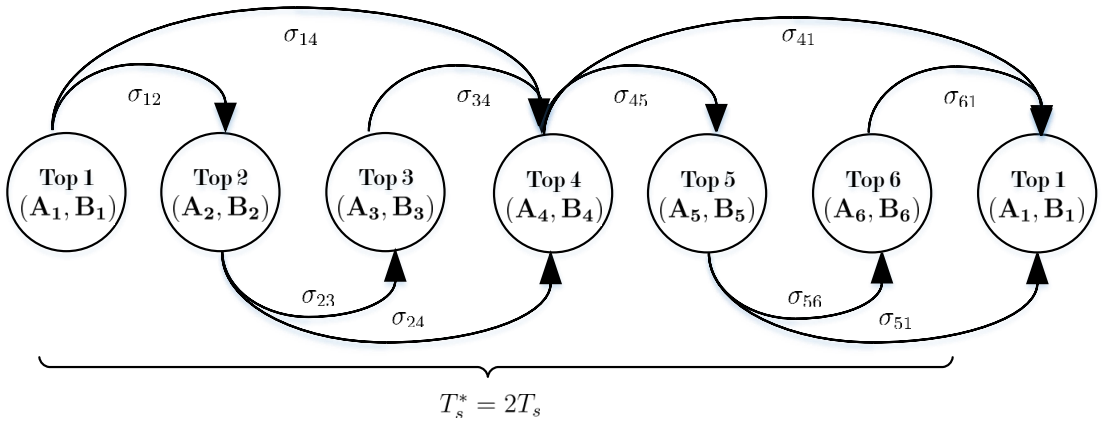

Figure 4.1. Transition of topologies of a buck converter (2-period case).

For generality, we continue to assume that the power stage may operate in DCM, so there are six topologies and can be organized into three groups: an on-state when the switch is closed, an off-state when the switch is open, and a DCM state once the current through inductor becomes zero. The on-state topology is modeled by $(\mathbf{A}_1, \mathbf{B}_1)$ or $(\mathbf{A}_4, \mathbf{B}_4)$; the off- state topology is modeled by $(\mathbf{A}_2, \mathbf{B}_2)$ or $(\mathbf{A}_5, \mathbf{B}_5)$; and the DCM topology is modeled by $(\mathbf{A}_3, \mathbf{B}_3)$ or $(\mathbf{A}_6, \mathbf{B}_6)$.

In the 2-period model, the state space matrices $(\mathbf{A}_p, \mathbf{B}_p, \mathbf{C}_p, \mathbf{D}_p)$ of a buck converter remain the same as those in the original power stage model. The phase-lead/lag compensator generates signal v_c in the same way and is modeled in state space as $(\mathbf{A}_c, \mathbf{B}_c, \mathbf{C}_c, \mathbf{D}_c)$. Choosing state vector $\mathbf{x} = [i_L \quad v_{co} \quad \mathbf{x}_c^T]^T$, input vector $\mathbf{u} = [V_d \quad V_o^{ref}]^T$, and output vector $\mathbf{y} = [v_o \quad i_L \quad v_{co} \quad v_c \quad \mathbf{x}_c^T]^T$, so the overall

close-loop system is defined by the following piecewise-LTI model.

$$\begin{aligned}\dot{\mathbf{x}}(t) &= \mathbf{A}_m\mathbf{x}(t) + \mathbf{B}_m\mathbf{u}(t) \qquad (k + d^{*k}_{m-1})T^*_s \le t \le (k + d^{*k}_m)T^*_s \\ \mathbf{y}(t) &= \mathbf{C}\mathbf{x}(t) + \mathbf{D}\mathbf{u}(t) \qquad 0 \le d^{*k}_m \le 1 \qquad m = 1, \cdots, 6\end{aligned}$$

where

$$\mathbf{A}_1 = \mathbf{A}_4 = \begin{bmatrix} \mathbf{A}_{p1} & \mathbf{0}_{2\times1} \\ -\mathbf{B}_c\mathbf{C}_p & \mathbf{A}_c \end{bmatrix} \qquad \mathbf{A}_2 = \mathbf{A}_5 = \begin{bmatrix} \mathbf{A}_{p2} & \mathbf{0}_{2\times1} \\ -\mathbf{B}_c\mathbf{C}_p & \mathbf{A}_c \end{bmatrix}$$

$$\mathbf{A}_3 = \mathbf{A}_6 = \begin{bmatrix} \mathbf{A}_{p3} & \mathbf{0}_{2\times1} \\ -\mathbf{B}_c\mathbf{C}_p & \mathbf{A}_c \end{bmatrix} \qquad \mathbf{B}_1 = \mathbf{B}_4 = \begin{bmatrix} \mathbf{B}_{p1} & \mathbf{0}_{2\times1} \\ 0 & \mathbf{B}_c \end{bmatrix}$$

$$\mathbf{B}_2 = \mathbf{B}_5 = \begin{bmatrix} \mathbf{B}_{p2} & \mathbf{0}_{2\times1} \\ 0 & \mathbf{B}_c \end{bmatrix} \qquad \mathbf{B}_3 = \mathbf{B}_6 = \begin{bmatrix} \mathbf{B}_{p3} & \mathbf{0}_{2\times1} \\ 0 & \mathbf{B}_c \end{bmatrix}$$

$$\mathbf{C} = \begin{bmatrix} \mathbf{C}_p & 0 \\ \mathbf{I}_{2\times2} & \mathbf{0}_{2\times1} \\ -\mathbf{D}_c\mathbf{C}_p & \mathbf{C}_c \\ \mathbf{0}_{1\times2} & 1 \end{bmatrix} \qquad \mathbf{D} = \begin{bmatrix} \mathbf{0}_{3\times1} & \mathbf{0}_{3\times1} \\ \mathbf{0} & \mathbf{D}_c \\ 0 & 0 \end{bmatrix}$$

In Figure 4.1, there are two possible transitions from the on-state topology: either to the off-state topology (σ_{12}) or to the next on-state topology (σ_{14}). Transitions from the off-state topology can be to the DCM topology (σ_{23}) or to the next on-state topology (σ_{24}). The only transition from the DCM topology is to the next on-state topology (σ_{34}). Thus, for the 2-period SSSM, the switching surfaces of the closed-loop feedback system are defined as:

$$\begin{aligned}\boldsymbol{\sigma}_1 &= \begin{bmatrix} \begin{bmatrix} -r'_s & 0 \end{bmatrix} - \mathbf{D}_c\mathbf{C}_p \\ \mathbf{0}_{1\times2} \end{bmatrix} \begin{matrix} \mathbf{C}_c \\ \mathbf{0} \end{matrix} \end{bmatrix} \mathbf{x}(t) + \begin{bmatrix} 0 & \mathbf{D}_c \\ 0 & \mathbf{0} \end{bmatrix} \mathbf{u}(t) + \begin{bmatrix} -m_{sc}T_s \\ -1 \end{bmatrix} d^*_1 + \begin{bmatrix} 0 \\ \frac{1}{2} \end{bmatrix} \\ \boldsymbol{\sigma}_2 &= \begin{bmatrix} 1 & 0 & 0 \\ 0 & 0 & 0 \end{bmatrix} \mathbf{x}(t) + \begin{bmatrix} 0 & 0 \\ 0 & 0 \end{bmatrix} \mathbf{u}(t) + \begin{bmatrix} 0 \\ -1 \end{bmatrix} d^*_2 + \begin{bmatrix} 0 \\ \frac{1}{2} \end{bmatrix}\end{aligned}$$

$$
\begin{aligned}
\sigma_3 &= \frac{1}{2} - d_3^* \\
\boldsymbol{\sigma}_4 &= \begin{bmatrix} \left[\begin{pmatrix} -r_s' & 0 \end{pmatrix} - \mathbf{D}_c\mathbf{C}_p\right] & \mathbf{C}_c \\ \mathbf{0}_{1\times 2} & \mathbf{0} \end{bmatrix} \mathbf{x}(t) + \begin{bmatrix} 0 & \mathbf{D}_c \\ 0 & \mathbf{0} \end{bmatrix} \mathbf{u}(t) + \begin{bmatrix} -m_{sc}T_s - \frac{1}{2}m_{sc}T_s \\ -1 \end{bmatrix} d_4^* + \begin{bmatrix} 0 \\ 1 \end{bmatrix} \\
\boldsymbol{\sigma}_5 &= \begin{bmatrix} 1 & 0 & 0 \\ 0 & 0 & 0 \end{bmatrix} \mathbf{x}(t) + \begin{bmatrix} 0 & 0 \\ 0 & 0 \end{bmatrix} \mathbf{u}(t) + \begin{bmatrix} 0 \\ -1 \end{bmatrix} d_5^* + \begin{bmatrix} 0 \\ 1 \end{bmatrix} \\
\sigma_6 &= 1 - d_6^*.
\end{aligned}
$$

Supplying this new piecewise-LTI model and new set of switching surfaces as input to the existing 1-period Floquet method yields a periodic steady state response in which two periods of the actual system have been compressed into one period for the solver.

Multi-period Solver

Having illustrated how to rebuild a 1-period SSSM into a 2-period SSSM, certain pattern for multi-period solver can be observed. Possible transitions between circuit topologies for multi-period solver are illustrated in Figure 4.2.

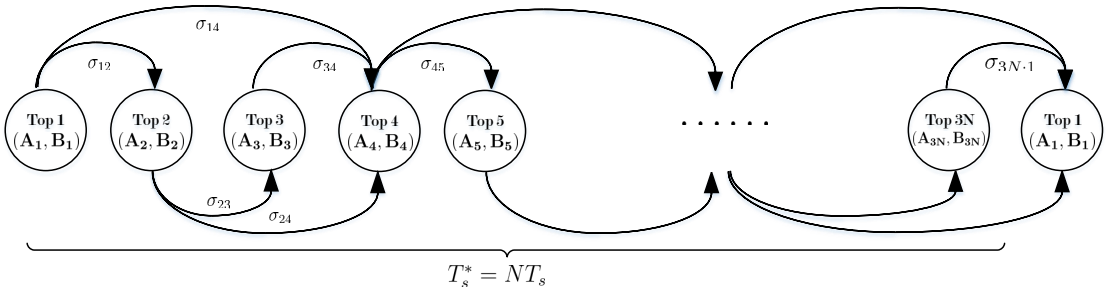

Figure 4.2. Transition of topologies of a buck converter (multi-period case).

There are $3N$ circuit topologies in this model where N is the multiple number of original switching period. Topologies $3n+1, n = 0, \cdots, N-1$ represent the on-state topologies; topologies $3n+2$ represent the off-state topologies; and topologies $3n+3$ represent the DCM topologies. For each group of these topologies, the piecewise-LTI matrices remain the same as the original ones.

$$
\begin{aligned}
(\mathbf{A}_{\{1,\cdots,3n+1\}}, \mathbf{B}_{\{1,\cdots,3n+1\}}, \mathbf{C}_{\{1,\cdots,3n+1\}}, \mathbf{D}_{\{1,\cdots,3n+1\}}) &= (\mathbf{A}_{1,original}, \mathbf{B}_{1,original}, \mathbf{C}_{1,original}, \mathbf{C}_{1,original}) \\
(\mathbf{A}_{\{2,\cdots,3n+2\}}, \mathbf{B}_{\{2,\cdots,3n+2\}}, \mathbf{C}_{\{2,\cdots,3n+2\}}, \mathbf{D}_{\{2,\cdots,3n+2\}}) &= (\mathbf{A}_{2,original}, \mathbf{B}_{2,original}, \mathbf{C}_{2,original}, \mathbf{D}_{2,original}) \\
(\mathbf{A}_{\{3,\cdots,3n+3\}}, \mathbf{B}_{\{3,\cdots,3n+3\}}, \mathbf{C}_{\{3,\cdots,3n+3\}}, \mathbf{D}_{\{3,\cdots,3n+3\}}) &= (\mathbf{A}_{3,original}, \mathbf{B}_{3,original}, \mathbf{D}_{3,original}, \mathbf{D}_{3,original})
\end{aligned}
$$

Thus, the multi-period system can be described by the following piecewise-LTI model.

$$
\begin{aligned}
\dot{\mathbf{x}}(t) &= \mathbf{A}_m\mathbf{x}(t) + \mathbf{B}_m\mathbf{u}(t) \qquad (k + d_{m-1}^{*k})T_s^* \le t \le (k + d_m^{*k})T_s^* \\
\mathbf{y}(t) &= \mathbf{C}_m\mathbf{x}(t) + \mathbf{D}_m\mathbf{u}(t) \qquad 0 \le d_m^{*k} \le 1 \qquad m = 1, \cdots, 3N
\end{aligned} \tag{4.1}
$$

Transitions from the on-state topology could be either to the off-state topology or to the next on-state topology. Switching surfaces for those transitions from topologies $\{1, 4, \cdots, 3n+1\}$ have similar form. Then, transitions from the off-state topology can be to the DCM topology or to the next on-state topology. From the DCM topology, the system could transition to the next on-state topology. Also, similar law can be observed in switching surfaces for those transitions from topologies $\{2, 5, \ldots\ 3n+2\}$ and $\{3, 6, \ldots\ 3n+3\}$.

For a multi-period solver, the solver switching period is defined as $T_s^* = NT_s$. Consequently the new duty cycle d_m^* is re-defined by the following map.

$$
d_m = N(d_m^* - \frac{n}{N}) \tag{4.2}
$$

New switching surfaces are obtained by substituting d_m in equation (2.26) with the expression for d_m^* in equation (4.2).

$$
\begin{aligned}
\boldsymbol{\sigma}_m(\mathbf{x}, \mathbf{u}, d_m) &= \boldsymbol{\sigma}_{xm}\mathbf{x} + \boldsymbol{\sigma}_{um}\mathbf{u} + \boldsymbol{\sigma}_{dm}d_m + \boldsymbol{\sigma}_{cm} \\
&= \boldsymbol{\sigma}_{xm}\mathbf{x} + \boldsymbol{\sigma}_{um}\mathbf{u} + \boldsymbol{\sigma}_{dm}N(d_m^* - \frac{n}{N}) + \boldsymbol{\sigma}_{cm} \\
&= \boldsymbol{\sigma}_{xm}\mathbf{x} + \boldsymbol{\sigma}_{um}\mathbf{u} + N\boldsymbol{\sigma}_{dm}d_m^* + \boldsymbol{\sigma}_{cm} - n\boldsymbol{\sigma}_{dm} \\
&= \boldsymbol{\sigma}_{xm}\mathbf{x} + \boldsymbol{\sigma}_{um}\mathbf{u} + \boldsymbol{\sigma}_{dm}^*d_m^* + \boldsymbol{\sigma}_{cm}^*
\end{aligned} \tag{4.3}
$$

where $\boldsymbol{\sigma}_{dm}^* = N\boldsymbol{\sigma}_{dm}$ and $\boldsymbol{\sigma}_{cm}^* = \boldsymbol{\sigma}_{cm} - n\boldsymbol{\sigma}_{dm}$.

The combination of the new piecewise-LTI model in equation (4.1) and the new set of switching surfaces in equation (4.3) that incorporates $3N$ topologies makes it

possible to calculate the periodic steady state response of power converter systems. Then using this multi-period SSSM as input to the existing Floquet method, low frequency sub-harmonic oscillations can be captured, where conventional small signal analysis and the existing single-period Floquet method fail.

4.2 Extension to Sinusoidal Inputs

In practical applications, disturbances are an issue that must be addressed. Often disturbance signals are modeled by sinusoidal signals. For example, $\tilde{v}_o^{ref}$ in Figure 4.3 represents a disturbance to the feedback signal of the power converter system. Moreover, to perform frequency-domain analysis of an SSSM, the input signal should be a sinusoidal one. The Floquet method can be modified to admit sinusoidal input signals in addition to piecewise constant input signals.

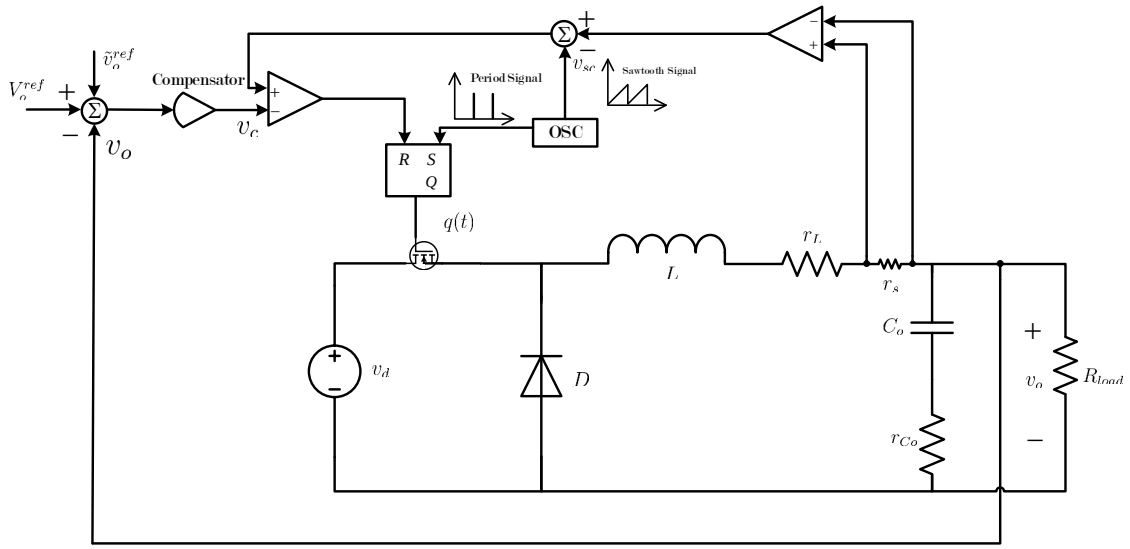

Figure 4.3. Current-mode controlled buck converter with sinusoidal disturbances.

4.2.1 Redefined Poincaré Map

In this section, the existing Floquet method is extended to admit sinusoidal input signals. A power converter system is still described by an SSSM model.

$$\begin{aligned} \dot{\mathbf{x}}_m(t) = \mathbf{A}_m\mathbf{x}_m(t) + \mathbf{B}_m\mathbf{u}(t) \qquad & (k + d^k_{m-1})T_s \le t \le (k + d^k_m)T_s \\ & 0 \le d^k_m \le 1 \qquad m = 1, 2, \ldots, M \end{aligned} \tag{4.4}$$

where column vector $\mathbf{x}$, matrices $\mathbf{A}_m$, $\mathbf{B}_m$, d^k_m, and T_s are defined the same as those in equation (2.10). The input $\mathbf{u}(t) \in \mathbb{R}^P$ contains sinusoidal input signals and constant input signals, where P is the number of inputs. The time-varying input $\mathbf{u}(t)$ can be divided into two components: time-varying signals and constant signals.

$$\mathbf{u}(t) = \hat{\mathbf{U}}(t)\underline{\mathbf{u}} \tag{4.5}$$

where $\hat{\mathbf{U}}(t)$ is the time-varying part containing sinusoidal signals and $\underline{\mathbf{u}}$ is the constant part. Using this equation, along with initial condition $\mathbf{x}^0_m$, the state trajectory during the m^{th} circuit topology of the k^{th} period can be rewritten as:

$$\mathbf{x}_m(t) = \mathbf{\Phi}_m(t, t_0)\mathbf{R}_m\mathbf{x}^0_m + \hat{\mathbf{\Psi}}_m(t, t_0)\underline{\mathbf{u}} \tag{4.6}$$

where

$$\begin{aligned} \mathbf{\Phi}_m &= e^{\mathbf{A}_m(t-t_0)} \\ \hat{\mathbf{\Psi}}_m &= \int_{t_0}^{t} \mathbf{\Phi}_m(t, \tau)\mathbf{B}_m\hat{\mathbf{U}}(t - \tau)d\tau \\ t_0 &= (k + d_{m-1})T_s. \end{aligned}$$

In equation (4.6), $\mathbf{R}_m$ is referred as projection matrix; it maps the state vector in the m^{th} topology to the next one. Then taking $\mathbf{x}_m$ as a new initial value for the next topology $m + 1$ and iteratively using equation (4.6) for all remaining topologies through the last topology, the response at the end of the last topology in k^{th} period is obtained by the following equation.

$$\mathbf{x}_M[(k + 1)T_s] = \mathbf{\Pi}^M_1\mathbf{x}^0_1[kT_s] + \hat{\mathbf{\Theta}}_M\underline{\mathbf{u}} \tag{4.7}$$

where

$$\begin{aligned}\mathbf{\Pi}_p^q &= \prod_{i=p}^{q} \mathbf{\Phi}_i(\Delta_i)\mathbf{R}_i \\ \hat{\mathbf{\Theta}}_q &= \sum_{i=1}^{q} \mathbf{\Pi}_{i+1}^q \hat{\mathbf{\Psi}}_i(\hat{\mathbf{U}}) \\ \Delta_i &= d_i - d_{i-1} \quad i \in \{1, 2, \cdots, M\}.\end{aligned}$$

The values of state variables at the end of k^{th} period are the same as those at the beginning of the first topology of $k+1$ period. So with periodic sampling, $\mathbf{x}_1[k] = \mathbf{x}_1(kT_s)$, the redefined Poincaré map over one switching cycle for sinusoidal input case is elaborated as below.

$$\begin{aligned}\mathbf{x}_1[k+1] &= \hat{\mathbf{f}}(\mathbf{x}_1[k], \underline{\mathbf{u}}[k], \mathbf{d}) \\ &= \mathbf{\Pi}_1^M \mathbf{x}_1[k] + \hat{\mathbf{\Theta}}_M \underline{\mathbf{u}}[k] \end{aligned} \tag{4.8}$$

Because the input signal is time-varying, the switching surfaces must be modified using equation (4.5)

$$\begin{aligned}\boldsymbol{\sigma}_m(\mathbf{x}, \mathbf{u}, d_m) &= \boldsymbol{\sigma}_{xm}\mathbf{x} + \boldsymbol{\sigma}_{um}\mathbf{u}(t) + \boldsymbol{\sigma}_{dm}d_m + \boldsymbol{\sigma}_{cm} \\ &= \boldsymbol{\sigma}_{xm}\mathbf{x} + \boldsymbol{\sigma}_{um}\hat{\mathbf{U}}(t)\underline{\mathbf{u}} + \boldsymbol{\sigma}_{dm}d_m + \boldsymbol{\sigma}_{cm} \\ &= \boldsymbol{\sigma}_{xm}\mathbf{x} + \boldsymbol{\sigma}_{um}^*\underline{\mathbf{u}} + \boldsymbol{\sigma}_{dm}d_m + \boldsymbol{\sigma}_{cm} \end{aligned} \tag{4.9}$$

where $\boldsymbol{\sigma}_{um}^* = \boldsymbol{\sigma}_{um}\hat{\mathbf{U}}(t)$.

4.2.2 Redefined Periodic Steady State Model

Assuming that piecewise-LTI system is operating around an operating point, let us use small perturbations as

$$\mathbf{x} = \mathbf{X} + \tilde{\mathbf{x}}, \qquad \underline{\mathbf{u}} = \underline{\mathbf{U}} + \underline{\tilde{\mathbf{u}}}, \qquad d_m = D_m + \tilde{d_m}, \qquad m = 1, \cdots, M \tag{4.10}$$

The objective is to seek a first-order approximation to the perturbation of the state at the start of the next switching cycle:

$$\tilde{\mathbf{x}}[k+1] = \mathbf{H}_x \tilde{\mathbf{x}}[k] + \mathbf{H}_u \underline{\tilde{\mathbf{u}}}[k] \tag{4.11}$$

where $\mathbf{H}_x$ is the same monodromy matrix as in equation (2.20) but the control matrix $\mathbf{H}_u$ in equation (2.21) needs modification.

Substituting perturbation equation (4.10) into the redefined Poincaré map (4.8) and switching surfaces (4.9), only leaving the first order approximation to the perturbation of Taylor series, we have:

$$\begin{aligned}
\tilde{\mathbf{x}}[k+1] &= \frac{\partial \hat{\mathbf{f}}}{\partial \mathbf{x}} \tilde{\mathbf{x}}[k] + \frac{\partial \hat{\mathbf{f}}}{\partial d_1} \tilde{d_1}[k] + \cdots + \frac{\partial \hat{\mathbf{f}}}{\partial d_{M-1}} \tilde{d}_{M-1}[k] + \hat{\mathbf{\Theta}}_M \underline{\tilde{\mathbf{u}}}[k] && (4.12)\\
0 &= \frac{\partial \boldsymbol{\sigma}_1}{\partial \mathbf{x}} \tilde{\mathbf{x}}[k] + \frac{\partial \boldsymbol{\sigma}_1}{\partial d_1} \tilde{d_1}[k] + \boldsymbol{\sigma}^*_{u1} \underline{\tilde{\mathbf{u}}}[k] + \boldsymbol{\sigma}_{x1} \hat{\mathbf{\Theta}}_1 \underline{\tilde{\mathbf{u}}}[k] && (4.13)\\
0 &= \frac{\partial \boldsymbol{\sigma}_2}{\partial \mathbf{x}} \tilde{\mathbf{x}}[k] + \frac{\partial \boldsymbol{\sigma}_2}{\partial d_1} \tilde{d_1}[k] + \frac{\partial \boldsymbol{\sigma}_2}{\partial d_2} \tilde{d_2}[k] + \boldsymbol{\sigma}^*_{u2} \underline{\tilde{\mathbf{u}}}[k] + \boldsymbol{\sigma}_{x2} \hat{\mathbf{\Theta}}_2 \underline{\tilde{\mathbf{u}}}[k] \\
&\vdots && (4.14)\\
0 &= \frac{\partial \boldsymbol{\sigma}_{M-1}}{\partial \mathbf{x}} \tilde{\mathbf{x}}[k] + \frac{\partial \boldsymbol{\sigma}_{M-1}}{\partial d_1} \tilde{d_1}[k] + \cdots + \frac{\partial \boldsymbol{\sigma}_{M-1}}{\partial d_{M-1}} \tilde{d}_{M-1}[k] \\
&\quad + \boldsymbol{\sigma}^*_{u\cdot M-1} \underline{\tilde{\mathbf{u}}}[k] + \boldsymbol{\sigma}_{x\cdot M-1} \hat{\mathbf{\Theta}}_{M-1} \underline{\tilde{\mathbf{u}}}[k] && (4.15)
\end{aligned}$$

The objective is to rewrite equation (4.12) into the form in equation (4.11). Consequently, all $\tilde{d_m}[k]$ terms must be represented as functions of $\tilde{\mathbf{x}}[k]$ and $\underline{\tilde{\mathbf{u}}}[k]$. From equation (4.13), $\tilde{d_1}[k]$ can be solved as functions of $\tilde{\mathbf{x}}[k]$ and $\underline{\tilde{\mathbf{u}}}[k]$. Then substituting the result of $\tilde{d_1}[k]$ into equation (4.14), we can derive an expression for $\tilde{d_2}[k]$. If we continue this process until equation (4.15), all $\tilde{d_m}[k]$ terms are represented by $\tilde{\mathbf{x}}[k]$ and $\underline{\tilde{\mathbf{u}}}[k]$. Finally, eliminate $\tilde{d_m}[k]$ in equation (4.12) by substituting their results and thus derive the steady state equation (4.11), where

$$\mathbf{H}_x = \frac{\partial \hat{\mathbf{f}}}{\partial \mathbf{x}} + \sum_{m=1}^{M-1} \sum_{\substack{\alpha_1 > \cdots > \alpha_m \\ \alpha_i = 1, \cdots M-1}} \left[\frac{\frac{\partial \hat{\mathbf{f}}}{\partial d_{\alpha_m}} \prod_{k=1}^{m-1} \left(\frac{\partial \boldsymbol{\sigma}_{\alpha_k}}{\partial d_{\alpha_{k+1}}} \right) \frac{\partial \boldsymbol{\sigma}_{\alpha_m}}{\partial \mathbf{x}}}{(-1)^{m+1} \prod_{k=1}^{m} \left(\frac{\partial \boldsymbol{\sigma}_{\alpha_k}}{\partial d_{\alpha_k}} \right)} \right] \tag{4.16}$$

$$\mathbf{H}_u = \hat{\mathbf{\Theta}}_M(\hat{\mathbf{U}}) + \sum_{m=1}^{M-1} \sum_{\substack{\alpha_1>\cdots>\alpha_m \\ \alpha_i=1,\cdots M-1}} \left[\frac{\frac{\partial \hat{\mathbf{f}}}{\partial d_{\alpha_m}} \prod_{k=1}^{m-1} \left(\frac{\partial \boldsymbol{\sigma}_{\alpha_k}}{\partial d_{\alpha_{k+1}}} \right) [\boldsymbol{\sigma}^*_{u\alpha_m} + \boldsymbol{\sigma}_{x\alpha_m} \hat{\mathbf{\Theta}}_{\alpha_m}(\hat{\mathbf{U}})]}{(-1)^{m+1} \prod_{k=1}^{m} \left(\frac{\partial \boldsymbol{\sigma}_{\alpha_k}}{\partial d_{\alpha_k}} \right)} \right] \tag{4.17}$$

The derivative terms in equation (4.16) and (4.17) are expressed as follows:

$$\begin{aligned}
\frac{\partial \hat{\mathbf{f}}}{\partial \mathbf{x}} &= \mathbf{\Pi}_1^M \\
\frac{\partial \boldsymbol{\sigma}_\alpha}{\partial \mathbf{x}} &= \boldsymbol{\sigma}_{x\alpha} \mathbf{\Pi}_1^\alpha \\
\hat{\mathbf{\Theta}}_q(\hat{\mathbf{U}}) &= \sum_{i=1}^{q} \mathbf{\Pi}_{i+1}^q \hat{\mathbf{\Psi}}_i(\hat{\mathbf{U}}) \\
\frac{\partial \hat{\mathbf{f}}}{\partial d_\alpha} &= \mathbf{\Pi}_{\alpha+1}^M \left[\mathbf{R}_\alpha \dot{\mathbf{X}}(d_\alpha^-) - \dot{\mathbf{X}}(d_\alpha^+) \right] \\
\frac{\partial \boldsymbol{\sigma}_\beta}{\partial d_\alpha} &= \begin{cases} \boldsymbol{\sigma}_{x\beta} \mathbf{\Pi}_{\alpha+1}^\beta \left[\mathbf{R}_\alpha \dot{\mathbf{X}}(d_\alpha^-) - \dot{\mathbf{X}}(d_\alpha^+) \right] & \beta > \alpha \\ \boldsymbol{\sigma}_{x\alpha} \dot{\mathbf{X}}(d_\alpha^-) + \dot{\boldsymbol{\sigma}}^*_{u\alpha} \underline{\mathbf{u}} + \boldsymbol{\sigma}_{d\alpha} & \beta = \alpha \\ \mathbf{0} & \beta < \alpha \end{cases}
\end{aligned}$$

where

$$\begin{aligned}
\dot{\mathbf{X}}(d_\alpha^-) &= \mathbf{A}_\alpha \mathbf{X}_\alpha + \mathbf{B}_\alpha \mathbf{U} \\
\dot{\mathbf{X}}(d_\alpha^+) &= \mathbf{A}_{\alpha+1} \mathbf{R}_\alpha \mathbf{X}_\alpha + \mathbf{B}_{\alpha+1} \mathbf{U} \\
\mathbf{\Pi}_p^q &= \prod_{i=p}^{q} \mathbf{\Phi}_i(\Delta_i) \mathbf{R}_i \quad p \le q \\
\hat{\mathbf{\Psi}}_i(\hat{\mathbf{U}}) &= \int_{t_0}^{t} \mathbf{\Phi}_i(t,\tau) \mathbf{B}_i \hat{\mathbf{U}}(t-\tau) d\tau \\
\mathbf{\Phi}_i(\Delta_i) &= e^{\mathbf{A}_i(\Delta_i)} \\
\Delta_i &= d_i - d_{i-1} \quad i \in \{1, 2, \cdots, M\}
\end{aligned}$$

Here the inner summations are taken over all of the possible combinations of m different integer numbers $\alpha_k \in \{M-1, M-2, \cdots, 1\} \quad k = 1, 2, \cdots, m$ with $\alpha_1 = M$ such that $\alpha_1 > \cdots > \alpha_m$. Equations (4.16) and (4.17) provide the closed-form expressions for the monodromy matrix $\mathbf{H}_x$ and the control matrix $\mathbf{H}_u$, if

the input signal $\mathbf{u}(t)$ can be rewritten as $\mathbf{u}(t) = \hat{\mathbf{U}}(t)\underline{\mathbf{u}}$, where $\hat{\mathbf{U}}(t)$ is the time-varying part and $\underline{\mathbf{u}}$ is the constant part. Then the SSSM of power converter system is converted to the periodic steady state model as equation (4.11) which can be used for analyzing properties such as stability, periodic steady state response, and frequency response.

4.2.3 Closed-Form Expressions for Zero-State Response to Bohl-type Inputs

To determine the switching sequence and monodromy matrix as described in the previous section, it is necessary to solve the state equation. The solution is often expressed as:

$$\mathbf{x}(t) = \mathbf{\Phi}(t, t_0)\mathbf{x}_0 + \int_{t_0}^{t} \mathbf{\Phi}(t, \tau)\mathbf{B}\mathbf{u}(\tau)d\tau \tag{4.18}$$

where

$$\begin{aligned} \mathbf{\Phi}(t, t_0) &= e^{\mathbf{A}(t-t_0)} \\ \mathbf{x}_0 &= \mathbf{x}(t_0) \end{aligned}$$

While the zero-state response represented by the integral in the second term on the right hand side of equation (4.18) can be readily approximated numerically, it can be expressed in closed-form for so-called Bohl-type inputs [114]. For the implementation of the enhanced Floquet method in MATLAB, it is desirable to represent the zero-state response as a linear combination of real-valued functions of time.

Real-Valued Modal Decomposition

Before considering the state-transition matrix $\mathbf{\Phi}(t, t_0)$ in equation (4.18), it is useful to consider the matrix exponential: $e^{\mathbf{A}}$. Once all eigenvalues and eigenvectors have been determined, $\mathbf{A}$ can be expressed as $\mathbf{A} = \mathbf{P}\mathbf{\Lambda}\mathbf{P}^{-1}$, where $\mathbf{P}$ consists of all eigenvectors and $\mathbf{\Lambda}$ is a diagonal matrix with all eigenvalues. Thus, the matrix

exponential of $\mathbf{A}$ can be expressed:

$$e^{\mathbf{A}} = \left[\begin{array}{cccc} \mathbf{p}_1 & \mathbf{p}_2 & \cdots & \mathbf{p}_N \end{array} \right] \left[\begin{array}{cccc} e^{\lambda_1} & 0 & \cdots & 0 \\ 0 & e^{\lambda_2} & \cdots & 0 \\ \vdots & \vdots & \ddots & \vdots \\ 0 & 0 & \cdots & e^{\lambda_N} \end{array} \right] \left[\begin{array}{cccc} \mathbf{p}_1 & \mathbf{p}_2 & \cdots & \mathbf{p}_N \end{array} \right]^{-1}$$

This derivation is under assumption that each of the eigenvalues is distinct, which is usually true in power converter systems. If an eigenvalue is complex, then one of the other eigenvalues is its complex conjugate and the eigenvectors associated with the pair of complex conjugate eigenvalues are complex conjugates. An entirely real representation $\mathbf{A} = \mathbf{P}\mathbf{\Lambda}\mathbf{P}^{-1}$ is possible but $\mathbf{\Lambda}$ will be block diagonal instead of simply diagonal. To illustrate the transformation from a complex, simply diagonal representation to a real-valued, block-diagonal representation, let us consider an $\mathbf{A} = \mathbf{P}\mathbf{\Lambda}\mathbf{P}^{-1}$ matrix that is 2×2; the technique can be applied to any appropriate 2×2 diagonal block of a larger matrix. Suppose the two eigenvalues of $\mathbf{A}$ are complex, then we have $\lambda_1 = \alpha_1 + j\omega_1 = \lambda_2^*$ and $\mathbf{p}_1 = \mathbf{p}_2^*$. Thus, we have

$$\begin{aligned} \mathbf{A} &= \left[\begin{array}{cc} \mathbf{p}_1 & \mathbf{p}_1^* \end{array} \right] \left[\begin{array}{cc} \lambda_1 & 0 \\ 0 & \lambda_1^* \end{array} \right] \left[\begin{array}{cc} \mathbf{p}_1 & \mathbf{p}_1^* \end{array} \right]^{-1} \\ &= \left[\begin{array}{cc} \mathbf{p}_1 & \mathbf{p}_1^* \end{array} \right] \mathbf{T}\mathbf{T}^{-1} \left[\begin{array}{cc} \lambda_1 & 0 \\ 0 & \lambda_1^* \end{array} \right] \mathbf{T}\mathbf{T}^{-1} \left[\begin{array}{cc} \mathbf{p}_1 & \mathbf{p}_1^* \end{array} \right]^{-1} \\ &= (\left[\begin{array}{cc} \mathbf{p}_1 & \mathbf{p}_1^* \end{array} \right] \mathbf{T})\mathbf{T}^{-1} \left[\begin{array}{cc} \lambda_1 & 0 \\ 0 & \lambda_1^* \end{array} \right] \mathbf{T}(\left[\begin{array}{cc} \mathbf{p}_1 & \mathbf{p}_1^* \end{array} \right] \mathbf{T})^{-1}. \\ &= (\mathbf{P}\mathbf{T})\mathbf{T}^{-1}\mathbf{\Lambda}\mathbf{T}(\mathbf{P}\mathbf{T})^{-1} \end{aligned}$$

By choosing $\mathbf{T} = \frac{1}{2} \left[\begin{array}{cc} 1 & -j \\ 1 & j \end{array} \right]$, the state-transition matrix $\mathbf{\Phi}(t, t_0)$ in equation (4.18) can be expressed as a real-valued function.

$$\begin{aligned} \mathbf{\Phi}(t, t_0) &= e^{\mathbf{A}(t-t_0)} \\ &= e^{(\mathbf{P}\mathbf{T})\mathbf{T}^{-1}\mathbf{\Lambda}\mathbf{T}(\mathbf{P}\mathbf{T})^{-1}(t-t_0)} \\ &= (\mathbf{P}\mathbf{T})e^{\mathbf{T}^{-1}\mathbf{\Lambda}\mathbf{T}(t-t_0)}(\mathbf{P}\mathbf{T})^{-1} \end{aligned}$$

$$= \begin{bmatrix} \mathrm{Re}(\mathbf{p}_1) & \mathrm{Im}(\mathbf{p}_1) \end{bmatrix} e^{\alpha_1(t-t_0)} \begin{bmatrix} \cos(\omega_1(t-t_0)) & \sin(\omega_1(t-t_0)) \\ -\sin(\omega_1(t-t_0)) & \cos(\omega_1(t-t_0)) \end{bmatrix} \begin{bmatrix} \mathrm{Re}(\mathbf{p}_1) & \mathrm{Im}(\mathbf{p}_1) \end{bmatrix}^{-1} \quad (4.19)$$

Therefore, we can partition $\mathbf{\Phi}(t, t_0)$ using K blocks, each of which corresponds to either a real eigenvalue or to a pair of complex conjugate eigenvalues. The state-transition matrix $\mathbf{\Phi}(t, t_0)$ can be represented by real-valued matrices.

$$\mathbf{\Phi}(t,t_0) = \begin{bmatrix} \mathbf{q}_1 & \mathbf{q}_2 & \cdots & \mathbf{q}_K \end{bmatrix} \begin{bmatrix} e^{\Lambda_1}(t-t_0) & 0 & \cdots & 0 \\ 0 & e^{\Lambda_2}(t-t_0) & \cdots & 0 \\ \vdots & \vdots & \ddots & \vdots \\ 0 & 0 & \cdots & e^{\Lambda_K}(t-t_0) \end{bmatrix} \begin{bmatrix} \mathbf{q}_1 & \mathbf{q}_2 & \cdots & \mathbf{q}_K \end{bmatrix}^{-1}$$

Replacing $\mathbf{Q}^{-1}$ by $\mathbf{R}$:

$$\begin{aligned} \mathbf{\Phi}(t,t_0) &= \begin{bmatrix} \mathbf{q}_1 & \mathbf{q}_2 & \cdots & \mathbf{q}_K \end{bmatrix} \begin{bmatrix} e^{\Lambda_1}(t-t_0) & 0 & \cdots & 0 \\ 0 & e^{\Lambda_2}(t-t_0) & \cdots & 0 \\ \vdots & \vdots & \ddots & \vdots \\ 0 & 0 & \cdots & e^{\Lambda_K}(t-t_0) \end{bmatrix} \begin{bmatrix} \mathbf{r}_1 \\ \mathbf{r}_2 \\ \vdots \\ \mathbf{r}_K \end{bmatrix} \\ &= \mathbf{q}_1 e^{\Lambda_1(t-t_0)}\mathbf{r}_1 + \mathbf{q}_2 e^{\Lambda_2(t-t_0)}\mathbf{r}_2 + \cdots + \mathbf{q}_K e^{\Lambda_K(t-t_0)}\mathbf{r}_K \end{aligned} \quad (4.20)$$

where for a real eigenvalue, the mode is expressed as:

$$\begin{aligned} \mathbf{q}_k e^{\Lambda_k(t-t_0)}\mathbf{r}_k &= e^{\lambda_k(t-t_0)}\mathbf{q}_k\mathbf{r}_k \\ &= e^{\lambda_k(t-t_0)}\mathbf{M}_k \end{aligned}$$

and for a complex conjugate pair of eigenvalues, the mode is expressed as:

$$\begin{aligned} \mathbf{q}_k e^{\Lambda_k(t-t_0)}\mathbf{r}_k &= e^{\alpha_k(t-t_0)}(\cos(\omega_k(t-t_0))\mathbf{q}_k\mathbf{r}_k - \sin(\omega_k(t-t_0))\mathbf{q}_k\mathbf{J}\mathbf{r}_k \\ &= e^{\alpha_k(t-t_0)}(\cos(\omega_k(t-t_0))\mathbf{M}_{ck} - \sin(\omega_k(t-t_0))\mathbf{M}_{sk} \end{aligned} \quad (4.21)$$

where $\mathbf{J} = \begin{bmatrix} 0 & -1 \\ 1 & 0 \end{bmatrix}$. The derivations of equations (4.19) and (4.21) are provided in Appendix A.

Zero-State Response

Suppose the time-varying input signal can be represented as $\mathbf{u}(t) = \hat{\mathbf{u}}(t) \cdot \underline{\mathbf{u}}$, where $\hat{\mathbf{u}}(t)$ contains time varying parts, $\underline{\mathbf{u}}$ contains constant parts, and $\cdot$ indicates the Hadamard product. That is:

$$\mathbf{u}(t) = \begin{bmatrix} \hat{u}_1(t)\underline{u}_1 \\ \vdots \\ \hat{u}_P(t)\underline{u}_P \end{bmatrix} = \begin{bmatrix} \hat{u}_1(t) \\ \vdots \\ \hat{u}_P(t) \end{bmatrix} \cdot \begin{bmatrix} \underline{u}_1 \\ \vdots \\ \underline{u}_P \end{bmatrix}$$

This Hadamard product is equivalent to the normal matrix product $\mathbf{u}(t) = \hat{\mathbf{U}}(t)\underline{\mathbf{u}}$, where $\hat{\mathbf{U}}(t)$ is a diagonal matrix with time-varying inputs placing along the diagonal entries. That is:

$$\mathbf{u}(t) = \begin{bmatrix} \hat{u}_1(t)\underline{u}_1 \\ \vdots \\ \hat{u}_P(t)\underline{u}_P \end{bmatrix} = \begin{bmatrix} \hat{u}_1(t) & 0 & 0 \\ 0 & \ddots & 0 \\ 0 & 0 & \hat{u}_P(t) \end{bmatrix} \begin{bmatrix} \underline{u}_1 \\ \vdots \\ \underline{u}_P \end{bmatrix}$$

After the real-valued modal decomposition of the state-transition matrix $\mathbf{\Phi}(t, t_0)$, one can derive closed-form expressions for the zero-state response to various input signals.

$$\begin{aligned} \mathbf{\Psi}(t, t_0) &= \int_{t_0}^{t} \mathbf{\Phi}(t, \tau)\mathbf{B}\mathbf{u}(\tau)d\tau \\ &= \int_{t_0}^{t} \mathbf{\Phi}(t, \tau) \begin{bmatrix} \mathbf{b}_1 & \cdots & \mathbf{b}_P \end{bmatrix} \begin{bmatrix} u_1(\tau) \\ \vdots \\ u_P(\tau) \end{bmatrix} d\tau \\ &= \sum_{p=1}^{P} \int_{t_0}^{t} \mathbf{\Phi}(t, \tau)\mathbf{b}_p \hat{u}_p(\tau)\underline{u}_p d\tau \\ &= \sum_{p=1}^{P} \int_{t_0}^{t} \mathbf{\Phi}(t, \tau)\mathbf{b}_p \hat{u}_p(\tau)d\tau \underline{u}_p \\ &= \sum_{p=1}^{P} \psi_p(t, t_0)\underline{u}_p \end{aligned} \tag{4.22}$$

Thus, the zero-state response can be obtained by summing the zero-state responses for the P input signals where the zero-state response to input p is $\psi_p(t,t_0)\underline{u}_p = \int_{t_0}^{t} \mathbf{\Phi}(t,\tau)\mathbf{b}_p\hat{u}_p(\tau)d\tau\underline{u}_p$ of each input signal $\hat{u}_p(t)$, where $\hat{u}_p(t)$ can be either constant or sinusoidal. The state-transition matrix $\mathbf{\Phi}(t,t_0)$ is expressed by real-valued decomposition described by equation (4.20). So there are four cases of interest for equation (4.22): zero-state response of a real eigenvalue to a constant input, zero-state response of a complex eigenvalue to a constant input, zero-state response of a real eigenvalue to a sinusoidal input, and zero-state response of a complex eigenvalue to a sinusoidal input. The closed-form expressions for these cases are provided in Appendix A as equation (A.1), equation (A.2), equation (A.3), and equation (A.4), respectively.

4.3 Results

In this section, the enhanced Floquet method is applied to a buck converter with current-mode control as shown in Figure 4.3. The disturbance is modeled as sinusoidal signal added to V_o^{ref}. This represents the practically important case of the feedback signal being corrupted by switching frequency noise. The results are compared to those obtained by using Ridley's model [1]. Results from a commercial circuit simulator results are also presented.

The piecewise-LTI model of the buck converter system is described by equation (4.4). Matrices $\mathbf{A}_m$, $\mathbf{B}_m$ are the same as those in equation (2.24). The parameter values of the particular buck converter are provided in Table B.1 of Appendix B. Assume that a sinusoidal noise disturbance signal is added to the output voltage reference signal as shown in Figure 4.3; $v_o^{ref} = V_o^{ref} + \tilde{v}_o^{ref}(t) = V_o^{ref} + \underline{v}_o^{ref}\cos(w_s t)$, where $\underline{v}_o^{ref}$ is the magnitude of the disturbance and is chosen to be 0.1% of V_o^{ref}. The input vector is now defined as:

$$\begin{aligned}
\mathbf{u}(t) &= \begin{bmatrix} V_d \\ V_o^{ref} + \tilde{v}_o^{ref}(t) \end{bmatrix} \\
&= \begin{bmatrix} 1 & 0 & 0 \\ 0 & 1 & 1 \end{bmatrix} \begin{bmatrix} V_d \\ V_o^{ref} \\ \underline{v}_o^{ref}\cos(w_s t) \end{bmatrix}
\end{aligned}$$

$$
\begin{aligned}
&= \begin{bmatrix} 1 & 0 & 0 \\ 0 & 1 & 1 \end{bmatrix} \begin{bmatrix} 1 & 0 & 0 \\ 0 & 1 & 0 \\ 0 & 0 & \cos(w_s t) \end{bmatrix} \begin{bmatrix} V_d \\ V_o^{ref} \\ \underline{v}_o^{ref} \end{bmatrix} \\
&= \mathbf{T}_u \hat{\mathbf{U}}(t) \underline{\mathbf{u}}
\end{aligned}
$$

where $\hat{\mathbf{U}}(t)$ is the time-varying part and $\underline{\mathbf{u}}$ is the constant part. The switching surfaces in (4.9), vector $\boldsymbol{\sigma}_{um}^* = \boldsymbol{\sigma}_{um}\mathbf{T}_u\hat{\mathbf{U}}(t)$, while $\boldsymbol{\sigma}_{xm}$, $\boldsymbol{\sigma}_{dm}$, and $\boldsymbol{\sigma}_{cm}$ remain the same as those in equation (2.27). The transformation matrix $\mathbf{T}_u$ also post-multiplies the SSSM control matrices $\mathbf{B}_m$ and $\mathbf{D}_m$ such that $\mathbf{B}_m^* = \mathbf{B}_m\mathbf{T}_u$ and $\mathbf{D}_m^* = \mathbf{D}_m\mathbf{T}_u$.

4.3.1 Frequency Response

By investigating the Floquet multipliers or eigenvalues of $\mathbf{H}_x$, we can assess stability and examine bifurcation properties of the buck converter system with switching frequency disturbance. As shown in Figure 4.4, all Floquet multipliers are located in the unit circle indicating that the system is stable. This can be confirmed from the periodic steady state response shown in Figure 4.5 as well.

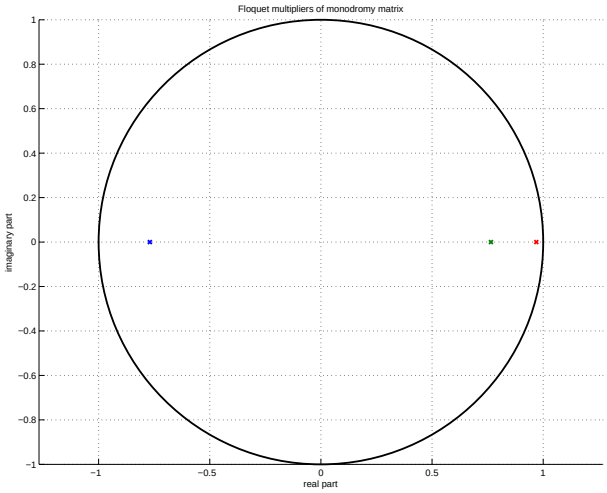

Figure 4.4. Buck converter system Floquet multipliers (eigenvalues of monodromy matrix).

The accuracy of the Floquet method is verified by circuit simulations which

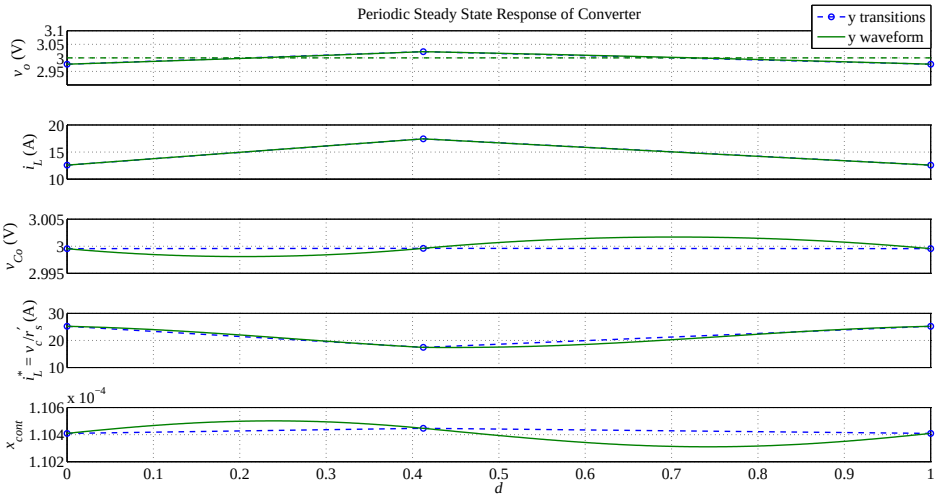

Figure 4.5. Periodic steady state response of the buck converter.

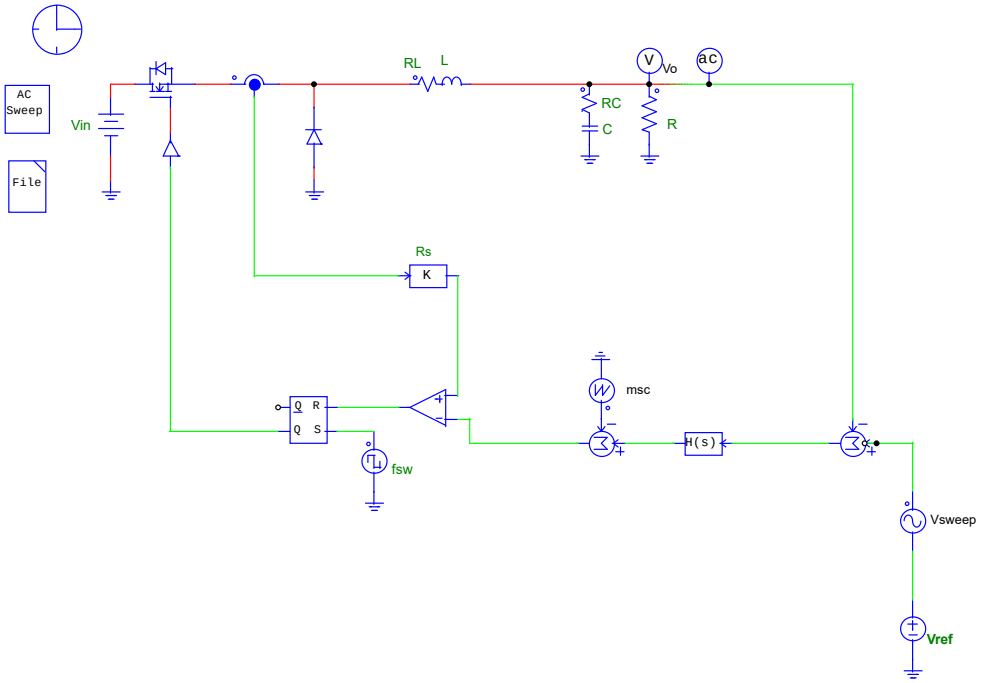

Figure 4.6. PSIM schematic circuit diagram of the buck converter system.

are obtained by PSIM commercial software. The PSIM schematic of the circuit is shown in Figure 4.6. The frequency response from v_o^{ref} to v_o is shown in Figure 4.7; it includes 5000 samples. Frequency responses obtained from the Floquet method, Ridley's model, and PSIM simulation are shown in Figure 4.8. For the

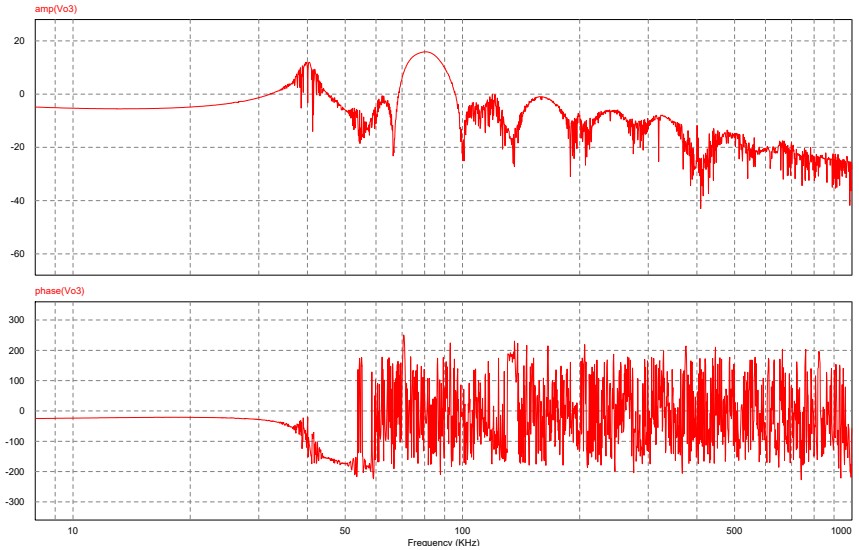

Figure 4.7. Input voltage to output voltage frequency response of the buck converter system calculating using a commercial circuit simulation software.

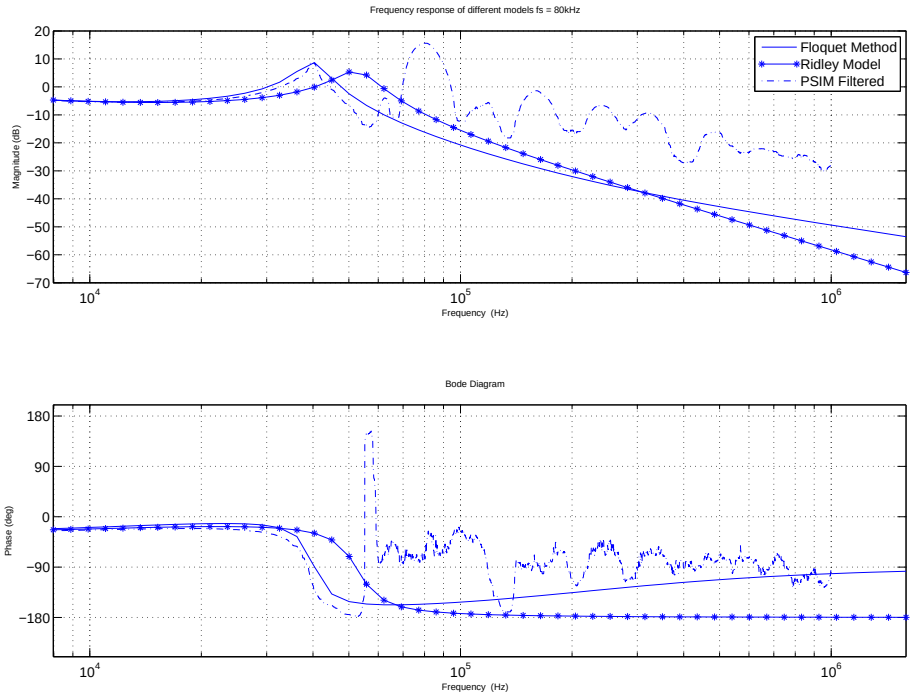

Figure 4.8. Comparison of input voltage to output voltage frequency responses of the buck converter system using different approaches.

Floquet method, the frequency response is calculated by converting the discrete-time Poincaré map $(\mathbf{H}_x, \mathbf{H}_u, \mathbf{C}, \mathbf{D})$ to a continuous-time transfer function using a zero-order-hold (MATLAB d2c.m function). For the PSIM results, the frequency response in Figure 4.7 was decluttered using a median filter with a window width of 100. In the low frequency range, all three responses are in good agreement. In the high frequency range, the response from the Floquet method and Ridley's model are comparable, although the former exhibits the effect of a zero in the transfer function. The response from PSIM is markedly different because the simulation includes the periodic switching that manifests itself through complex poles at the switching frequency and its harmonics. The very high frequency phase response from PSIM oscillates around $-90°$. The response from the Floquet method characterizes this trend better than Ridley's model. In the mid-frequency range defined here as $\frac{1}{2}f_s$ to f_s where $f_s = 80$ kHz, comparison of the responses is more complicated. Around $\frac{1}{2}f_s$, there is good agreement between the Floquet method and PSIM simulation. Both indicate a well damped complex pole at $f = \frac{1}{2}f_s = 40$ kHz with a damping factor of $\xi = 0.08$, a magnitude peak of 8 dB, and $-180°$ phase shift within a band of approximately 20 kHz. Ridley's model, on the other hand, indicates a complex pole at $f = 55$ kHz with a greater damping factor of $\xi = 0.12$.

As we compare Figure 4.7 and Figure 4.8, the results provided by the Floquet method are more accurate and have better consistency to the commercial circuit simulation results. Frequency characteristics of small signal model are essentially meaningless at half switching frequency and above. The Floquet method provides periodic steady state analysis in a quick manner. In high-frequency region, the frequency response is usually difficult to predict. The commercial circuit simulation results confirm good accuracy of the Floquet method.

4.3.2 Exact Frequency Response at Harmonics and Sub-harmonics

In the previous section, the frequency of the sinusoidal input was set to the switching frequency of the converter in order to study the affect of noise in the feedback path of these systems when the converter is connected to a stiff supply (i.e., a sup-

ply for which voltage varies with load current in only a small, linear manner). In multi-converter systems, the source network may not be stiff, because each of the converters has an impedance that can change radically as the frequency of the load is varied. The potential for this is evident from Figure 4.9 which shows the input admittance of the buck converter system. The enhanced Floquet method can be used to determine the exact frequency response at discrete frequencies corresponding to harmonics and sub-harmonics of the switching period. More specifically, the sinusoidal input can be set to a frequency $f_d = \frac{n}{m} f_s$ where n and m are integer values.

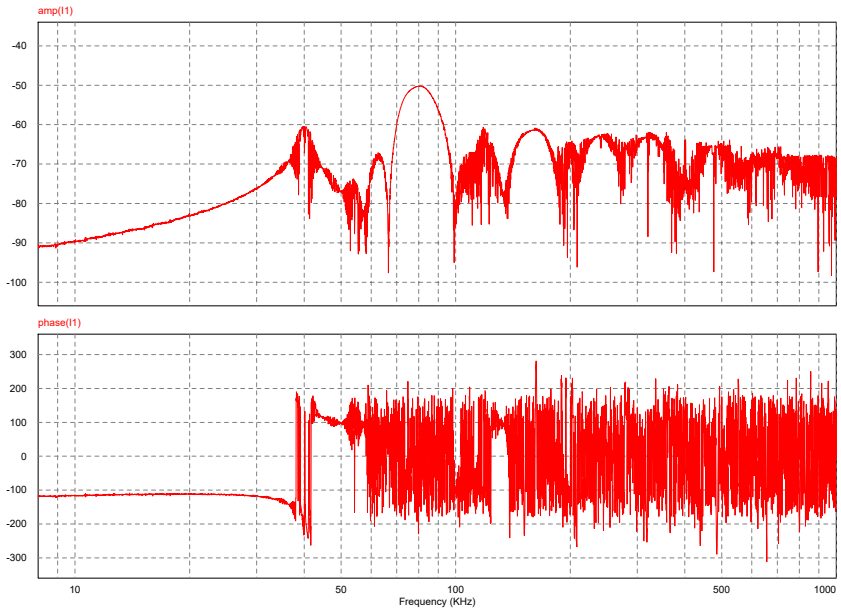

Figure 4.9. Input admittance of the buck converter system calculating using a commercial circuit simulation software.

To calculate the exact frequency response from input voltage to output voltage at harmonics and sub-harmonics, perturb output reference signal by a sinusoidal signal and apply multi-period solver and the enhanced Floquet method to obtain periodic steady state responses that include harmonics and sub-harmonics. Then use Fourier series analysis to obtain the magnitudes and phases of corresponding responses. Finally, calculate the magnitude ratio and phase difference between the output signal and reference output signal.

Figure 4.10 compares frequency responses from input voltage to output voltage

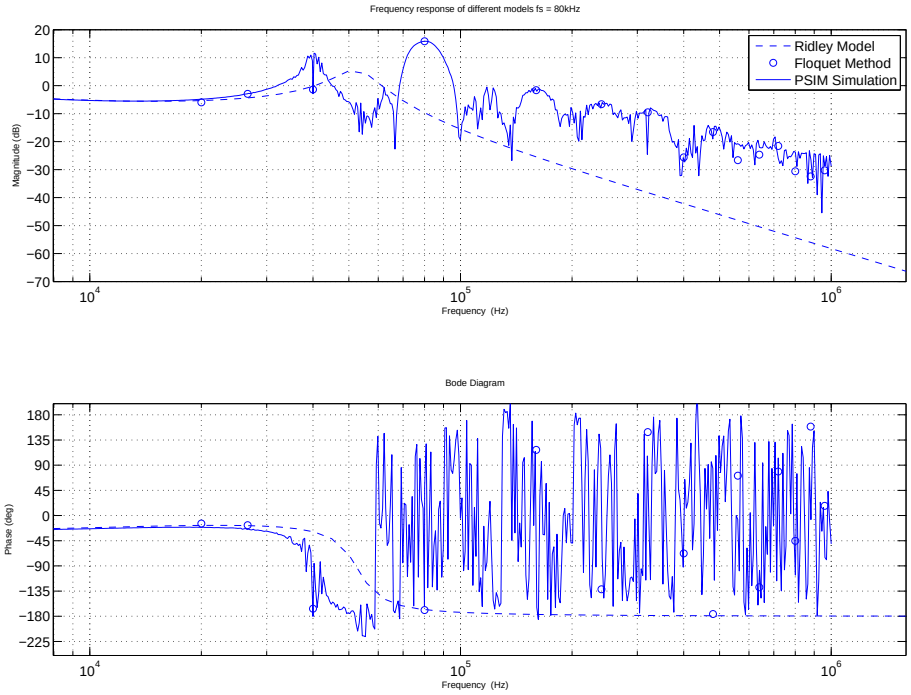

Figure 4.10. Comparison of exact input voltage to output voltage frequency responses using different approaches.

obtained from the Floquet method, Ridley's model, and PSIM simulation. Dashed line represents response from Ridley's model. Solid line shows the response from PSIM simulation. Circles are frequency responses at harmonic and sub-harmonic frequencies. As shown in this figure, multi-period solver combined with the enhanced Floquet method provides a very good estimation of magnitude ratio and phase shift than Ridley's model. Ridley's model only gives information up to half switching frequency. The Floquet method can provide accurate frequency response not only below half switching frequency but also half switching frequency and higher harmonic frequencies.

4.4 Summary

In this chapter, enhancements to the existing Floquet method have been presented. A multi-period solver permits capture of low frequency sub-harmonic behavior

given a standard (1-period) switch state space model. Admission of sinusoidal input signals is achieved through modification of the switching condition inequality and derivation of control matrix $\mathbf{H}_u$. Solver efficiency is also improved through the derivation of closed-form expressions for the zero-state response to sinusoidal inputs.

A buck converter under current-mode control with switching frequency disturbance is used as an example to demonstrate the enhanced Floquet method. The stability and periodic steady state response can be studied by investigating Floquet multipliers of the Poincaré map monodromy matrix. The frequency response from input voltage to output voltage is calculated and compared with Ridley's model and PSIM simulation. These results match well in the low-frequency range but differ in the high-frequency range. By combining multi-period solver and the enhanced Floquet method, exact frequency responses at harmonic and sub-harmonic frequencies are obtained. The accuracy of the results by the enhanced Floquet method is verified by PSIM commercial circuit simulation and proved that the enhanced Floquet method is a fast and reliable way to analyze switch-mode power converter systems.

Chapter 5

Optimal Design of Power Converter Systems

Five important criteria for power converter system design are: power quality, efficiency, size, cost, and reliability. Given a set of design specifications, one must select components values for inductors and capacitors in the power stage and input filter as well as for the compensator. In this chapter, an automated design approach is described and compared to a conventional design process.

5.1 Power Converter System Design Considerations

Typically, there are two or three subsystems within a power converter system: power stage, compensator, and input filter. The input filter is optional depending upon the nature of the source network. It is increasingly important, however, as systems of converter systems become more common. In such systems of systems, the role of input filter is to improve the power quality at the input to power converter systems. The performance degradation due to the source transients can be avoided. Insertion of an input filter complicates the dynamics of an individual converter. A poorly designed input filter may even make the system unstable. Recently, there are many efforts to improve the stability and dynamics of power converter systems with input filter. The following design considerations must

be taken into account. The buck converter system with current-mode control is presented to illustrate the design considerations.

5.1.1 Power Stage Design

The simplest and most common power stage topology is the buck converter, sometimes referred as step-down converter. The input current for a buck converter is discontinuous or pulsating due to the controlled switch being connected to the input port. The output current is continuous assuming the converter is operating in CCM, because the output inductor is between the switching elements and the output capacitor. The first task is to choose inductance and capacitance values for inductor L and capacitor C_o based on desired requirements including steady state performance, transient response, and efficiency.

Inductance Calculation

In practical design of dc-to-dc power converters, the power stage is designed with regard to continuous conduction mode (CCM) or discontinuous conduction mode (DCM). Generally, DCM is undesirable for high-frequency power converters, because the peak inductor energy and the peak current stresses on semiconductor devices are much higher than in CCM. Thus, CCM is usually selected as the starting point for power stage design. In most feedback control applications, the output voltage V_o is regulated to be constant by controlling the duty cycle D to compensate for variations in the input voltage $V_d \in [V_{d_{min}}, V_{d_{max}}]$. To select an appropriate value for L, a minimum value of output current $I_{o_{min}}$ and the entire interval $D \in [D_{min}, D_{max}]$ must be known. The minimum feasible value for L of a buck converter is calculated as:

$$L \geqslant \frac{1}{2}\frac{V_o}{f_s I_{o_{min}}}(1 - D_{min}).$$

where f_s is the switching frequency, and V_o is the output voltage. Since $D_{min} = \frac{V_o}{V_{d_{max}}}$, the inequality for selecting inductance can also be expressed as:

$$L \geqslant \frac{V_o(V_{d_{max}} - V_o)}{2 f_s V_{d_{max}} I_{o_{min}}}. \tag{5.1}$$

Inductor Core Selection and Turns Calculation

The inductor is an energy storage component where energy is stored in a magnetic field. It consists of an insulated conductor wound on a high-permeability material core made of ferrite. The shape of the core is a factor to be considered. Toroidal cores are the most common. The objective is to design an inductor by selecting a toroidal core and then determining number of turn required to obtained a given inductance L while avoiding magnetic saturation for the worst-case current I_{max}. The manufacturer provides figures relating the different cores and LI_{max}^2 values they can handle without saturation, from which the selection of core can be made. So the selection of the core requires knowing LI_{max}^2. Once the number of turns has been determined the associated parasitic resistance r_L can be calculated.

The inductance of a ferrite toroidal inductor can be expressed as:

$$L = 10^{-9} A_L N^2 \tag{5.2}$$

where L is the desired inductance, N is the number of turns of wire, and A_L is the inductance factor which represents the ability of core to provide inductance; the unit of A_L is nH/turn^2. Then using equation (5.2), number of turns can be determined for a given inductance L.

The wires are wounded along the toroidal core. Each turn of wire passes through the window area of the core. The fill factor represents how much the window area of core is filled by the winding. The fill factor K_f is defined as follows:

$$K_f = \frac{N A_w}{W} \tag{5.3}$$

where A_w is the wire cross-sectional area and W is the core window area given by core manufactures. NASA provided an approximation of the maximum practical winding factor to be 0.4 ($K_f = 0.4$) [115]. So combining equation (5.2) and (5.3) by eliminating N, one requirement for core selection given a desired inductance L is derived:

$$L \leq \frac{K_f^2 W^2 A_L}{10^{-9} A_w^2}. \tag{5.4}$$

The right hand side of this inequality contains parameters dependent on the choice of different toroidal cores and wires.

For a candidate toroidal core that satisfies inequality (5.4), the number of turns of wire can be determined by equation (5.2) given a specific inductance L. Then the associated dc resistant of the inductor can be calculated:

$$r_L = N l_{p.t.} r_{p.u.} \tag{5.5}$$

where $l_{p.t.}$ is the length per turn, $r_{p.u.}$ is the resistance per unit length of the wire.

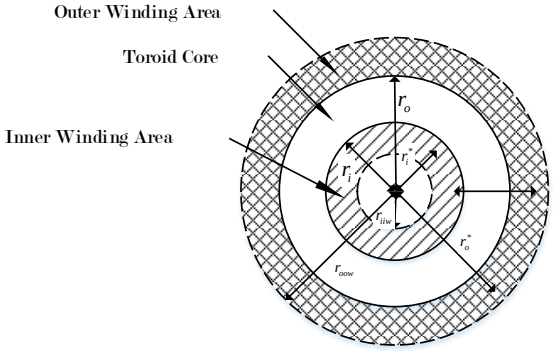

Figure 5.1. Winding of toroid core.

Figure 5.1 shows a cross section of a toroid core (white) and a winding (cross hatch), where r_i is the inner radius, r_o is the outer radius, r_{iiw} is the smallest inner winding radius, r_{oow} is the largest outer winding radius, r_i^* is the mean inner winding radius, and r_o^* is the mean outer winding radius. Assuming the full fill winding approach is used, the maximum practical fill factor is $K_f = 0.4$. Given N, A_w, r_i, and r_o are specified in previous steps, a good approximation of the length per turn $l_{p.t.}$ for a winding on a toroid core can be calculated.

For the inner winding annular region, by the definition of fill factor, we have:

$$\frac{NA_w}{K_f} = \pi(r_i^2 - r_{iiw}^2)$$

One can solve this equation to obtain the smallest inner winding radius r_{iiw}. The mean inner winding radius r_i^* is defined such that the annular area from r_{iiw} to r_i^* equals to that from r_i^* to r_i.

$$\pi({r_i^*}^2 - r_{iiw}^2) = \pi(r_i^2 - {r_i^*}^2)$$

So the mean inner winding radius r_i^* is calculated as:

$$r_i^* = \sqrt{\frac{1}{2}(r_i^2 + r_{iiw}^2)}$$

Similarly, for the outer winding annular region, the largest outer winding radius r_{oow} can be determined by solving this equation:

$$\frac{NA_w}{K_f} = \pi(r_{oow}^2 - r_o^2)$$

The mean outer winding radius r_o^* is defined such that the annular area from r_o to r_o^* equals to that from r_o^* to r_{oow}.

$$\pi(r_o^{*^2} - r_o^2) = \pi(r_{oow}^2 - r_o^{*^2})$$

So the mean outer winding radius r_o^* is calculated as:

$$r_o^* = \sqrt{\frac{1}{2}(r_o^2 + r_{oow}^2)}$$

Thus the length per turn $l_{p.t.}$ is calculated as:

$$\begin{aligned} l_{p.t.} &= 2(h + r_i - r_i^* + r_o - r_i + r_o^* - r_o) \\ &= 2(h - r_i^* + r_o^*) \end{aligned} \tag{5.6}$$

where h is the height of the core. Here, we are ignoring the effect of wire lapping above and below the core. By substituting equation (5.6) into equation (5.5), the associated dc resistant r_L can be calculated and used when calculating the power loss of the inductor.

For a selected inductor core, core losses per unit volume (P_m in mW/cm^3) represents the energy dissipated within the unit volume of the inductor core. They are plotted as a function of maximum excursion of the flux density for various values of frequency, which are provided by the core manufacturer.

Capacitance Calculation

The specification on voltage ripple is often provided in percent of the output voltage as $\frac{\Delta V_o}{V_o}$, where ΔV_o is the peak-to-peak voltage ripple. To maintain output power quality, the inequality for selecting capacitance for a buck converter is given by:

$$\begin{aligned} C_o &\geqslant \frac{1}{8 f_s^2 L \frac{\Delta V_o}{V_o}} (1 - D_{min}) \\ &= \frac{1}{8 f_s^2 L \frac{\Delta V_o}{V_o}} (1 - \frac{V_o}{V_{d_{max}}}) \end{aligned} \tag{5.7}$$

Capacitor Selection

Capacitors are used to maintain voltage by absorbing and supplying current in response to the instantaneous energy demand at the user's end. The choice of capacitor must have a voltage rating that is greater than the maximum voltage plus a margin. Given a capacitance C_o, the volume of the capacitor can be determined from data sheets provided by capacitor manufacturers. Capacitors with different capacitance usually have different dimensions. This also makes the selection of capacitors a discrete problem.

Once the capacitor is selected, the associated equivalent series resistance (ESR) can be calculated using the following expression.

$$r_c = \frac{df}{2\pi f_s C} \tag{5.8}$$

where f_s is switching frequency and df is dissipation factor which is provided by the manufacturer. The associated ESR r_c along with the RMS value of capacitor ripple current are used to calculate power loss of the capacitor.

5.1.2 Compensator Design

Feedback control is usually used to improve both steady state and dynamic response. As illustrated in Figure 2.10, a compensator $T_c(s)$ is added to improve the performance of the power converter system. For voltage-mode control, there is no inner current loop and the compensator could be Type-II or Type-III. The compensator could be a phase-lag/lead one for buck converter with current-mode

control. Current-mode control is presented to illustrate compensator design. A new small signal model for current-mode control was developed in [1]. The model takes into account the sampling effect due to switching. For convenience, the block diagram is re-state here. This method is based on sampled data modeling

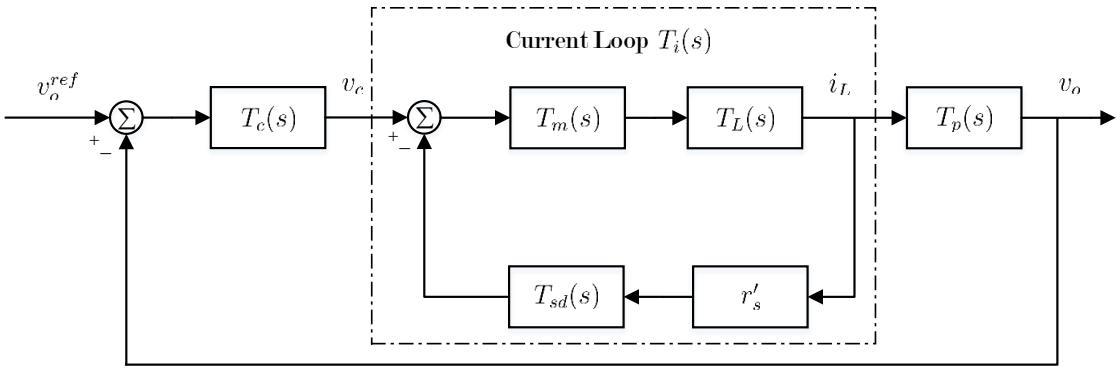

Figure 5.2. Detailed block diagram of current-mode control.

and good accuracy can be expected from dc to half the switching frequency. The control-to-output transfer function is described as

$$\frac{v_o(s)}{v_c(s)} = T_p(s)T_i(s) \tag{5.9}$$

where exact transfer function $T_p(s)$ and $T_i(s)$ [1] are as follows:

$$\begin{aligned}
T_p(s) &= \frac{r_{Co}s + \frac{1}{C_o}}{s + \frac{1}{R_{load}C_o}} \\
T_i(s) &= \frac{\omega_{sd}^2}{r'_s}\frac{1}{s^2 + 2\zeta\omega_{sd}s + \omega_{sd}^2} \\
\omega_{sd} &= \frac{\pi}{T_s} \\
\zeta &= \frac{\pi}{4}\frac{m_1 + m_2 - 2\frac{m_{sc}}{r'_s}}{m_1 - m_2} \\
m_2 &= -\frac{V_o}{L} \\
m_1 &= \frac{V_d - V_o}{L}.
\end{aligned}$$

As can be observed in equation (5.9), this transfer function is dependent on the values of circuit parameters including L and C_o. The control-to-output transfer

functions for the boost and the buck-boost converters are provided in Appendix C.1 and C.2.

With knowledge of $T_p(s)$ and $T_i(s)$ from power stage design, one can choose parameter values of the compensator to improve the performance of buck converter system. A first-order phase lag compensator $T_c(s)$ is given by

$$T_c(s) = K_c \frac{s + \omega_{zc}}{s + \omega_{pc}} \tag{5.10}$$

where the magnitude of ω_{zc} is larger than the magnitude of ω_{pc}. The zero ω_{zc} of compensator could be chosen to cancel the stable pole of the plant transfer function in equation (5.9) or be placed at the one-fifth the selected crossover frequency suggested in [116]. The pole ω_{pc} of compensator is chosen to near the origin, so that it performs as a practical integrator to improve steady state tracking while avoiding saturation.

5.1.3 Input Filter Design

Switching in power converters can result in significant input current ripple. Therefore, it is common to employ an input filter to mitigate power quality problems in the source network. In practical applications, a low pass input filter is usually inserted between the converter and the source network. Thus the input filter reduces source current ripple in i_s while also reducing voltage ripple in v_d presented to the converter. It can also reduce the effect of source transients in v_s on the converter. Ideally, it should appear as a DC source. The voltage ripple of a buck converter at the input capacitor can be calculated as

$$\Delta V_d = \begin{cases} \frac{I_o D_{max}(1-D_{max})}{f_s C_i} & \text{when} \quad D_{max} \leq \frac{1}{2} \\ \frac{I_o D_{min}(1-D_{min})}{f_s C_i} & \text{when} \quad D_{min} > \frac{1}{2} \\ \frac{I_o}{4 f_s C_i} & \text{when} \quad D_{min} \leq \frac{1}{2} \quad \text{and} \quad D_{max} > \frac{1}{2} \end{cases} \tag{5.11}$$

Potential instability caused by insertion of the input filter has motivated much research, and many design criteria have been presented. The fundamental idea behind these criteria is that the input filter should not influence the performance of power converter systems.

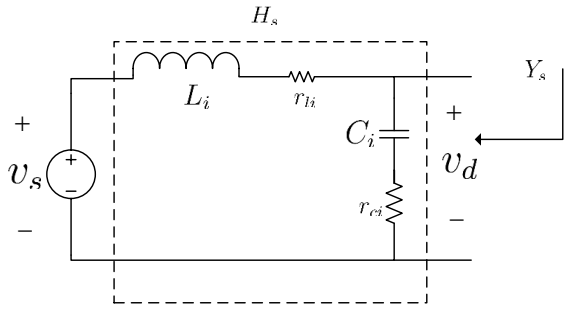

Figure 5.3. Input filter.

Input Filter Design Criteria via *y*-parameter Model

Kohut [22] investigated the effect of the input filter and formulated design constraints using a y-parameter model for current-mode control. The criteria are given in terms of the filter voltage transfer function H_s, output admittance Y_s, and a y-parameter model of the switching converter. The y-parameter mode is an equivalent small signal circuit-oriented model of the current-mode controlled power stage, in which the current loop is no longer visible. There are six parameters in this model, from which the control-to-output transfer function can be determined. The y-parameter model of buck converter [3] shown was derived as:

$$
\begin{aligned}
y_{11} &= -\frac{c_1 D^2}{R}\frac{1+(s/c_1)/(\omega_s/\pi)}{1+s/\omega_c} \\
y_{1c} &= \frac{D}{R_f}\frac{1+sL/R}{1+s/\omega_c} \\
y_{12} &= \frac{c_2 D}{R}\frac{1+(sD/c_2)/(\omega_s/\pi)}{1+s/\omega_c} \\
y_{21} &= -\frac{D(nD'-1)}{KR}\frac{1}{1+s/\omega_c} \\
y_{2c} &= -\frac{1}{R_f}\frac{1}{1+s/\omega_c} \\
y_{22} &= \frac{nD'-D}{KR}\frac{1}{1+s/\omega_c}
\end{aligned}
$$

where $R = V_o/I_o$; $K = \frac{2L}{RT_s}$; $n = 1 + 2m_{sc}/m_L$; ω_s is the angular switching frequency; R_f is the effective current sensing resistor; $\omega_c = \frac{\omega_s}{\pi n D'}$ and $D' = 1 - D$.

A well designed input filter using this y-parameter model should satisfy the

following conditions [22].

$$\begin{aligned} |\frac{y_L}{Y_s}| &\ll 1 & |\frac{y_H}{Y_s}| &\ll 1 \\ |\frac{y_{11}}{Y_s}| &\ll 1 & |H_s| &\leq 1 \end{aligned} \tag{5.12}$$

where

$$\begin{aligned} y_L &= \frac{y_{21}y_{1c}}{y_{2c}} - y_{11} \\ y_H &= y_{11} - \frac{y_{12}y_{21}}{y_{22} + sC_o + \frac{1}{R_{load}}} \end{aligned}$$

y_{ij} are parameters in the y-parameter model. Note that inequality $|H_s| \leq 1$ can be relaxed, so that $3 - 6$ dB is acceptable for peak values for H_s [22].

An input filter can be used to attenuate the noise emissions from the converter without adversely affecting the converter if these conditions are met. Similar input filter design criteria using y-parameter model were obtained in [16] and [26] for boost and buck-boost converters.

5.2 Automated Design Process

In this dissertation, the automated design process illustrated in Figure 1.2 is implemented in MATLAB. The inputs are SSSM of power converter system, bounds of design variables, fixed parameters, and design specifications. The outputs are values of design variables, periodic steady state response of the final design, and objective value of the final design. Automated design process utilizes SSSM to model the system, applies the enhanced Floquet method to determine the steady state and transient performance. A buck converter under current-mode control with input filter and switching frequency ($w_s = 2\pi f_s$) disturbance shown in Figure 5.4 is used as an example. The disturbance signal is model by a sinusoidal signal; $v_o^{ref} = V_o^{ref} + \tilde{v}_o^{ref}(t) = V_o^{ref} + \underline{v}_o^{ref}\cos(w_s t)$. The amplitude of disturbance signal $\underline{v}_o^{ref}$ is chosen to be 0.1% of V_o^{ref}. Different inductor cores result in noticeable different inductance curves and parasitic resistances, thus making it a discrete variable and non-differentiable.

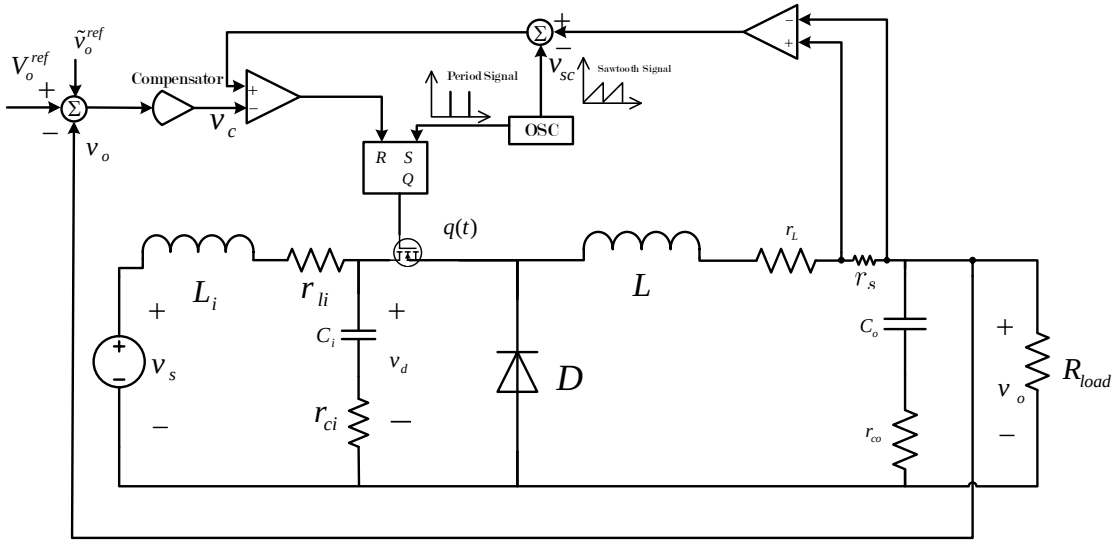

Figure 5.4. Buck converter under current-mode control with input filter and disturbance.

5.2.1 Objective Function

Several objective functions for the multi-objective design optimization of a buck converter with an input filter under current-mode control are defined in this section.

Minimization of Voltage Ripple

Once the system is modeled by SSSM, it is possible to predict the periodic steady state response using the Floquet method. There are two voltages for which peak-to-peak ripple is important: output voltage $v_{o_{pp}}$ and input voltage $v_{d_{pp}}$. Since the system is perturbed by a sinusoidal noise, it is desirable to obtain these ripples from the periodic steady state response obtained by the enhanced Floquet method presented in the previous chapter. In practical applications of power converter systems, output voltage ripples are more important than input voltage ripples and deserve more weight in the objective function.

Minimization of Resistant Losses

It is usually desirable to increase the efficiency of the system, so the energy dissipated by parasitic resistors should be minimized. In the whole system, four parasitic resistors are associated with L, C_o, L_i, and C_i. The resistances are determined by

inductor selection and capacitor selection.

$$P_{loss} = I_l^2 r_l + I_{co}^2 r_{co} + I_{li}^2 r_{li} + I_{ci}^2 r_{ci} \tag{5.13}$$

where I_l, I_{co}, I_{li}, and I_{ci} are RMS values of the currents through L, C_o, L_i, and C_i respectively. These values can also be obtained from the periodic steady state response from the enhanced Floquet method.

Minimization of Settling Time

This objective is presented as a measure of transient response. Other criteria for transient performance such as rise time or peak time can also be considered. In the implementation, the more constraints that there are, the slower the solution. So instead of placing constraints on the real parts of poles of the system, settling time is a better criteria. If the system is not stable, then the settling time would be infinity, resulting in elimination of that candidate design. Settling time is defined as the time required for the response to reach and stay within 2% of its final value.

By the enhanced Floquet method from previous chapter, the SSSM of power converter system can be converted into periodic steady state model described as equation (4.11). Once the parameter values of compensator are determined by GAs, the transient properties can be obtained by converting the discrete-time Poincaré map $(\mathbf{H}_x, \mathbf{H}_u, \mathbf{C}, \mathbf{D})$ to a continuous-time transfer function using a zero-order-hold (MATLAB d2c.m function). MATLAB function (stepinfo.m) calculates the corresponding transient properties given a transfer function. This procedure is similar to that in Section 4.3.

Minimization of the Volume of Power Converter System

The volume of the power converter system is primarily influenced by the inductors and capacitors. Different cores may have significantly different characteristics. Consequently core selection must be treated as a discrete variable. Each core is labeled by an index that is integer-valued. Then the index corresponds to a set of parameters provided by the core manufacturer. Each capacitor is also labeled by an integer index which corresponds to the volume and the dissipation factor. The details of core and capacitor components are given in Table C 1 and C 2 of

Appendix D.

Objective Function

For a multi-objective problem, the weighted sum method is commonly used due to its simplicity. The original optimization problem is converted into a single objective optimization problem by multiplying each objective with a weight and summing them. Due to the different scales and units associated with each criterion, it is usually helpful to normalize each one.

The input and output voltage ripples are normalized by the input voltage V_d and output reference voltage V_o^{ref}, respectively. The resistive loss is normalized by the output power P_o. Settling time is normalized by $10T_s$. In contemporary power converter system, a good choice for the power density is 20 watts/in^3 (1.22 watts/cm^3). So volume is normalized by this power density. Therefore, the following single objective function is obtained.

$$f(\mathbf{x}) = c_1\frac{v_{o_{pp}}}{V_o^{ref}} + c_2\frac{v_{d_{pp}}}{V_d} + c_3\frac{P_{loss}}{P_o} + c_4\frac{\text{Settling Time}}{10T_s} + c_5\frac{\text{Volume}}{\frac{P_o}{20}} \tag{5.14}$$

where c_1 to c_5 are weights that can be adjusted to represent the relevant importance of each sub-objective.

Design Constraints

The design specifications are listed in Table 5.1. Values of fixed parameters are given in Table B.2 of Appendix B.

Specification	Value
Input Voltage Ripple	5%
Output Voltage Ripple	5%
Operating Mode	CCM

Table 5.1. Design specifications.

With respect to these specifications and other issues, constraints for this optimal design problem can be formulated as:

- The inductance inequality (5.1) holds to guarantee CCM operation.

- The core selection inequality (5.4) holds.
- The output voltage ripple (as calculated by equation (5.7))is less than 5% of V_o^{ref}.
- The input voltage ripple (as calculated by equation (5.11))is less than 5% of V_d.
- The input filter design inequalities (5.12) hold.

5.2.2 Formulation of Optimization Problem

The main design variables are L, C_o, L_i, C_i, core indices of L and L_i, and the gain of compensator K_c. Auxiliary design variables associated with main design variables are r_l, r_{co}, r_{li}, and r_{ci}. With the SSSM of buck converter system provided in Appendix E.1 and objective function as equation (5.14), the power converter system design optimization problem is formulated as follows.

$$\min f(\mathbf{x}) = c_1\frac{v_{o_{pp}}}{V_o^{ref}} + c_2\frac{v_{d_{pp}}}{V_d} + c_3\frac{P_{loss}}{P_o} + c_4\frac{\text{Settling Time}}{10T_s} + c_5\frac{\text{Volume}}{\frac{P_o}{20}} \tag{5.15}$$

subject to

$$\begin{aligned}
L &\geq \frac{V_o(V_{d_{max}} - V_o)}{2f_s V_{d_{max}} I_{o_{min}}} \\
L &\leq \frac{K_f^2 W^2 A_L}{10^{-9} A_w^2} \\
\frac{\Delta V_o}{V_o^{ref}} &= \frac{1}{8f_s^2 LC_o}(1 - \frac{V_o}{V_{d_{max}}}) < 5\% \\
\frac{\Delta V_d}{V_d} &= \begin{cases} \frac{I_o D_{max}(1-D_{max})}{f_s C_i V_d} & \text{when} \quad D_{max} \leq \frac{1}{2} \\ \frac{I_o D_{min}(1-D_{min})}{f_s C_i V_d} & \text{when} \quad D_{min} > \frac{1}{2} \\ \frac{I_o}{4f_s C_i V_d} & \text{when} \quad D_{min} \leq \frac{1}{2} \quad \text{and} \quad D_{max} > \frac{1}{2} \end{cases} < 5\% \\
|\frac{y_L}{Y_s}| &\ll 1 \\
|\frac{y_H}{Y_s}| &\ll 1 \\
|\frac{y_{11}}{Y_s}| &\ll 1 \\
|H_s| &\leq 1
\end{aligned} \tag{5.16}$$

where

$$
\begin{aligned}
y_L &= \frac{y_{21}y_{1c}}{y_{2c}} - y_{11} \\
y_H &= y_{11} - \frac{y_{12}y_{21}}{y_{22} + sC_o + \frac{1}{R_{load}}} \\
y_{11} &= -\frac{c_1 D^2}{R}\frac{1 + (s/c_1)/(\omega_s/\pi)}{1 + s/\omega_c} \\
y_{1c} &= \frac{D}{R_f}\frac{1 + sL/R}{1 + s/\omega_c} \\
y_{12} &= \frac{c_2 D}{R}\frac{1 + (sD/c_2)/(\omega_s/\pi)}{1 + s/\omega_c} \\
y_{21} &= -\frac{D(nD' - 1)}{KR}\frac{1}{1 + s/\omega_c} \\
y_{2c} &= -\frac{1}{R_f}\frac{1}{1 + s/\omega_c} \\
y_{22} &= \frac{nD' - D}{KR}\frac{1}{1 + s/\omega_c} \\
Y_s &= \frac{C_i L_i s^2 + (r_{li} + rci)s + 1}{C_i L_i r_{ci} s^2 + (L_i + C_i r_{ci} r_{li})s + r_{li}} \\
H_s &= \frac{C_i r_{ci} + 1}{L_i s^2 + (r_{li} + rci)s + 1}
\end{aligned}
$$

and $R = V_o/I_o$; $K = \frac{2L}{RT_s}$; $n = 1 + 2m_{sc}/m_L$; ω_s is the angular switching frequency; R_f is the effective current sensing resistor; $\omega_c = \frac{\omega_s}{\pi n D'}$ and $D' = 1 - D$. The operation $\ll 1$ is implemented as < 0.1.

Figure 5.5 shows the flow chart of optimization computation. Auxiliary variables r_l, r_{co}, r_{li}, and r_{ci} are determined by main design variables L, C_o, L_i, C_i, and core indices of L and L_i. The computation uses main design variables and auxiliary variables to build the SSSM of the power converter system. Then the periodic steady state responses can be calculated by the Floquet method and SSSM. The computation of periodic steady state reponses is computation intensive. Metrics including input and output voltage ripples, RMS values of currents through both inductors and capacitors, settling time, and volume can be determined from the periodic steady state responses. Finally, a numeric value is assigned to the objective function by summing these normalized metrics.

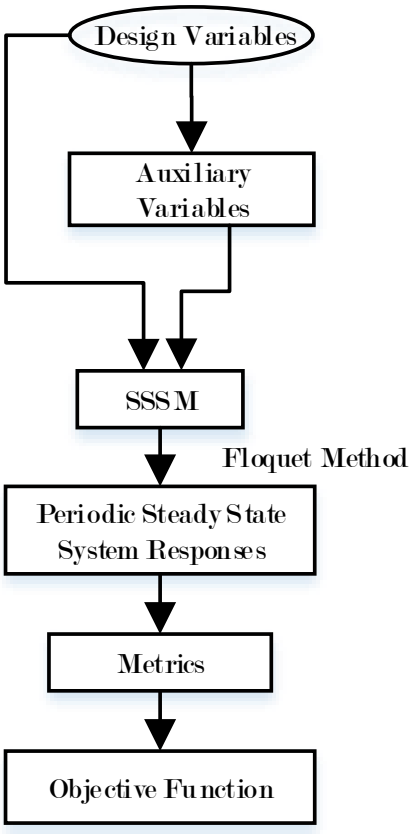

Figure 5.5. Flow chart of optimization computation.

When performing design optimization of power converter system, the design may be trapped by some local minima that can stop the optimization searching process. The global minimum for the optimization problem cannot be guaranteed. Thus, special considerations are needed for the optimization algorithm when the global minimum or near-global minimum is expected for the optimization problem.

5.2.3 Solution of the Optimization Problem using Genetic Algorithms

In this section, Genetic Algorithms (GAs) are used to solve the design optimization shown in Figure 5.4. Since the inductor and capacitor design requires selections from discrete sets of cores and capacitor components, this makes it a mixed integer optimization problem. The solution to such problem can be determined by some

algorithms, such as GAs, branch and bound algorithm, and Dakin's algorithm. Since GAs are heuristic global search process for the solution and popular in the literature, they are used to solve the optimization problem.

The automated design process using GAs is illustrated as Figure 3.1. The bounds of the design variables are set wide to keep the design from local minimum solutions. All the design variables are coded into a individual chromosome which represents a possible solution for the design. Then GAs evaluate the corresponding objective function values of equation (5.14) using periodic steady state solutions from the Floquet method. A fitness value is assigned to all individuals. Those with higher fitness values are more likely to be chosen to reproduce and create new population through operations of selection, crossover, and mutation. This process runs from generation to generation until termination condition is reached. The final output of automated design process is a set of design variable values that minimizes the objective equation (5.14) and satisfies all constraints.

Using the SSSM obtained in Appendix E.1, the design optimization problem equation (5.15), and constraints equation (5.16), results of design optimization problem for the buck converter system with input filter under current-mode control are given in Table 5.2.

Design Variable	Value
L	48 μH
C_o	170 μF
K_c	0.68
L_i	130 μH
C_i	110 μF
Output Core Type	0C40502TC
Input Core Type	0F40301TC

Table 5.2. Optimization results for system designed using automated design process.

Objective value obtained is 1.25. Figure 5.6 shows periodic steady state response using the design generated via GAs optimization. It shows output voltage v_o, inductor current i_L, output capacitor voltage v_{Co}, input inductor current i_{Li}, input capacitor voltage v_{Ci}, current reference signal $i_L^\star$, and compensator state x_{ctr}.

Each of these responses follows a stable periodic orbit. This is consistent with the locations of Floquet multipliers shown in Figure 5.7; all are within unit circle.

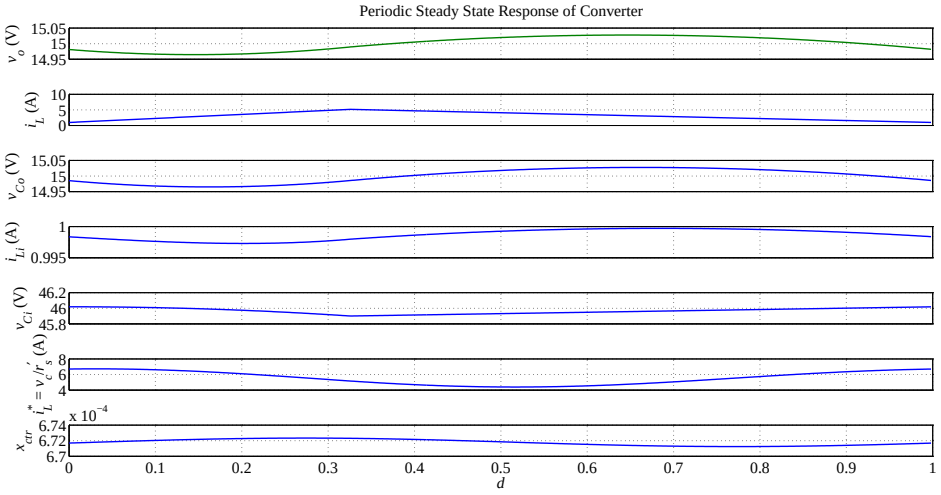

Figure 5.6. Periodic steady state response for system designed using automated design process.

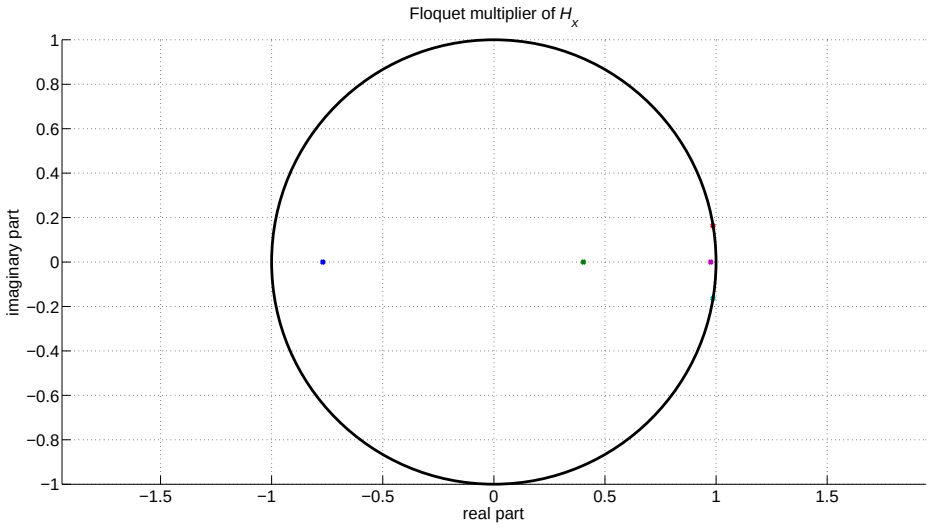

Figure 5.7. Floquet multipliers for system designed using automated design process.

From Figure 5.6, the buck converter system is operating in CCM. The output ripple is 0.06 V, which is less than $5\% \cdot V_o^{ref} = 0.75$ V. The input ripple is 0.12 V, which is less than $5\% \cdot V_d = 2.30$ V. All other constraints are also satisfied.

5.3 Conventional Design Process

The conventional design process is presented as a basis for comparison to the results from the automated design process described in Section 5.2. In the conventional design process, the three subsystems are designed sequentially using well established techniques. Given the design specifications, the conventional design process of buck converter with input filter under current-mode control as illustrated in Figure 5.4 follows the flow chart illustrated in Figure 1.1.

The design of each subsystem is cast as a constrained optimization problem. Usually, the power stage is considered first. Next, feedback control is added to improve the performance of the power stage. Finally, the input filter is designed so as to avoid interfering with the performance of the controlled power stage. All fixed parameter values of the system including V_d, V_o, f_s, R_{load}, and r'_s are chosen to be the same as those in the automated design process, as shown in Appendix B.2.

5.3.1 Power Stage Design

In conventional analysis, the most widely accepted model is the state space averaging model that is presented in Section 2.2.2. Using this model, steady state and transient properties can be assessed, based on which a constrained optimization can be formulated.

Problem Formulation

For power stage design, main design variables are chosen as L and C_o and auxiliary variables are r_L and r_{co}. The objective function can be constructed as weighed summation of output voltage ripple, resistant loss, and settling time. The constraints are the power stage is operating in CCM and output voltage ripple is less than 5% of the output voltage reference. Then the constrained optimization design of power stage is formulated as follows:

$$\min f(\mathbf{x}) = c_1 \frac{v_{o_{pp}}}{V_o^{ref}} + c_2 \frac{P_{loss}}{P_o} + c_3 \frac{\text{Settling Time}}{10T_s}$$

subject to

$$\begin{aligned} L &\geqslant \frac{V_o(V_{d_{max}} - V_o)}{2f_s V_{d_{max}} I_{o_{min}}} \\ \frac{\Delta V_o}{V_o^{ref}} &= \frac{1}{8f_s^2 L C_o}(1 - \frac{V_o}{V_{d_{max}}}) < 5\%. \end{aligned}$$

Since the type of core is discrete variable and conventional optimization faces difficulties with discrete variables, the core selection can be determined by first calculating the maximum energy LI_{max} that the core should handle the worst-case current I_{max}. Next, useable cores can be determined by referring to the manufacturer's data sheet. Each useable core should also satisfy core selection inequality (5.4). The associated resistance r_L is calculated as equation (5.5). The capacitor is selected the same as described in Section 5.1.1 and ESR is calculated as equation(5.8). The optimization results for power stage are shown in Table 5.3.

Design Variable	Value
L	35 μH
C_o	21 μF

Table 5.3. Optimization results for power stage designed using conventional design process.

5.3.2 Compensator Design

Once L and C_o have been designed for the power stage, the compensator is designed to improve the response of the system. For current-mode controlled buck converter, Ridley's model [1] for the power stage and current loop is usually used. Once the parameter values for inductor L and capacitor C_o are determined for the power stage, the current-loop transfer function $T_i(s)$ and power stage transfer function $T_p(s)$ in Figure 5.2 are determined. A phase-lag compensator that has the same structure as that in automated design process is used to make the comparison. The pole is chosen to be near the origin so that it acts as a practical integrator to avoid saturation and the zero is chosen to cancel the stable pole of the power stage. So the gain of the compensator K_c is the design variable of the for compensator design. At this stage, transient properties such as settling time could be chosen to

measure the performance of the compensator, which can be obtained using classical linear theory by using Ridley's model of the closed loop system shown in Figure 5.2. The objective function could be defined as follows.

$$\min f(\mathbf{x}) = \frac{\text{Settling Time}}{10T_s}$$

However, a disadvantage here is that the range of K_c that stabilizes the system is limited, since the inductance and capacitance of power stage are already determined in power stage design. So the design may be trapped into a local minimum. The optimization result for compensator is shown in Table 5.4.

Design Variable	Value
K_c	0.09

Table 5.4. Optimization result for compensator designed using conventional design process.

5.3.3 Input Filter Design

An input filter is usually inserted between the utility supply and the power stage to improve the power quality. Kohut [22] proposed several inequalities for the design of input filter as shown in equation (5.12). The input filter is designed in the way that the performance of the controlled power stage cannot be affected.

Problem Formulation

The main design variables are chosen as L_i and C_i and auxiliary variables are r_{li} and r_{ci}. The amplitude of the input voltage ripple ΔV_d is expected to be less than 5% of the input voltage V_d. So when designing the input filter, the objective and constraints become as follows. Then the constrained optimization design of power stage is formulated as follows:

$$\min f(\mathbf{x}) = c_4 \frac{v_{d_{pp}}}{V_d} + c_5 \frac{P_{loss}}{P_o}$$

subject to

$$\begin{aligned}
\frac{\Delta V_d}{V_d} &= \begin{cases} \frac{I_o D_{max}(1-D_{max})}{f_s C_i V_d} & \text{when} \quad D_{max} \le \frac{1}{2} \\ \frac{I_o D_{min}(1-D_{min})}{f_s C_i V_d} & \text{when} \quad D_{min} > \frac{1}{2} \\ \frac{I_o}{4 f_s C_i V_d} & \text{when} \quad D_{min} \le \frac{1}{2} \quad \text{and} \quad D_{max} > \frac{1}{2} \end{cases} < 5\% \\
|\frac{y_L}{Y_s}| &\ll 1 \\
|\frac{y_H}{Y_s}| &\ll 1 \\
|\frac{y_{11}}{Y_s}| &\ll 1 \\
|H_s| &\le 1
\end{aligned}$$

where

$$\begin{aligned}
y_L &= \frac{y_{21} y_{1c}}{y_{2c}} - y_{11} \\
y_H &= y_{11} - \frac{y_{12} y_{21}}{y_{22} + sC_o + \frac{1}{R_{load}}} \\
y_{11} &= -\frac{c_1 D^2}{R} \frac{1 + (s/c_1)/(\omega_s/\pi)}{1 + s/\omega_c} \\
y_{1c} &= \frac{D}{R_f} \frac{1 + sL/R}{1 + s/\omega_c} \\
y_{12} &= \frac{c_2 D}{R} \frac{1 + (sD/c_2)/(\omega_s/\pi)}{1 + s/\omega_c} \\
y_{21} &= -\frac{D(nD' - 1)}{KR} \frac{1}{1 + s/\omega_c} \\
y_{2c} &= -\frac{1}{R_f} \frac{1}{1 + s/\omega_c} \\
y_{22} &= \frac{nD' - D}{KR} \frac{1}{1 + s/\omega_c} \\
Y_s &= \frac{C_i L_i s^2 + (r_{li} + rci)s + 1}{C_i L_i r_{ci} s^2 + (L_i + C_i r_{ci} r_{li})s + r_{li}} \\
H_s &= \frac{C_i r_{ci} + 1}{L_i s^2 + (r_{li} + rci)s + 1}
\end{aligned}$$

and $R = V_o/I_o$; $K = \frac{2L}{RT_s}$; $n = 1 + 2m_{sc}/m_L$; ω_s is the angular switching frequency; R_f is the effective current sensing resistor; $\omega_c = \frac{\omega_s}{\pi n D'}$ and $D' = 1 - D$. The operation $\ll 1$ is implemented as < 0.1. The optimization results for input filter are shown in Table 5.5.

Design Variable	Value
L_i	1 μH
C_i	420 μF

Table 5.5. Optimization results for input filter designed using conventional design process.

5.3.4 Optimization Results using Conventional Design Process

The bounds of the design variables are the same as those in automated design process. Using classical constrained optimization techniques discussed in Section 3.1, the design optimization are obtained by sequentially solving constrained optimization problems for three stages in power converter system. The design optimization results of the whole system are summarized in Table 5.6.

Design Variable	Value
L	35 μH
C_o	21 μF
K_c	0.09
L_i	1 μH
C_i	420 μF

Table 5.6. Optimization results for system designed using convention design process.

Figure 5.8 shows the stable periodic steady state response for the converter system designed using the convention design process. This is consistent with the locations of Floquet multipliers shown in Figure 5.9; all are within unit circle. It shows output voltage v_o, inductor current i_L, output capacitor voltage v_{Co}, input inductor current i_{Li}, input capacitor voltage v_{Ci}, current reference signal $i_L^\star$, and compensator state x_{ctr}.

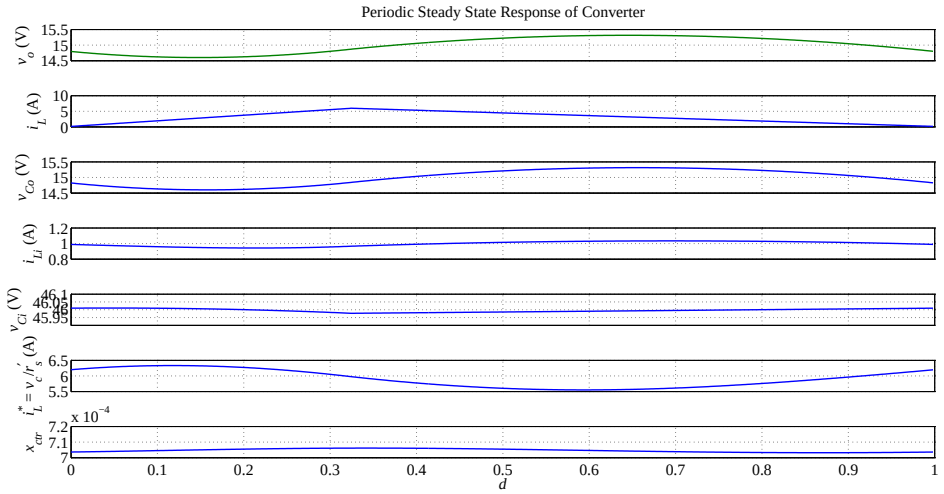

Figure 5.8. Periodic steady state response of system designed using conventional design process.

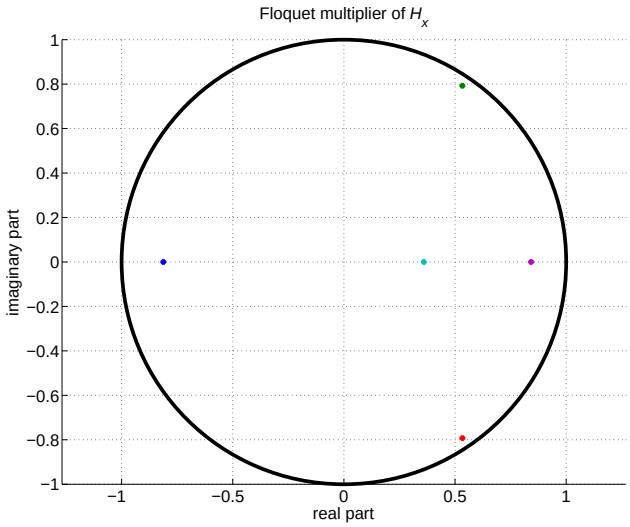

Figure 5.9. Floquet multipliers of system designed using conventional design process.

From Figure 5.8, the buck converter system is operating in CCM. The output voltage ripple is 0.71 V, which is less than $5\% \cdot V_o^{ref} = 0.75$ V. The input voltage ripple is 0.04 V , which is less than $5\% \cdot V_d = 2.30$ V. All other constraints are also satisfied. The objective value of the conventional design is 0.57. Note that this objective value does include the volume of power converter system.

5.4 Design of Boost and Buck-Boost Converter by Automated Design Process

To verify the versatility of the automated design process, results for two different converters, the boost converter and the buck-boost converter are presented in this section.

5.4.1 Right-Half-Plane Zero

For current-mode controlled boost and buck-boost converters that are operated in continuous conduction mode, a right-half-plane zero is encountered in small signal analysis. The control-to-output transfer functions of boost and buck-boost converter [117] are provided in Appendix C. The right-half-plane zero provides 20 db/decade gain and 90° phase lead. This can cause the power converter system to be unstable if the compensator is chosen as typical phase-lead/lag one.

Originally, the compensator is chosen to be a standard phase-lead/lag one and attempt of design boost and buck-boost converter systems using automated design process is made. But the design witnesses stability issue the same as that in small signal analysis. One remedy to compensate the effect of this right-half-plane zero is to use a Type II compensator [116].

$$T_c(s) = K_c \frac{s + \omega_{zc}}{(s + \omega_{pc1})(s + \omega_{pc2})}$$

The closed-loop SSSM of boost and buck-boost converter systems using this Type II compensator are derived in Appendix E.

5.4.2 Results of Automated Design Process

The design objective function is the same as those in Section 5.2. The fixed parameters are provided in Appendix B. Using the SSSM defined in Appendix E.2 and E.3, design optimization results for the boost and buck-boost converter systems with input filter under current-mode control are given in Table 5.7 and 5.8. The objective values obtained are 26.23 and 40.24 for the boost and the buck-boost design, respectively.

Design Variable	Value
L	247 μH
C_o	17.5 μF
K_c	1.1
L_i	276 μH
C_i	36.9 μF
ω_{pc1}	0.0013 rad/s
ω_{pc2}	1.34×10^3 rad/s
ω_{zc}	4.29×10^4 rad/s
Output Core Type	0R40301TC
Input Core Type	0F40401TC

Table 5.7. Optimization results for boost converter system designed using automated design process.

Design Variable	Value
L	1.45 mH
C_o	20.4 μF
K_c	1.71
L_i	472 μH
C_i	172 μF
ω_{pc1}	0.0036 rad/s
ω_{pc2}	8.35×10^2 rad/s
ω_{zc}	6.57×10^3 rad/s
Output Core Type	0F40301TC
Input Core Type	0F40301TC

Table 5.8. Optimization results for buck-boost converter system designed using automated design process.

The periodic steady state responses for the boost and the buck-boost converters are shown in Figures 5.10 and 5.11. They show output voltage v_o, inductor current i_L, output capacitor voltage v_{Co}, input inductor current i_{Li}, input capacitor voltage v_{Ci}, current reference signal $i_L^\star$, and compensator states $x_{1_{cont}}$ and $x_{2_{cont}}$. Each of

these responses follows a stable periodic orbit. This is consistent with the absolute values of all Floquet multipliers being within the unit circle. From Figure 5.10,

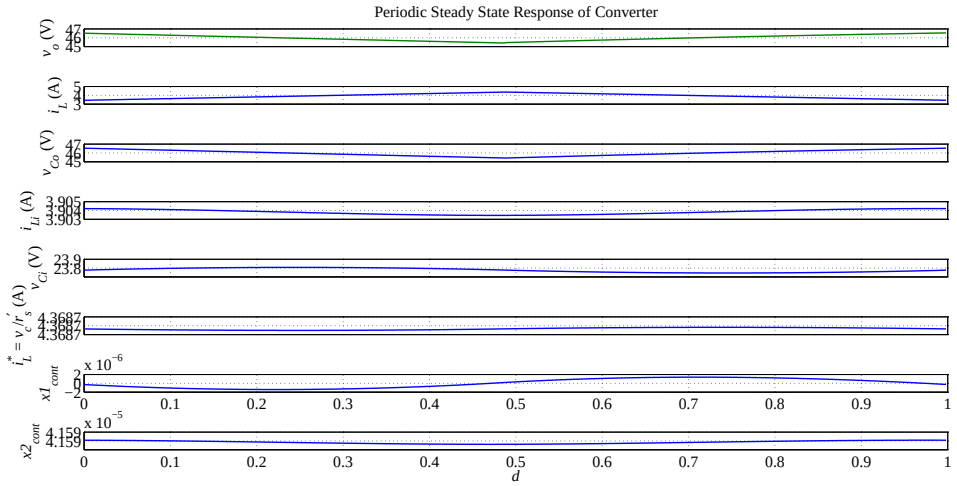

Figure 5.10. Periodic steady state response of boost converter design.

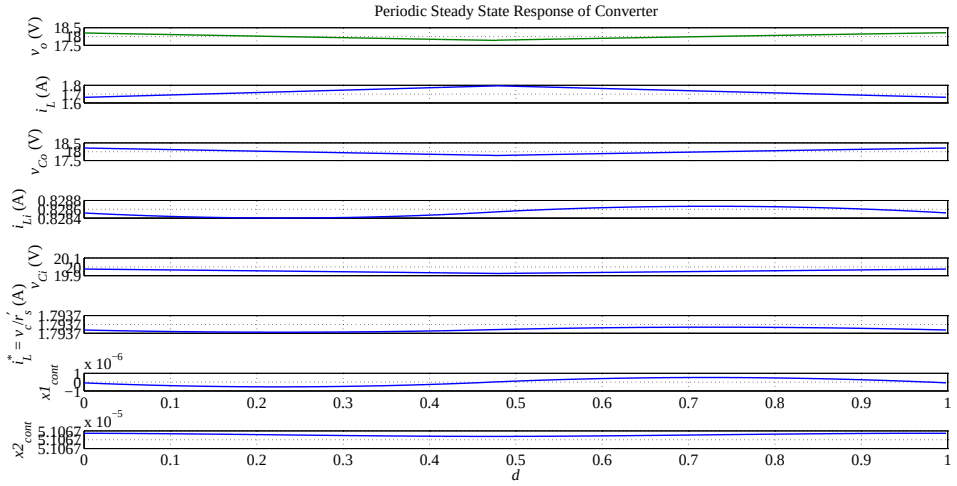

Figure 5.11. Periodic steady state response of buck-boost converter design.

the boost converter system is operating in CCM. The output ripple is 0.44 V, which is less than $5\% \cdot V_o^{ref} = 0.90$ V. The input ripple is 0.05 V, which is less than $5\% \cdot V_d = 1.15$ V. All constraints are satisfied by the optimal design using GAs. From Figure 5.11, the buck-boost converter system is operating in CCM.

The output voltage ripple is 0.43 V, which is less than $5\% \cdot V_o^{ref} = 2.3$ V. The input voltage ripple is 0.06 V, which is less than $5\% \cdot V_d = 1$ V. All other constraints are also satisfied.

5.5 Summary

In this chapter, two design processes for power converter systems have been presented. In the automated design process, the enhanced Floquet method and GAs are used to determine the values of design variables including power stage, compensator, and input filter that minimize the objective function (equation (5.14)). In the conventional design process, the design is partitioned into three stages. These three stages are handled sequentially as constrained optimization problems using classical optimization techniques. The individual objective function values for each design process are given side by side in Table 5.9.

Objective	Conventional Design Process	Automated Design Process
Output Voltage Ripples (V)	0.71	0.12
Input Voltage Ripples (V)	0.04	0.06
Power Loss (W)	0.22	0.29
Settling Time (ms)	10.2	10.2
Volume (in^3)	1.78	1.69
Objective Value	0.57	1.27
Psudo Value	1.34	0.53

Table 5.9. Comparison of objective values for the conventional design process and the automated design process.

All objective function values are normalized as explained in Section 5.2.1. The performance of the automated design process is better than that of the conventional design process. Since the volume is excluded in the conventional design process, psudo objective value is introduced. For the conventional design process, the psudo objective value is the objective value of equation (5.14) plus the normalized volume of the power converter system. Similarly, the psudo objective value for the automated design is the objective value of equation (5.14) minus the normalized volume. Thus, the objective value of the conventional design process and the psudo objective value of the automated design process are comparable; the psudo

objective value of the conventional design process and the objective value of the automated design process are comparable. From these results, the performance of the power converter system is improved by approximately 7% by automated design process.

Design Variable	Conventional Design Process	Automated Design Process
L	35 μH	48 μH
C_o	21 μF	170 μF
K_c	0.09	0.68
L_i	1 μH	130 μH
C_i	420 μF	110 μF

Table 5.10. Comparison of design variables values for the conventional design process and the automated design process.

The values of design variables for each design process are given side by side in Table 5.10. In the automated design process, the larger power stage capacitor and the smaller input capacitor result in smaller output voltage ripple and larger input voltage ripple than those in the conventional design process, respectively. However, the input inductor and the compensator gain are larger than those in the conventional design process. When the load changes abruptly, this could cause the inductor drawing more energy from the source, deteriorating the dynamics of the system, and maybe even collapsing the source. The inclusion of transient simulation may be helpful to guarantee the dynamics of the system. Thus, more attention should be made for the transient response in the future work.

Chapter 6

Conclusions and Future Work

6.1 Summary

In this dissertation, the existing Floquet method for power converter system modeling is enhanced. In particular, a multi-period solver is added and sinusoidal input signals are admitted. In addition, the enhanced Floquet method is incorporated into an automated design process. Several converters are used as examples with the current-mode controlled buck converter being the most prevalent.

The existing Floquet method uses accurate model for networks with ideal switches and is capable of handling systems with multiple switches and multiple topologies. It is fast for steady state parametric studies. However, only piecewise constant input signals are permitted and the periodic steady state response can only be calculated for single-period, although this is sufficient for determining stability in the case of sub-harmonic oscillations.

To calculate the periodic steady state response for multiple periods, a multi-period solver is developed. This multi-period solver is a preprocessor that uses the SSSM of a single-period system and determines the new SSSM that has more topologies and switching surfaces. The multi-period solver permits determination of the actual periodic steady state response at sub-harmonic frequency and calculation of the system response to input signals or disturbance signals that are sub-harmonic to the switching frequency.

Accepting sinusoidal inputs permits the modeling of disturbance signals and modeling of ac-to-dc rectifiers. Disturbance signals are modeled as sinusoidal sig-

nals. By partition the sinusoidal signals into constant signals and time-varying signals, admission of sinusoidal input signals is achieved through modification of the switching condition inequality and derivation of control matrix $\mathbf{H}_u$. Solver efficiency is also improved through the derivation of the closed-form expressions for the zero-state response to sinusoidal inputs. The enhanced Floquet method enables frequency-domain analysis of the system and investigation of the affect of sinusoidal signals to the system.

The the enhanced Floquet method is used to determine the frequency response from input voltage to output voltage of a buck converter under current-mode control with switching frequency disturbance. The exact frequency responses from input voltage to output voltage at harmonics and sub-harmonics of the same buck converter are also calculated. These frequency responses are compared with those obtained from small signal analysis and PSIM commercial circuit simulation. The results obtained from the enhanced Floquet method are more accurate than those obtained from the small signal analysis.

Tradeoffs are inevitable difficulties when one designs power converter systems. Larger volumes of inductor and capacitor lead to small ripples and good stability, whereas the smaller size of power converter systems becomes increasingly desirable. Design considerations including power stage design, inductor core selection, capacitor selection, compensator design, and input filter design are discussed. The automated design process uses the enhanced Floquet method and optimization algorithms to determine the values of design variables that are the solution of the optimization problem, given the design specifications. The discrete properties of inductor core selection and capacitor selection make it a mixed integer optimization problem. Genetic algorithms are used because they are a popular remedy to solve such optimization problem in the literature. The conventional design process is presented as a basis for comparison to the results from the automated design process. In the conventional design process, three stages of power converter systems are separately and sequentially designed as constrained optimization problems.

The automated design process is a systematic algorithm that only needs design specifications and SSSM of the power converter system and could determine values of the design variables of the power converter system with little human designers' interference. It evaluates a large number of possible sets of design variables and

searches the fittest solution. Because this process chooses all design variables as one optimization problem, it has better opportunity to locate a set of near-global optimum than conventional design process has. The automated design process using the enhanced Floquet method can be applied to other switched power converter systems, including buck, boost, and buck-boost power converter systems. It can also accommodate different type of compensator and different control strategies such as fixed duty cycle control, voltage-mode control, and current-mode control.

6.2 Future Work

Several items that require additional attention are as follows. For the enhanced Floquet method:

- The summations in the closed-form expressions of $\mathbf{H}_x$ and $\mathbf{H}_u$ could be simplified.
- The closed-form expressions of $\mathbf{H}_x$ and $\mathbf{H}_u$ could be derived for a new switching condition equation that accommodates discrete-time control.
- The closed-form expressions for the zero-state response to sinusoidal inputs could be enhanced to support Jordan canonical form.
- A study of how the amplitude of sinusoidal disturbance signal affects frequency response of the power converter system could be helpful.

For the automated design process:

- The switching frequency could be treated as a design variable, which results in the transistor/diode selection available.
- Switching loss, conduction loss, core loss, packaging/thermal considerations, and selection of compensator type could be included in the objectives and constraints.
- The transient response associated with the objective function could be improved to provide a better estimation of system dynamics.

- Inductor design for cores with soft magnetic characteristics could be incorporated in the automated design process.
- Given a desired capacitance, determination of combination of capacitors could be useful.

Appendix A

Derivation of Closed-Form Expressions for Zero-State Response to Bohl-type Inputs

Derivation of Equation (4.19)

$$\begin{aligned}
\mathbf{\Phi}(t,t_0) &= e^{\mathbf{A}(t-t_0)} \\
&= e^{(\mathbf{PT})\mathbf{T}^{-1}\mathbf{\Lambda T}(\mathbf{PT})^{-1}(t-t_0)} \\
&= (\mathbf{PT})e^{\mathbf{T}^{-1}\mathbf{\Lambda T}(t-t_0)}(\mathbf{PT})^{-1} \\
&= \left[\begin{array}{cc} Re(\mathbf{p}_1) & Im(\mathbf{p}_1) \end{array}\right] e^{\mathbf{T}^{-1}\mathbf{\Lambda T}(t-t_0)} \left[\begin{array}{cc} Re(\mathbf{p}_1) & Im(\mathbf{p}_1) \end{array}\right]^{-1}
\end{aligned}$$

where

$$\begin{aligned}
e^{\mathbf{T}^{-1}\mathbf{\Lambda T}(t-t_0)} &= \mathbf{T}^{-1}e^{\mathbf{\Lambda}(t-t_0)}\mathbf{T} \\
&= \left[\begin{array}{cc} 1 & 1 \\ j & -j \end{array}\right] \left[\begin{array}{cc} e^{\lambda_1(t-t_0)} & 0 \\ 0 & e^{\lambda_1^*(t-t_0)} \end{array}\right] \frac{1}{2} \left[\begin{array}{cc} 1 & -j \\ 1 & j \end{array}\right] \\
&= \frac{1}{2}\left[\begin{array}{cc} 1 & 1 \\ j & -j \end{array}\right] \left[\begin{array}{cc} e^{(\alpha_1+j\omega_1)(t-t_0)} & 0 \\ 0 & e^{(\alpha_1-j\omega_1)(t-t_0)} \end{array}\right] \left[\begin{array}{cc} 1 & -j \\ 1 & j \end{array}\right] \\
&= \frac{1}{2}e^{\alpha_1(t-t_0)}\left[\begin{array}{cc} 1 & 1 \\ j & -j \end{array}\right] \left[\begin{array}{cc} e^{j\omega_1(t-t_0)} & 0 \\ 0 & e^{-j\omega_1(t-t_0)} \end{array}\right] \left[\begin{array}{cc} 1 & -j \\ 1 & j \end{array}\right]
\end{aligned}$$

$$
\begin{aligned}
&= \frac{1}{2}e^{\alpha_1(t-t_0)}\begin{bmatrix} e^{j\omega_1(t-t_0)}+e^{-j\omega_1(t-t_0)} & -je^{j\omega_1(t-t_0)}+je^{-j\omega_1(t-t_0)} \\ je^{j\omega_1(t-t_0)}-je^{-j\omega_1(t-t_0)} & e^{j\omega_1(t-t_0)}+e^{-j\omega_1(t-t_0)} \end{bmatrix} \\
&= e^{\alpha_1(t-t_0)}\begin{bmatrix} \cos(\omega_1(t-t_0)) & \sin(\omega_1(t-t_0)) \\ -\sin(\omega_1(t-t_0)) & \cos(\omega_1(t-t_0)) \end{bmatrix}
\end{aligned}
$$

Derivation of Equation (4.21)

$$
\begin{aligned}
\mathbf{q}_k e^{\Lambda_k(t-t_0)}\mathbf{r}_k &= \mathbf{q}_k e^{\alpha_1(t-t_0)}\begin{bmatrix} \cos(\omega_1(t-t_0)) & \sin(\omega_1(t-t_0)) \\ -\sin(\omega_1(t-t_0)) & \cos(\omega_1(t-t_0)) \end{bmatrix}\mathbf{r}_k \\
&= e^{\alpha_1(t-t_0)}\left(\cos(\omega_1(t-t_0))\mathbf{q}_k\begin{bmatrix} 1 & 0 \\ 0 & 1 \end{bmatrix}\mathbf{r}_k + \sin(\omega_1(t-t_0))\mathbf{q}_k\begin{bmatrix} 0 & 1 \\ -1 & 0 \end{bmatrix}\mathbf{r}_k\right) \\
&= e^{\alpha_k(t-t_0)}(\cos(\omega_k(t-t_0))\mathbf{q}_k\mathbf{r}_k - \sin(\omega_k(t-t_0))\mathbf{q}_k\mathbf{J}\mathbf{r}_k \\
&= e^{\alpha_k(t-t_0)}(\cos(\omega_k(t-t_0))\mathbf{M}_{ck} - \sin(\omega_k(t-t_0))\mathbf{M}_{sk}
\end{aligned}
$$

where

$$
\mathbf{J} = \begin{bmatrix} 0 & -1 \\ 1 & 0 \end{bmatrix}
$$

Zero-State Response to a Constant Input $u_p(t) = 1$ for Real Mode

$$
\begin{aligned}
\mathbf{\Psi}(t,t_0)|_{u_p(t)} &= \int_{t_0}^{t}\mathbf{\Phi}(t,\tau)\mathbf{b}_p u_p(\tau)d\tau \\
&= \int_{t_0}^{t} e^{\lambda_k(t-\tau)}d\tau\mathbf{M}_k\mathbf{b}_p \\
&= \begin{cases} \frac{-1+e^{\lambda_k(t-t_0)}}{\lambda_k}\mathbf{M}_k\mathbf{b}_p & \text{if}\lambda_k \neq 0 \\ (t-t_0)\mathbf{M}_k\mathbf{b}_p & \text{if}\lambda_k = 0 \end{cases}
\end{aligned} \tag{A.1}
$$

Zero-State Response to a Constant Input $u_p(t) = 1$ for Complex Mode

$$
\begin{aligned}
\mathbf{\Psi}(t,t_0)|_{u_p(t)} &= \int_{t_0}^{t}\mathbf{\Phi}(t,\tau)\mathbf{b}_p u_p(\tau)d\tau \\
&= \frac{-\alpha_k + e^{\lambda_k(t-t_0)}[\alpha_k\cos(\omega_k(t-t_0)) + \omega_k\sin(\omega_k(t-t_0))]}{\alpha_k^2+\omega_k^2}\mathbf{M}_{ck}\mathbf{b}_p \\
&\quad + \frac{-\omega_k + e^{\lambda_k(t-t_0)}[-\alpha_k\sin(\omega_k(t-t_0)) + \omega_k\cos(\omega_k(t-t_0))]}{\alpha_k^2+\omega_k^2}\mathbf{M}_{sk}\mathbf{b}_p
\end{aligned}
$$

(A.2)

Zero-State Response to a Sinusoidal Input $u_p(t) = \cos(\omega_p t + \phi_p)$ for Real Mode

$$\begin{aligned}
\mathbf{\Psi}(t,t_0)|_{u_p(t)} &= \int_{t_0}^{t} \mathbf{\Phi}(t,\tau)\mathbf{b}_p u_p(\tau)d\tau \\
&= \int_{t_0}^{t} e^{\lambda_k(t-\tau)}\cos(\omega_p t+\phi_p)d\tau \mathbf{M}_k\mathbf{b}_p \\
&= \frac{-\lambda_k\cos(\omega_p t+\phi_p)+\omega_p\sin(\omega_p t+\phi_p)}{\lambda_k^2+\omega_p^2}\mathbf{M}_k\mathbf{b}_p \\
&\quad +\frac{e^{\lambda_k(t-t_0)}(\lambda_k\cos(\omega_p t_0+\phi_p)-\omega_p\sin(\omega_p t_0+\phi_p))}{\lambda_k^2+\omega_p^2}\mathbf{M}_k\mathbf{b}_p
\end{aligned} \tag{A.3}$$

Zero-State Response to a Sinusoidal Input $u_p(t) = \cos(\omega_p t + \phi_p)$ for Complex Mode

$$\begin{aligned}
\mathbf{\Psi}(t,t_0)|_{u_p(t)} &= \int_{t_0}^{t} \mathbf{\Phi}(t,\tau)\mathbf{b}_p u_p(\tau)d\tau \\
&= \int_{t_0}^{t} e^{\alpha_k(t-\tau)}\cos((\omega_k-\omega_p)\tau-\omega_k t)d\tau(\frac{1}{2}A_p\mathbf{M}_{ck}\mathbf{b}_p+\frac{1}{2}B_p\mathbf{M}_{sk}\mathbf{b}_p) \\
&\quad +\int_{t_0}^{t} e^{\alpha_k(t-\tau)}\sin((\omega_k-\omega_p)\tau-\omega_k t)d\tau(-\frac{1}{2}B_p\mathbf{M}_{ck}\mathbf{b}_p+\frac{1}{2}A_p\mathbf{M}_{sk}\mathbf{b}_p) \\
&\quad +\int_{t_0}^{t} e^{\alpha_k(t-\tau)}\cos((\omega_k+\omega_p)\tau-\omega_k t)d\tau(\frac{1}{2}A_p\mathbf{M}_{ck}\mathbf{b}_p-\frac{1}{2}B_p\mathbf{M}_{sk}\mathbf{b}_p) \\
&\quad +\int_{t_0}^{t} e^{\alpha_k(t-\tau)}\sin((\omega_k+\omega_p)\tau-\omega_k t)d\tau(\frac{1}{2}B_p\mathbf{M}_{ck}\mathbf{b}_p+\frac{1}{2}A_p\mathbf{M}_{sk}\mathbf{b}_p)
\end{aligned} \tag{A.4}$$

where

$$\begin{aligned}
A_p &= \cos(\phi_p) \\
B_p &= -\sin(\phi_p)
\end{aligned}$$

Appendix B

Parameter Values of Power Converter Systems

V_d	V_o	f_s	L	C_o	R_{load}	r_l	r_{co}	m_{sc}	r'_s
8 V	3 V	80 kHz	5 μH	2000 μF	200 mΩ	20 mΩ	10 mΩ	420 kV/s	0.1 Ω

Table B.1. Parameter values for the buck converter in Chapter 4.

V_d	V_o	f_s	R_{load}	r'_s
46 V	15 V	50 kHz	4.89 Ω	0.1 Ω

Table B.2. Parameter values for the buck converter for design optimization.

V_d	V_o	f_s	R_{load}	r'_s
24 V	46 V	50 kHz	23 Ω	0.45 Ω

Table B.3. Parameter values for the boost converter for design optimization.

V_d	V_o	f_s	R_{load}	r'_s
20 V	18 V	50 kHz	18 Ω	0.32 Ω

Table B.4. Parameter values for the buck-boost converter for design optimization.

Appendix C

Transfer Functions of Current-mode Controlled dc-to-dc Converter

C.1 Transfer Function of Current-mode Control for Boost Converter

The control-to-output transfer function [117] is

$$\frac{v_o(s)}{v_c(s)} = \frac{R_{load}D'}{r'_s K_D} \cdot \frac{(1-\frac{s}{\omega_R})\cdot(1+\frac{s}{\omega_z})}{(1+\frac{s}{\omega_p})\cdot(1+\frac{s}{\omega_n\cdot Q}+\frac{s^2}{\omega_n^2})}$$

where

$$\begin{aligned}
K_D &= 1+\frac{R_{load}}{Z_o}+\frac{R_{load}D'^2}{r'_s}\left(\frac{1}{K_m}+\frac{K}{D'}\right)\\
K_m &= \frac{1}{(0.5-D)r'_s\frac{T_s}{L}+\frac{V_{sc}}{V_o}}\\
K &= \frac{1}{2}\frac{T_s}{L}r'_s DD'\\
\omega_R &= \frac{R\cdot D'^2}{L}\\
\omega_z &= \frac{1}{C_o\cdot r_c}\\
\omega_p &= \frac{K_D}{C_o\cdot R_{load}}
\end{aligned}$$

$$\begin{aligned} \omega_n &= \frac{D'}{\sqrt{LC}} \\ Q &= D' R_{load} \sqrt{\frac{C}{L}}. \end{aligned}$$

C.2 Transfer Function of Current-mode Control for Buck-Boost Converter

The control-to-output transfer function [117] is

$$\frac{v_o(s)}{v_c(s)} = \frac{R_{load} D'}{r'_s K_D} \cdot \frac{(1 - \frac{s}{\omega_R}) \cdot (1 + \frac{s}{\omega_z})}{(1 + \frac{s}{\omega_p}) \cdot (1 + \frac{s}{\omega_n \cdot Q} + \frac{s^2}{\omega_n^2})}$$

where

$$\begin{aligned} K_D &= 1 + \frac{R_{load} D}{Z_o} + \frac{R_{load} D'^2}{r'_s} \left(\frac{1}{K_m} + \frac{K}{D'} \right) \\ K_m &= \frac{1}{(0.5 - D) r'_s \frac{T_s}{L} + \frac{V_{sc}}{V_o}} \\ K &= \frac{1}{2} \frac{T_s}{L} r'_s D D' \\ \omega_R &= \frac{R \cdot D'^2}{L \cdot D} \\ \omega_z &= \frac{1}{C_o \cdot r_c} \\ \omega_p &= \frac{K_D}{C_o \cdot R_{load}} \\ \omega_n &= \frac{D'}{\sqrt{LC}} \\ Q &= D' R_{load} \sqrt{\frac{C}{L}}. \end{aligned}$$

Appendix D

Inductor Core and Capacitor Data

Core Type	Volume (cm^3)	A_L (nH/N^2)	B_s (T)	Window Area (cm^2)
0F40301TC	11.94	495	0.47	0.02
0R40301TC	11.94	380	0.47	0.02
0F40401TC	23.27	570	0.47	0.04
0F40502TC	15.48	440	0.47	0.03
0C40502TC	15.48	129	0.38	0.03

Table C 1. Inductor core data from Magnetics [118].

Capacitor Type	Capacitance (F)	Volume (in^3)	*df*	ESR (Ω)
116ELL10	$C \leq 1 \times 10^{-5}$	0.0354	0.06	—
116RLL22	$1 \times 10^{-5} < C \leq 2.2 \times 10^{-5}$	0.0132	0.06	—
136RVI47	$2.2 \times 10^{-5} < C \leq 4.7 \times 10^{-5}$	0.0575	0.1	—
136RVI68	$4.7 \times 10^{-5} < C \leq 6.8 \times 10^{-5}$	0.0767	0.1	—
136RVI120	$6.8 \times 10^{-5} < C \leq 1.2 \times 10^{-4}$	0.0959	0.1	—
136RVI150	$1.2 \times 10^{-4} < C \leq 1.5 \times 10^{-4}$	0.1198	0.1	—
136RVI180	$1.5 \times 10^{-4} < C \leq 1.8 \times 10^{-4}$	0.1438	0.1	—
136RVI270	$1.8 \times 10^{-4} < C \leq 2.7 \times 10^{-4}$	0.1872	0.1	—
136RVI330	$2.7 \times 10^{-4} < C \leq 3.3 \times 10^{-4}$	0.2454	0.1	—
136RVI390	$3.3 \times 10^{-4} < C \leq 3.9 \times 10^{-4}$	0.2321	0.1	—
136RVI470	$3.9 \times 10^{-4} < C \leq 4.7 \times 10^{-4}$	0.3067	0.1	—
136RVI680	$4.7 \times 10^{-4} < C \leq 6.8 \times 10^{-4}$	0.3804	0.1	—
136RVI820	$6.8 \times 10^{-4} < C \leq 8.2 \times 10^{-4}$	0.4294	0.1	—
136RVI1000	$8.2 \times 10^{-4} < C \leq 1 \times 10^{-3}$	0.4814	0.1	—
052PED1500	$1 \times 10^{-3} < C \leq 1.5 \times 10^{-3}$	1.1982	—	8.3×10^{-2}
052PED2200	$1.5 \times 10^{-3} < C \leq 2.2 \times 10^{-3}$	1.7254	—	5.7×10^{-2}
052PED3300	$2.2 \times 10^{-3} < C \leq 3.3 \times 10^{-3}$	2.3485	—	4.8×10^{-2}
052PED4700	$3.3 \times 10^{-3} < C \leq 4.7 \times 10^{-3}$	2.9356	—	3.6×10^{-2}
052PED6800	$4.7 \times 10^{-3} < C \leq 6.8 \times 10^{-3}$	3.8342	—	3.5×10^{-2}
052PED10000	$6.8 \times 10^{-3} < C \leq 1 \times 10^{-2}$	5.3679	—	2.5×10^{-2}
052PED15000	$1 \times 10^{-2} < C \leq 1.5 \times 10^{-2}$	7.6684	—	1.8×10^{-2}

Table C 2. Capacitor data from Vishay (voltage rating $V_r = 63$V) [119].

Appendix E

Switched State Space Model of Power Converter Systems

E.1 Switched State Space Model of Buck Converter Systems with Input Filter

For generality, assume that the power stage operates in DCM. Choose state vector $\mathbf{x}_p = [i_L \quad v_c \quad i_{li} \quad v_{ci}]^T$ and input vector $\mathbf{u}_p = [V_d]$, then the buck converter with an input filter is described by piecewise-LTI model.

$$\begin{aligned} \dot{\mathbf{x}}_p &= \mathbf{A}_{pm}\mathbf{x}_p + \mathbf{B}_{pm}\mathbf{u}_p \\ \mathbf{y}_p &= \mathbf{C}_p\mathbf{x}_p + \mathbf{D}_p\mathbf{u}_p \end{aligned} \tag{E.1}$$

where $m \in \{1, 2, 3\}$ is the topology index, and $\mathbf{A}_{pm}$ and $\mathbf{B}_{pm}$ are the state matrices and control matrices for the m^{th} circuit topology. The input vector $\mathbf{u}_p$ and output vector $\mathbf{y}_p$ are assumed to be independent of topology. The matrices $\mathbf{A}_{pm}$, $\mathbf{B}_{pm}$, $\mathbf{C}_p$, and $\mathbf{D}_p$ are expressed as:

$$\mathbf{A}_{p1} = \begin{bmatrix} \frac{1}{L}\left(\frac{R_{load}^2}{r_{co}+R_{load}} - r_{lo} - R_{load} - r_{ci}\right) & -\frac{R_{load}}{L(r_{co}+R_{load})} & \frac{r_{ci}}{L} & \frac{1}{L} \\ \frac{R_{load}}{r_{co}C_o+R_{load}C_o} & -\frac{1}{r_{co}C_o+R_{load}C_o} & 0 & 0 \\ \frac{r_{ci}}{L_i} & 0 & -\frac{r_{li}+r_{ci}}{L_i} & -\frac{1}{L_i} \\ -\frac{1}{C_i} & 0 & \frac{1}{C_i} & 0 \end{bmatrix}$$

$$\mathbf{A}_{p2} = \begin{bmatrix} -\frac{R_{load}r_{co}+R_{load}r_{lo}+r_{co}r_{lo}}{L(R_{load}+r_{co})} & -\frac{R_{load}}{L(R_{load}+r_{co})} & 0 & 0 \\ \frac{R_{load}}{C_o(R_{load}+r_{co})} & -\frac{1}{C_o(R_{load}+r_{co})} & 0 & 0 \\ 0 & 0 & -\frac{r_{li}+r_{ci}}{L_i} & -\frac{1}{L_i} \\ -\frac{1}{C_i} & 0 & \frac{1}{C_i} & 0 \end{bmatrix}$$

$$\mathbf{A}_{p3} = \begin{bmatrix} 0 & 0 & 0 & 0 \\ \frac{R_{load}}{C_o(R_{load}+r_{co})} & -\frac{1}{C_o(R_{load}+r_{co})} & 0 & 0 \\ 0 & 0 & -\frac{r_{li}+r_{ci}}{L_i} & -\frac{1}{L_i} \\ -\frac{1}{C_i} & 0 & \frac{1}{C_i} & 0 \end{bmatrix}$$

$$\mathbf{B}_{p1} = \begin{bmatrix} 0 \\ 0 \\ \frac{1}{L_i} \\ 0 \end{bmatrix} \qquad \mathbf{B}_{p2} = \begin{bmatrix} 0 \\ 0 \\ \frac{1}{L_i} \\ 0 \end{bmatrix} \qquad \mathbf{B}_{p3} = \begin{bmatrix} 0 \\ 0 \\ \frac{1}{L_i} \\ 0 \end{bmatrix}$$

$$\mathbf{C}_p = \frac{R_{load}}{r_{co}+R_{load}} \begin{bmatrix} r_{co} & 1 & 0 & 0 \end{bmatrix} \qquad \mathbf{D}_p = 0$$

The phase-lead/lag compensator takes the difference between the reference output voltage v_o^{ref} and the actual output voltage v_o to generate a control signal v_c. Its zero is designed to cancel the pole of the power stage. The pole is located at 0.001 so that its performance is close to a practical integrator and the phase lag compensator behaves like a PI controller. Define the compensator state as $\mathbf{x}_c = [x_{ctr}]$ and input vector as $u_c = v_o^{ref} - v_o$, then the compensator is modeled as follows:

$$\dot{\mathbf{x}}_c = \mathbf{A}_c\mathbf{x}_c + \mathbf{B}_c v_o^{ref} - \mathbf{B}_c\mathbf{C}_p\mathbf{x}_p$$
$$v_c = \mathbf{C}_c\mathbf{x}_c + \mathbf{D}_c v_o^{ref} - \mathbf{D}_c\mathbf{C}_p\mathbf{x}_p$$

where $\mathbf{A}_c = [-0.001]$, $\mathbf{B}_c = [1]$, $\mathbf{C}_c = [K_c w_{zc}]$, and $\mathbf{D}_c = [K_c]$ are state space matrices of the compensator.

E.1.1 Closed-loop Piecewise-LTI Model

The overall close-loop system is modeled in the form of piecewise-LTI model by choosing state $\mathbf{x} = [i_L \quad v_{co} \quad i_{li} \quad v_{ci} \quad \mathbf{x}_c^T]^T$, input $\mathbf{u} = [V_d \quad V_o^{ref}]^T$, and output

$\mathbf{y} = [v_o \quad i_L \quad v_{co} \quad i_{li} \quad v_{ci} \quad v_c \quad \mathbf{x}_c^T]^T$.

$$\begin{aligned} \dot{\mathbf{x}}(t) &= \mathbf{A}_m\mathbf{x}(t) + \mathbf{B}_m\mathbf{u}(t) \qquad (k + d_{m-1}^k)T \le t \le (k + d_m^k)T \\ \mathbf{y}(t) &= \mathbf{C}_m\mathbf{x}(t) + \mathbf{D}_m\mathbf{u}(t) \qquad 0 \le d_m^k \le 1 \qquad m = 1, 2, 3 \end{aligned}$$

where

$$\mathbf{A}_m = \begin{bmatrix} \mathbf{A}_{pm} & \mathbf{0} \\ -\mathbf{B}_c\mathbf{C}_p & \mathbf{A}_c \end{bmatrix}$$

$$\mathbf{B}_m = \begin{bmatrix} \mathbf{B}_{pm} & \mathbf{0} \\ \mathbf{0} & \mathbf{B}_c \end{bmatrix}$$

$$\mathbf{C} = \begin{bmatrix} \mathbf{C}_p & 0 \\ \mathbf{I}_{4\times4} & \mathbf{0}_{4\times1} \\ -\mathbf{D}_c\mathbf{C}_p & \mathbf{C}_c \\ \mathbf{0}_{1\times4} & 1 \end{bmatrix}$$

$$\mathbf{D} = \begin{bmatrix} \mathbf{0}_{5\times1} & \mathbf{0}_{5\times1} \\ \mathbf{0} & \mathbf{D}_c \\ 0 & 0 \end{bmatrix}$$

E.1.2 Switching Surfaces

There are four possible transitions among circuit topologies. The system can transit from on-state to off-state, from off-state to DCM, from off-state to next on-state, and from DCM to next on-state. Therefore, the switching surfaces are

$$\begin{aligned} \sigma_1 &= v_c - m_{sc}T_s d_1 - r_s' i_L \\ &= \left[\left[\begin{pmatrix} -r_s' & 0 & 0 & 0 \end{pmatrix} - \mathbf{D}_c\mathbf{C}_p \right] \quad \mathbf{C}_c \right] \mathbf{x} + \begin{bmatrix} 0 & \mathbf{D}_c \end{bmatrix} \mathbf{u} - m_{sc}T_s d_1 \\ \boldsymbol{\sigma}_2 &= \begin{bmatrix} 1 & 0 & 0 & 0 & 0 \\ 0 & 0 & 0 & 0 & 0 \end{bmatrix} \mathbf{x} + \begin{bmatrix} 0 & 0 \\ 0 & 0 \end{bmatrix} \mathbf{u} + \begin{bmatrix} 0 \\ -1 \end{bmatrix} d_2 + \begin{bmatrix} 0 \\ 1 \end{bmatrix} \\ \sigma_3 &= 1 - d_3 \end{aligned} \tag{E.2}$$

E.2 Switched State Space Model of Boost Converter Systems with Input Filter

For generality, assume that the power stage operates in DCM. Choose state vector $\mathbf{x}_p = [i_L \quad v_c \quad i_{li} \quad v_{ci}]^T$ and input vector $\mathbf{u}_p = [V_d]$, then the boost converter with an input filter is described by piecewise-LTI model.

$$\begin{aligned} \dot{\mathbf{x}}_p &= \mathbf{A}_{pm}\mathbf{x}_p + \mathbf{B}_{pm}\mathbf{u}_p \\ \mathbf{y}_p &= \mathbf{C}_{pm}\mathbf{x}_p + \mathbf{D}_{pm}\mathbf{u}_p \end{aligned} \tag{E.3}$$

where $m \in \{1, 2, 3\}$ is the topology index, and $\mathbf{A}_{pm}$ and $\mathbf{B}_{pm}$ are the state matrices and control matrices for the m^{th} circuit topology. The input vector $\mathbf{u}_p$ and output vector $\mathbf{y}_p$ are assumed to be independent of topology. The matrices $\mathbf{A}_{pm}$, $\mathbf{B}_{pm}$, $\mathbf{C}_{pm}$, and $\mathbf{D}_{pm}$ are expressed as:

$$\mathbf{A}_{p1} = \begin{bmatrix} -\frac{r_{ci}+r_L}{L} & 0 & \frac{r_{ci}}{L} & \frac{1}{L} \\ 0 & -\frac{1}{r_{co}C_o+R_{load}C_o} & 0 & 0 \\ \frac{r_{ci}}{L_i} & 0 & -\frac{r_{li}+r_{ci}}{L_i} & -\frac{1}{L_i} \\ -\frac{1}{C_i} & 0 & \frac{1}{C_i} & 0 \end{bmatrix}$$

$$\mathbf{A}_{p2} = \begin{bmatrix} \frac{1}{L}(\frac{R_{load}^2}{r_{co}+R_{load}} - r_{lo} - R_{load} - r_{ci}) & -\frac{R_{load}}{L(r_{co}+R_{load})} & \frac{r_{ci}}{L} & \frac{1}{L} \\ \frac{R_{load}}{r_{co}C_o+R_{load}C_o} & -\frac{1}{r_{co}C_o+R_{load}C_o} & 0 & 0 \\ \frac{r_{ci}}{L_i} & 0 & -\frac{r_{li}+r_{ci}}{L_i} & -\frac{1}{L_i} \\ -\frac{1}{C_i} & 0 & \frac{1}{C_i} & 0 \end{bmatrix}$$

$$\mathbf{A}_{p3} = \begin{bmatrix} 0 & 0 & 0 & 0 \\ 0 & -\frac{1}{C_o(R_{load}+r_{co})} & 0 & 0 \\ 0 & 0 & -\frac{r_{li}+r_{ci}}{L_i} & -\frac{1}{L_i} \\ 0 & 0 & \frac{1}{C_i} & 0 \end{bmatrix}$$

$$\mathbf{B}_{p1} = \begin{bmatrix} 0 \\ 0 \\ \frac{1}{L_i} \\ 0 \end{bmatrix} \qquad \mathbf{B}_{p2} = \begin{bmatrix} 0 \\ 0 \\ \frac{1}{L_i} \\ 0 \end{bmatrix} \qquad \mathbf{B}_{p3} = \begin{bmatrix} 0 \\ 0 \\ \frac{1}{L_i} \\ 0 \end{bmatrix}$$

$$\mathbf{C}_{p_1} = \frac{R_{load}}{r_{co} + R_{load}} \begin{bmatrix} 0 & 1 & 0 & 0 \end{bmatrix}$$

$$\mathbf{C}_{p_2} = \frac{R_{load}}{r_{co} + R_{load}} \begin{bmatrix} r_{co} & 1 & 0 & 0 \end{bmatrix}$$

$$\mathbf{C}_{p_3} = \frac{R_{load}}{r_{co} + R_{load}} \begin{bmatrix} 0 & 1 & 0 & 0 \end{bmatrix}$$

$$\mathbf{D}_p = 0$$

The Type II compensator takes the difference between the reference output voltage v_o^{ref} and the actual output voltage v_o to generate a control signal v_c. Define the compensator state as $\mathbf{x}_c = \begin{bmatrix} x_{ctr1} & x_{ctr2} \end{bmatrix}^T$ and input vector as $u_c = v_o^{ref} - v_o$, then the compensator is modeled as :

$$\begin{aligned} \dot{\mathbf{x}}_c &= \mathbf{A}_c\mathbf{x}_c + \mathbf{B}_c v_o^{ref} - \mathbf{B}_c\mathbf{C}_p\mathbf{x}_p \\ v_c &= \mathbf{C}_c\mathbf{x}_c + \mathbf{D}_c v_o^{ref} - \mathbf{D}_c\mathbf{C}_p\mathbf{x}_p \end{aligned}$$

where $\mathbf{A}_c = \begin{bmatrix} -w_{pc1} & -w_{pc2} \\ 1 & 0 \end{bmatrix}$, $\mathbf{B}_c = \begin{bmatrix} 1 \\ 0 \end{bmatrix}$, $\mathbf{C}_c = \begin{bmatrix} 1 & K_c w_{zc} \end{bmatrix}$, and $\mathbf{D}_c = 0$ are state space matrices of the compensator.

E.2.1 Closed-loop Piecewise-LTI Model

The overall close-loop system is modeled in the form of piecewise-LTI Model by choosing state $\mathbf{x} = [i_L \quad v_{co} \quad i_{li} \quad v_{ci} \quad \mathbf{x}_c^T]^T$, input $\mathbf{u} = [V_d \quad V_o^{ref}]^T$, and output $\mathbf{y} = [v_o \quad i_L \quad v_{co} \quad i_{li} \quad v_{ci} \quad v_c \quad \mathbf{x}_c^T]^T$.

$$\begin{aligned} \dot{\mathbf{x}}(t) &= \mathbf{A}_m\mathbf{x}(t) + \mathbf{B}_m\mathbf{u}(t) \qquad (k + d_{m-1}^k)T \le t \le (k + d_m^k)T \\ \mathbf{y}(t) &= \mathbf{C}_m\mathbf{x}(t) + \mathbf{D}_m\mathbf{u}(t) \qquad 0 \le d_m^k \le 1 \qquad m = 1, 2, 3 \end{aligned}$$

where

$$\mathbf{A}_m = \begin{bmatrix} \mathbf{A}_{pm} & \mathbf{0} \\ -\mathbf{B}_c\mathbf{C}_{pm} & \mathbf{A}_c \end{bmatrix}$$

$$\mathbf{B}_m = \begin{bmatrix} \mathbf{B}_{pm} & \mathbf{0} \\ \mathbf{0} & \mathbf{B}_c \end{bmatrix}$$

$$\mathbf{C}_m = \begin{bmatrix} \mathbf{C}_{pm} & \mathbf{0}_{1\times 2} \\ \mathbf{I}_{4\times 4} & \mathbf{0}_{4\times 2} \\ -\mathbf{D}_c\mathbf{C}_{pm} & \mathbf{C}_c \\ \mathbf{0}_{2\times 4} & \mathbf{I}_{2\times 2} \end{bmatrix}$$

$$\mathbf{D}_m = \begin{bmatrix} \mathbf{0}_{5\times 1} & \mathbf{0}_{5\times 1} \\ \mathbf{0} & \mathbf{D}_c \\ \mathbf{0}_{2\times 1} & \mathbf{0}_{2\times 1} \end{bmatrix}$$

E.2.2 Switching Surfaces

There are four possible transitions among circuit topologies. The system can transit from on-state to off-state, from off-state to DCM, from off-state to next on-state, and from DCM to next on-state. Therefore, the switching surfaces are the same as buck converter systems and defined:

$$\begin{aligned} \sigma_1 &= v_c - m_{sc}T_s d_1 - r_s' i_L \\ &= \left[\left[\begin{pmatrix} -r_s' & 0 & 0 & 0 \end{pmatrix} - \mathbf{D}_c\mathbf{C}_{p1} \right] \quad \mathbf{C}_c \right] \mathbf{x} + \begin{bmatrix} 0 & \mathbf{D}_c \end{bmatrix} \mathbf{u} - m_{sc}T_s d_1 \\ \boldsymbol{\sigma}_2 &= \begin{bmatrix} 1 & 0 & 0 & 0 & 0 & 0 \\ 0 & 0 & 0 & 0 & 0 & 0 \end{bmatrix} \mathbf{x} + \begin{bmatrix} 0 & 0 \\ 0 & 0 \end{bmatrix} \mathbf{u} + \begin{bmatrix} 0 \\ -1 \end{bmatrix} d_2 + \begin{bmatrix} 0 \\ 1 \end{bmatrix} \\ \sigma_3 &= 1 - d_3 \end{aligned} \tag{E.4}$$

E.3 Switched State Space Model of Buck-Boost Converter Systems with Input Filter

For generality, assume that the power stage operates in DCM. Choose state vector $\mathbf{x}_p = [i_L \quad v_c \quad i_{li} \quad v_{ci}]^T$ and input vector $\mathbf{u}_p = [V_d]$, then the buck-boost converter

with an input filter is described by piecewise-LTI model.

$$\begin{aligned} \dot{\mathbf{x}}_p &= \mathbf{A}_{pm}\mathbf{x}_p + \mathbf{B}_{pm}\mathbf{u}_p \\ \mathbf{y}_p &= \mathbf{C}_{pm}\mathbf{x}_p + \mathbf{D}_{pm}\mathbf{u}_p \end{aligned} \tag{E.5}$$

where $m \in \{1, 2, 3\}$ is the topology index, and $\mathbf{A}_{pm}$ and $\mathbf{B}_{pm}$ are the state matrices and control matrices for the m^{th} circuit topology. The input vector $\mathbf{u}_p$ and output vector $\mathbf{y}_p$ are assumed to be independent of topology. The matrices $\mathbf{A}_{pm}$, $\mathbf{B}_{pm}$, $\mathbf{C}_{pm}$, and $\mathbf{D}_{pm}$ are expressed as:

$$\mathbf{A}_{p1} = \begin{bmatrix} -\frac{r_{ci}+r_L}{L} & 0 & \frac{r_{ci}}{L} & \frac{1}{L} \\ 0 & -\frac{1}{r_{co}C_o+R_{load}C_o} & 0 & 0 \\ \frac{r_{ci}}{L_i} & 0 & -\frac{r_{li}+r_{ci}}{L_i} & -\frac{1}{L_i} \\ -\frac{1}{C_i} & 0 & \frac{1}{C_i} & 0 \end{bmatrix}$$

$$\mathbf{A}_{p2} = \begin{bmatrix} -\frac{r_{co}R_{load}+r_LR_{load}+r_LR_{co}}{L(R_{load}+r_{co})} & -\frac{R_{load}}{L(r_{co}+R_{load})} & 0 & 0 \\ \frac{R_{load}}{r_{co}C_o+R_{load}C_o} & -\frac{1}{r_{co}C_o+R_{load}C_o} & 0 & 0 \\ 0 & 0 & -\frac{r_{li}+r_{ci}}{L_i} & -\frac{1}{L_i} \\ 0 & 0 & \frac{1}{C_i} & 0 \end{bmatrix}$$

$$\mathbf{A}_{p3} = \begin{bmatrix} 0 & 0 & 0 & 0 \\ 0 & -\frac{1}{C_o(R_{load}+r_{co})} & 0 & 0 \\ 0 & 0 & -\frac{r_{li}+r_{ci}}{L_i} & -\frac{1}{L_i} \\ 0 & 0 & \frac{1}{C_i} & 0 \end{bmatrix}$$

$$\mathbf{B}_{p1} = \begin{bmatrix} 0 \\ 0 \\ \frac{1}{L_i} \\ 0 \end{bmatrix} \qquad \mathbf{B}_{p2} = \begin{bmatrix} 0 \\ 0 \\ \frac{1}{L_i} \\ 0 \end{bmatrix} \qquad \mathbf{B}_{p3} = \begin{bmatrix} 0 \\ 0 \\ \frac{1}{L_i} \\ 0 \end{bmatrix}$$

$$\mathbf{C}_{p_1} = \frac{R_{load}}{r_{co}+R_{load}} \begin{bmatrix} 0 & 1 & 0 & 0 \end{bmatrix}$$

$$\mathbf{C}_{p_2} = \frac{R_{load}}{r_{co}+R_{load}} \begin{bmatrix} r_{co} & 1 & 0 & 0 \end{bmatrix}$$

$$\mathbf{C}_{p_3} = \frac{R_{load}}{r_{co} + R_{load}} \begin{bmatrix} 0 & 1 & 0 & 0 \end{bmatrix}$$

$$\mathbf{D}_p = 0$$

The Type II compensator takes the difference between the reference output voltage v_o^{ref} and the actual output voltage v_o to generate a control signal v_c. Define the compensator state as $\mathbf{x}_c = \begin{bmatrix} x_{ctr1} & x_{ctr2} \end{bmatrix}^T$ and input vector as $u_c = v_o^{ref} - v_o$, then the compensator is modeled as :

$$\dot{\mathbf{x}}_c = \mathbf{A}_c\mathbf{x}_c + \mathbf{B}_c v_o^{ref} - \mathbf{B}_c\mathbf{C}_p\mathbf{x}_p$$
$$v_c = \mathbf{C}_c\mathbf{x}_c + \mathbf{D}_c v_o^{ref} - \mathbf{D}_c\mathbf{C}_p\mathbf{x}_p$$

where $\mathbf{A}_c = \begin{bmatrix} -w_{pc1} & -w_{pc2} \\ 1 & 0 \end{bmatrix}$, $\mathbf{B}_c = \begin{bmatrix} 1 \\ 0 \end{bmatrix}$, $\mathbf{C}_c = \begin{bmatrix} 1 & K_c w_{zc} \end{bmatrix}$, and $\mathbf{D}_c = 0$ are state space matrices of the compensator.

E.3.1 Closed-loop Piecewise-LTI Model

The overall close-loop system is modeled in the form of piecewise-LTI Model by choosing state $\mathbf{x} = [i_L \quad v_{co} \quad i_{li} \quad v_{ci} \quad \mathbf{x}_c^T]^T$, input $\mathbf{u} = [V_d \quad V_o^{ref}]^T$, and output $\mathbf{y} = [v_o \quad i_L \quad v_{co} \quad i_{li} \quad v_{ci} \quad v_c \quad \mathbf{x}_c^T]^T$.

$$\dot{\mathbf{x}}(t) = \mathbf{A}_m\mathbf{x}(t) + \mathbf{B}_m\mathbf{u}(t) \qquad (k + d_{m-1}^k)T \le t \le (k + d_m^k)T$$
$$\mathbf{y}(t) = \mathbf{C}_m\mathbf{x}(t) + \mathbf{D}_m\mathbf{u}(t) \qquad 0 \le d_m^k \le 1 \qquad m = 1, 2, 3$$

where

$$\mathbf{A}_m = \begin{bmatrix} \mathbf{A}_{pm} & \mathbf{0} \\ -\mathbf{B}_c\mathbf{C}_{pm} & \mathbf{A}_c \end{bmatrix}$$

$$\mathbf{B}_m = \begin{bmatrix} \mathbf{B}_{pm} & \mathbf{0} \\ \mathbf{0} & \mathbf{B}_c \end{bmatrix}$$

$$\mathbf{C}_m = \begin{bmatrix} \mathbf{C}_{pm} & \mathbf{0}_{1\times 2} \\ \mathbf{I}_{4\times 4} & \mathbf{0}_{4\times 2} \\ -\mathbf{D}_c\mathbf{C}_{pm} & \mathbf{C}_c \\ \mathbf{0}_{2\times 4} & \mathbf{I}_{2\times 2} \end{bmatrix}$$

$$\mathbf{D}_m = \begin{bmatrix} \mathbf{0}_{5\times 1} & \mathbf{0}_{5\times 1} \\ \mathbf{0} & \mathbf{D}_c \\ \mathbf{0}_{2\times 1} & \mathbf{0}_{2\times 1} \end{bmatrix}$$

E.3.2 Switching Surfaces

There are four possible transitions among circuit topologies. The system can transit from on-state to off-state, from off-state to DCM, from off-state to next on-state, and from DCM to next on-state. The switching surfaces are the same as boost converter systems and defined as equation (E.4).

Bibliography

[1] R. B. Ridley, "A new, continuous-time model for current-mode control power convertors," *Power Electronics, IEEE Transactions on*, vol. 6, no. 2, pp. 271–280, 1991.

[2] B. Holland, "Modeling, analysis and compensation of the current-mode converter," 1984.

[3] R. D. Middlebrook, "Topics in multiple-loop regulators and current-mode programming," *Power Electronics, IEEE Transactions on*, vol. PE-2, no. 2, pp. 109–124, 1987.

[4] D. J. Perreault and G. C. Verghese, "Time-varying effects and averaging issues in models for current-mode control," *Power Electronics, IEEE Transactions on*, vol. 12, no. 3, pp. 453–461, 1997.

[5] R. Tymerski, "Application of the time varying transfer function for exact small-signal analysis," in *Power Electronics Specialists Conference, 1991. PESC '91 Record., 22nd Annual IEEE*, pp. 80–87.

[6] H. Y. Cho and E. Santi, "Peak-current-mode-controlled buck converter with positive feedforward control," in *Energy Conversion Congress and Exposition, 2009. ECCE 2009. IEEE*, pp. 2928–2935.

[7] M. Karppanen, M. Hankaniemi, T. Suntio, and M. Sippola, "Dynamical characterization of peak-current-mode-controlled buck converter with output-current feedforward," *Power Electronics, IEEE Transactions on*, vol. 22, no. 2, pp. 444–451, 2007.

[8] N. Kondrath and M. K. Kazimierczuk, "Control-to-output and duty ratio-to-inductor current transfer functions of peak current-mode controlled dc-dc pwm buck converter in ccm," in *Circuits and Systems (ISCAS), Proceedings of 2010 IEEE International Symposium on*, pp. 2734–2737.

[9] M. K. Kazimierczuk, "Transfer function of current modulator in pwm converters with current-mode control," *Circuits and Systems I: Fundamental Theory and Applications, IEEE Transactions on*, vol. 47, no. 9, pp. 1407–1412, 2000.

[10] F. C. Lee and Y. Yu, "An adaptive-control switching buck regulator-implementation, analysis and design," in *Power Electronics Specialists Conference, 1979 IEEE*, pp. 359–373.

[11] F. H. F. Leung, P. K. S. Tam, and C. K. Li, "An improved lqr-based controller for switching dc-dc converters," *Industrial Electronics, IEEE Transactions on*, vol. 40, no. 5, pp. 521–528, 1993.

[12] Y. Zaohong and P. C. Sen, "Dc-to-dc buck converters with novel current mode control," in *Power Electronics Specialists Conference, 1999. PESC 99. 30th Annual IEEE*, vol. 2, pp. 1158–1164 vol.2.

[13] S. Chattopadhyay and S. Das, "A digital current-mode control technique for dc-dc converters," *Power Electronics, IEEE Transactions on*, vol. 21, no. 6, pp. 1718–1726, 2006.

[14] C. Jingquan, A. Prodic, R. W. Erickson, and D. Maksimovic, "Predictive digital current programmed control," *Power Electronics, IEEE Transactions on*, vol. 18, no. 1, pp. 411–419, 2003.

[15] C. Man Pun and P. K. T. Mok, "Design and implementation of fully integrated digitally controlled current-mode buck converter," *Circuits and Systems I: Regular Papers, IEEE Transactions on*, vol. 58, no. 8, pp. 1980–1991, 2011.

[16] R. D. Middlebrook, "Input filter considerations in design and application of switching regulators," Oct. 11-14 1976.

[17] S. S. Kelkar and F. C. Lee, "Stability analysis of a buck regulator employing input filter compensation," *Aerospace and Electronic Systems, IEEE Transactions on*, vol. AES-20, no. 1, pp. 67–77, 1984.

[18] K. Dongsoo, C. Byungcho, L. Donggyu, and S. Jian, "Dynamics of current-mode-controlled dc-to-dc converters with input filter stage," in *Power Electronics Specialists Conference, 2005. PESC '05. IEEE 36th*, pp. 2648–2656.

[19] C. Byungcho, K. Dongsoo, L. Donggyu, C. Seungwon, and S. Jian, "Analysis of input filter interactions in switching power converters," *Power Electronics, IEEE Transactions on*, vol. 22, no. 2, pp. 452–460, 2007.

[20] T. Suntio, D. Gadoura, and Z. Kai, "Input filter interactions in peak-current-mode-controlled buck converter operating in cicm," *Industrial Electronics, IEEE Transactions on*, vol. 49, no. 1, pp. 76–86, 2002.

[21] M. Alfayyoumi, A. H. Nayfeh, and D. Borojevic, "Input filter interactions in dc-dc switching regulators," in *Power Electronics Specialists Conference, 1999. PESC 99. 30th Annual IEEE*, vol. 2, pp. 926–932 vol.2.

[22] C. R. Kohut, "Input filter design criteria for switching regulators using current-mode programming," *Power Electronics, IEEE Transactions on*, vol. 7, no. 3, pp. 469–479, 1992.

[23] S. Y. Erich and W. M. Polivka, "Input filter design criteria for current-programmed regulators," *Power Electronics, IEEE Transactions on*, vol. 7, no. 1, pp. 143–151, 1992.

[24] C. Shen-Yaur and C. Jin-Jia, "Study of the effect and design criteria of the input filter for buck converters with peak current-mode control using a novel system block diagram," *Industrial Electronics, IEEE Transactions on*, vol. 55, no. 8, pp. 3159–3166, 2008.

[25] F. C. Lee and Y. Yu, "Input-filter design for switching regulators," *Aerospace and Electronic Systems, IEEE Transactions on*, vol. AES-15, no. 5, pp. 627–634, 1979.

[26] J. Yungtaek and R. W. Erickson, "Physical origins of input filter oscillations in current programmed converters," *Power Electronics, IEEE Transactions on*, vol. 7, no. 4, pp. 725–733, 1992.

[27] M. U. Iftikhar, D. Sadarnac, and C. Karimi, "Input filter damping design for control loop stability of dc-dc converters," in *Industrial Electronics, 2007. ISIE 2007. IEEE International Symposium on*, pp. 353–358.

[28] P. A. Dahono, "A control method to damp oscillation in the input lc filter," in *Power Electronics Specialists Conference, 2002. pesc 02. 2002 IEEE 33rd Annual*, vol. 4, pp. 1630–1635.

[29] S. S. Kelkar and F. C. Lee, "A novel feedforward compensation canceling input filter-regulator i nteraction," *Aerospace and Electronic Systems, IEEE Transactions on*, vol. AES-19, no. 2, pp. 258–268, 1983.

[30] S. S. Kelkar and F. C. Lee, "Adaptive input filter compensation for switching regulators," *Aerospace and Electronic Systems, IEEE Transactions on*, vol. AES-20, no. 1, pp. 57–66, 1984.

[31] R. Weichel, W. Guanghui, J. Mayer, and H. Hofmann, "Active stabilization of dc-dc converters with input lc filters via current-mode control and input voltage feedback," in *Energy Conversion Congress and Exposition (ECCE), 2010 IEEE*, pp. 3409–3413.

[32] M. U. Iftikhar, E. Godoy, P. Lefranc, D. Sadarnac, and C. Karimi, "A control strategy to stabilize pwm dc-dc converters with input filters using state-feedback and pole-placement," in *Telecommunications Energy Conference, 2008. INTELEC 2008. IEEE 30th International*, pp. 1–5.

[33] S. Middlebrook, R. D.; Cuk, "A general unified approach to modelling switching-converter power stages," June 8-10 1976.

[34] R. D. Middlebrook, "Small-signal modeling of pulse-width modulated switched-mode power converters," *Proceedings of the IEEE*, vol. 76, no. 4, pp. 343–354, 1988.

[35] G. W. Wester and R. D. Middlebrook, "Low-frequency characterization of switched dc-dc converters," in *Power Electronics Specialists Conference, 1972 IEEE*, pp. 9–20.

[36] S. Jian, D. M. Mitchell, M. F. Greuel, P. T. Krein, and R. M. Bass, "Averaged modeling of pwm converters operating in discontinuous conduction mode," *Power Electronics, IEEE Transactions on*, vol. 16, no. 4, pp. 482–492, 2001.

[37] J. Mahdavi, A. Emaadi, M. D. Bellar, and M. Ehsani, "Analysis of power electronic converters using the generalized state-space averaging approach," *Circuits and Systems I: Fundamental Theory and Applications, IEEE Transactions on*, vol. 44, no. 8, pp. 767–770, 1997.

[38] A. Emadi, "Modelling and analysis of multi-converter dc power electronic systems using the generalized state space averaging method," in *Industrial Electronics Society, 2001. IECON '01. The 27th Annual Conference of the IEEE*, vol. 2, pp. 1001–1007 vol.2.

[39] A. C. Schittler, D. Pappis, C. Rech, A. Campos, and M. A. Dalla Costa, "Generalized state-space model for the interleaved buck converter," in *Power Electronics Conference (COBEP), 2011 Brazilian*, pp. 451–457.

[40] V. Vorperian, "Simplified analysis of pwm converters using model of pwm switch. continuous conduction mode," *Aerospace and Electronic Systems, IEEE Transactions on*, vol. 26, no. 3, pp. 490–496, 1990.

[41] V. Vorperian, "Simplified analysis of pwm converters using model of pwm switch. ii. discontinuous conduction mode," *Aerospace and Electronic Systems, IEEE Transactions on*, vol. 26, no. 3, pp. 497–505, 1990.

[42] F. D. Tan and R. D. Middlebrook, "A unified model for current-programmed converters," *Power Electronics, IEEE Transactions on*, vol. 10, no. 4, pp. 397–408, 1995.

[43] G. C. Verghese, C. A. Bruzos, and K. N. Mahabir, "Averaged and sampled-data models for current mode control: a re-examination," in *Power Electronics Specialists Conference, 1989. PESC '89 Record., 20th Annual IEEE*, pp. 484–491 vol.1.

[44] R. Tymerski and D. Li, "State space models for current programmed pulse width modulated converters," in *Power Electronics Specialists Conference, 1992. PESC '92 Record., 23rd Annual IEEE*, pp. 337–344 vol.1.

[45] J. G. Kassakian, M. F. Schlecht, and G. C. Verghese, *Principles of power electronics*. Reading, Mass.: Addison-Wesley, 1991.

[46] I. Dobson and S. Jalali, "Surprising simplification of the jacobian of diode switching circuits," in *Circuits and Systems, 1993., ISCAS '93, 1993 IEEE International Symposium on*, pp. 2652–2655.

[47] R. Rajaraman, I. Dobson, and S. G. Jalali, "Nonlinear dynamics and switching time bifurcations of a thyristor controlled reactor circuit," *Circuits and Systems I: Fundamental Theory and Applications, IEEE Transactions on*, vol. 43, no. 12, pp. 1001–1006, 1996.

[48] I. Dobson, "Stability of ideal thyristor and diode switching circuits," *Circuits and Systems I: Fundamental Theory and Applications, IEEE Transactions on*, vol. 42, no. 9, pp. 517–529, 1995.

[49] J. Dugundji and J. H. Wendell, "Some analysis methods for rotating systems with periodic coefficients," *AIAA Journal*, vol. 21, no. 6, pp. 890–897, 1983.

[50] S. G. Kriventsov and J. S. Mayer, "An exact expression for the input impedance of the buck converter in continuous conduction mode," in *Power Electronics Specialists Conference, 2001. PESC. 2001 IEEE 32nd Annual*, vol. 1, pp. 351–356 vol. 1.

[51] N. M. Wereley and S. R. Hall, "Frequency response of linear time periodic systems," in *Decision and Control, 1990., Proceedings of the 29th IEEE Conference on*, pp. 3650–3655 vol.6.

[52] P. H. Jan Awrejcewicz, *Nonlinearity, Bifurcation and Chaos - Theory and Applications*. InTech, 2012.

[53] J. A. Alvarez Martin, J. R. Melgoza, and J. J. Rincon Pasaye, "Exact steady state analysis in power converters using floquet decomposition," in *North American Power Symposium (NAPS), 2011*, pp. 1–7.

[54] L. Hong, S. Jianing, Y. Xiaojie, T. Zheng, Z. Bo, and L. Jinhu, "A novel stability analysis method based on floquet theory for cascaded dc-dc converters system," in *Energy Conversion Congress and Exposition (ECCE), 2015 IEEE*, pp. 2679–2683.

[55] S. K. Mazumder, A. H. Nayfeh, and D. Boroyevich, "Theoretical and experimental investigation of the fast- and slow-scale instabilities of a dc-dc converter," *Power Electronics, IEEE Transactions on*, vol. 16, no. 2, pp. 201–216, 2001.

[56] S. K. Mazumder, A. H. Nayfeh, and D. Borojevic, "Stability analysis of parallel dc-dc converters using a nonlinear approach," in *Power Electronics Specialists Conference, 2001. PESC. 2001 IEEE 32nd Annual*, vol. 3, pp. 1283–1288 vol. 3.

[57] W. Faqiang, Z. Hao, and M. Xikui, "Analysis of slow-scale instability in boost pfc converter using the method of harmonic balance and floquet theory," *Circuits and Systems I: Regular Papers, IEEE Transactions on*, vol. 57, no. 2, pp. 405–414, 2010.

[58] S. K. Mazumder, A. H. Nayfeh, and D. Boroyevich, "An investigation into the fast- and slow-scale instabilities of a single phase bidirectional boost converter," *Power Electronics, IEEE Transactions on*, vol. 18, no. 4, pp. 1063–1069, 2003.

[59] S. G. Kriventsov and J. S. Mayer, "Stability of periodic solutions for multitopology dc-to-dc power converters," in *Power Electronics Specialist Conference, 2003. PESC '03. 2003 IEEE 34th Annual*, vol. 4, pp. 1577–1582 vol.4.

[60] S. G. Kriventsov, *Nonlinear Techniques for Analysis of DC-DC Power Converter Systems*. PhD thesis, 2004.

[61] J. L. Rodriguez Marrero, J. M. Font, and G. C. Verghese, "Analysis of the chaotic regime for dc-dc converters under current-mode control," in *Power Electronics Specialists Conference, 1996. PESC '96 Record., 27th Annual IEEE*, vol. 2, pp. 1477–1483 vol.2.

[62] S. Bittanti, B. Sergio, and C. Patrizio, *Periodic Systems: Filtering and Control*. Communications and Control Engineering, Springer London, 2008.

[63] S. K. Mazumder, *Nonlinear Analysis and Control of Standalone, Parallel DC-DC, and Parallel Multi-Phase PWM Converters*. PhD thesis, 2001.

[64] T. Takayama and D. Maksimovic, "A power stage optimization method for monolithic dc-dc converters," in *Power Electronics Specialists Conference, 2006. PESC '06. 37th IEEE*, pp. 1–7.

[65] R. Yu, B. M. H. Pong, B. W. K. Ling, and J. Lam, "Two-stage optimization method for efficient power converter design including light load operation," *Power Electronics, IEEE Transactions on*, vol. 27, no. 3, pp. 1327–1337, 2012.

[66] E. Lefeuvre, D. Audigier, C. Richard, and D. Guyomar, "Buck-boost converter for sensorless power optimization of piezoelectric energy harvester," *Power Electronics, IEEE Transactions on*, vol. 22, no. 5, pp. 2018–2025, 2007.

[67] S. Balachandran and F. C. Y. Lee, "Algorithms for power converter design optimization," *Aerospace and Electronic Systems, IEEE Transactions on*, vol. AES-17, no. 3, pp. 422–432, 1981.

[68] R. B. Ridley, C. Zhou, and F. C. Y. Lee, "Application of nonlinear design optimization for power converter components," *Power Electronics, IEEE Transactions on*, vol. 5, no. 1, pp. 29–40, 1990.

[69] T. C. Neugebauer and D. J. Perreault, "Computer-aided optimization of dc/dc converters for automotive applications," in *Power Electronics Specialists Conference, 2000. PESC 00. 2000 IEEE 31st Annual*, vol. 2, pp. 689–695 vol.2.

[70] G. Sizikov, A. Kolodny, E. G. Fridman, and M. Zelikson, "Efficiency optimization of integrated dc-dc buck converters," in *Electronics, Circuits, and Systems (ICECS), 2010 17th IEEE International Conference on*, pp. 1208–1211.

[71] Z. Xunwei, T. G. Wang, and F. C. Lee, "Optimizing design for low voltage dc-dc converters," in *Applied Power Electronics Conference and Exposition, 1997. APEC '97 Conference Proceedings 1997., Twelfth Annual*, vol. 2, pp. 612–616 vol.2.

[72] A. De Nardo, N. Femia, G. Petrone, and G. Spagnuolo, "Optimal buck converter output filter design for point-of-load applications," *Industrial Electronics, IEEE Transactions on*, vol. 57, no. 4, pp. 1330–1341, 2010.

[73] R. Redl and N. O. Sokal, "Near-optimum dynamic regulation of dc-dc converters using feed-forward of output current and input voltage with current-mode control," *Power Electronics, IEEE Transactions on*, vol. PE-1, no. 3, pp. 181–192, 1986.

[74] R. Redl, B. P. Erisman, and Z. Zansky, "Optimizing the load transient response of the buck converter," in *Applied Power Electronics Conference and Exposition, 1998. APEC '98. Conference Proceedings 1998., Thirteenth Annual*, vol. 1, pp. 170–176 vol.1, 1998.

[75] L. Yu-Huei, W. Shih-Jung, H. Chun-Yu, and C. Ke-Horng, "Current mode dc-dc buck converters with optimal fast-transient control," in *Circuits and Systems, 2008. ISCAS 2008. IEEE International Symposium on*, pp. 3045–3048.

[76] Z. Yanlei, Z. Lei, and Z. Housheng, "Design on four-quadrant dc/ac converter for wind power flow optimization system," in *Power Engineering and Automation Conference (PEAM), 2011 IEEE*, vol. 1, pp. 179–182.

[77] F. Guang, E. Meyer, and L. Yan-Fei, "A new digital control algorithm to achieve optimal dynamic performance in dc-to-dc converters," *Power Electronics, IEEE Transactions on*, vol. 22, no. 4, pp. 1489–1498, 2007.

[78] A. DeNardo, N. Femia, G. Petrone, and G. Spagnuolo, "Optimal design of input filters for dc-dc switching regulator using ceramic and electrolytic capacitors," in *Electronics, Circuits and Systems, 2008. ICECS 2008. 15th IEEE International Conference on*, pp. 950–953.

[79] K. Raggl, T. Nussbaumer, and J. W. Kolar, "Model based optimization of emc input filters," in *Control and Modeling for Power Electronics, 2008. COMPEL 2008. 11th Workshop on*, pp. 1–6.

[80] S. A. Emami, M. B. Poudeh, and S. Eshtehardiha, "Particle swarm optimization for improved performance of pid controller on buck converter," in *Mechatronics and Automation, 2008. ICMA 2008. IEEE International Conference on*, pp. 520–524.

[81] S. Chonsatidjamroen, K.-N. Areerak, K.-L. Areerak, and A. Srikaew, "Optimized cascade pi controllers of buck converters using particle swarm optimization algorithm," 2012.

[82] H. Lou, C. Mao, J. Lu, D. Wang, and W. J. Lee, "Pulse width modulation ac/dc converters with line current harmonics minimisation and high power factor using hybrid particle swarm optimisation," *Power Electronics, IET*, vol. 2, no. 6, pp. 686–696, 2009.

[83] W. Anna, H. Zhanjun, L. Cui, C. Zhang, and W. Erlei, "Parameters optimization study and analysis of pid controller in buck converter based on fuzzy particle swarm optimization algorithm," in *Information Science, Electronics and Electrical Engineering (ISEEE), 2014 International Conference on*, vol. 3, pp. 1562–1566.

[84] A. F. Zobaa and A. Lecci, "Particle swarm optimisation of resonant controller parameters for power converters," *Power Electronics, IET*, vol. 4, no. 2, pp. 235–241, 2011.

[85] R. Hai-Peng and G. Xin, "Optimization controller design of caczvs three phase pfc converter using particle swarm optimization," in *Industrial Electronics Society, IECON 2014 - 40th Annual Conference of the IEEE*, pp. 1665–1671.

[86] N. Jiteurtragool, C. Wannaboon, and W. San-Um, "A power control system in dc-dc boost converter integrated with photovoltaic arrays using optimized back propagation artificial neural network," in *Knowledge and Smart Technology (KST), 2013 5th International Conference on*, pp. 107–112.

[87] I. Petrovic, M. Baric, A. Magzan, and N. Peric, "Application of a neural predictive controller in boost converter input current control," in *Intelligent Control, 2000. Proceedings of the 2000 IEEE International Symposium on*, pp. 327–332.

[88] A. F. Zobaa and A. Lecci, "Ant colony optimization of controller parameters for power converters," in *Advances in Power System Control, Operation and Management (APSCOM 2009), 8th International Conference on*, pp. 1–5.

[89] W. Anna, H. Zhanjun, L. Cui, C. Zhang, and W. Erlei, "Parameters optimization study and analysis of pid controller in buck converter based on fuzzy particle swarm optimization algorithm," in *Information Science, Electronics and Electrical Engineering (ISEEE), 2014 International Conference on*, vol. 3, pp. 1562–1566.

[90] V. Nivetha and G. V. Gowri, "Maximum power point tracking of photovoltaic system using ant colony and particle swam optimization algorithms," in *Electronics and Communication Systems (ICECS), 2015 2nd International Conference on*, pp. 948–952.

[91] L. Faa-Jeng, T. Li-Tao, L. Jeng-Wen, and C. Syuan-Yi, "Recurrent functional-link-based fuzzy-neural-network-controlled induction-generator system using improved particle swarm optimization," *Industrial Electronics, IEEE Transactions on*, vol. 56, no. 5, pp. 1557–1577, 2009.

[92] H. Helali, D. Bergogne, J. Ben Hadj Slama, H. Morel, P. Bevilacqua, B. Allard, and O. Brevet, "Power converter's optimisation and design. discrete cost function with genetic based algorithms," in *Power Electronics and Applications, 2005 European Conference on*, pp. 7 pp.–P.7.

[93] J. Baba and E. Masada, "Genetic algorithm based control for power converters," in *Power Conversion Conference - Nagaoka 1997., Proceedings of the*, vol. 1, pp. 463–466 vol.1.

[94] P. Zanchetta, M. Sumner, J. C. Clare, and P. W. Wheeler, "Control of matrix converters for ac power supplies using genetic algorithms," in *Industrial Electronics, 2004 IEEE International Symposium on*, vol. 2, pp. 1429–1433 vol. 2.

[95] P. Zanchetta, J. C. Clare, P. Wheeler, D. Katsis, M. Bland, and L. Empringham, "Control design of a three-phase matrix converter mobile ac power supply using genetic algorithms," in *Power Electronics Specialists Conference, 2005. PESC '05. IEEE 36th*, pp. 2370–2375.

[96] M. J. Schutten and D. A. Torrey, "Genetic algorithms for control of power converters," in *Power Electronics Specialists Conference, 1995. PESC '95 Record., 26th Annual IEEE*, vol. 2, pp. 1321–1326 vol.2.

[97] R. Hai Peng and Z. Ting, "Optimization design of power factor correction converter based on genetic algorithm," in *Genetic and Evolutionary Computing (ICGEC), 2010 Fourth International Conference on*, pp. 293–296.

[98] Y.-K. Choi and B.-W. Jung, "Parameter tuning for buck converters using genetic algorithms," 2007.

[99] N. Femia, P. Lamberti, G. Petrone, and G. Spagnuolo, "Selection criteria of closed-loop controllers for dc-dc voltage regulators based on nominal and tolerance design: genetic algorithm and vertex analysis based optimization," in *Industrial Electronics, 2002. ISIE 2002. Proceedings of the 2002 IEEE International Symposium on*, vol. 3, pp. 1015–1020 vol.3.

[100] D. V. Malyna, J. L. Duarte, M. A. M. Hendrix, and F. B. M. van Horck, "Multi-objective optimization of power converters using genetic algorithms," in *Power Electronics, Electrical Drives, Automation and Motion, 2006. SPEEDAM 2006. International Symposium on*, pp. 713–717.

[101] C. Versele, O. Deblecker, and J. Lobry, "Multiobjective optimal choice and design of isolated dc-dc power converters," in *Power Electronics and Applications (EPE 2011), Proceedings of the 2011-14th European Conference on*, pp. 1–10.

[102] M. B. poodeh, S. Eshtehardiha, A. Kiyoumarsi, and M. Ataei, "Optimizing lqr and pole placement to control buck converter by genetic algorithm," in *Control, Automation and Systems, 2007. ICCAS '07. International Conference on*, pp. 2195–2200.

[103] Z. Liang, C. Guodong, and C. Xu, "Optimization of inductor based on genetic algorithm for the medium voltage cascade converter with active front end," *International Review of Electrical Engineering*, vol. 6, no. 2, pp. 599–606, 2011.

[104] A. Y. Behzad Mirzaeian Dehkordi and S.-K. Sul, "Optimal design of a damped input filter based on a genetic algorithm for an electrolytic capacitorless converter," *Journal of Power Electronics*, vol. 9, no. 3, p. 12, 2009.

[105] A. Trentin, P. Zanchetta, J. Clare, and P. Wheeler, "Automated optimal design of input filters for direct ac/ac matrix converters," *Industrial Electronics, IEEE Transactions on*, vol. 59, no. 7, pp. 2811–2823, 2012.

[106] M. C. Joshi and K. M. Moudgalya, *Optimization: theory and practice*. Harrow: Alpha Science International Ltd, 2004.

[107] E. K. P. Chong and S. H. Zak, *An introduction to optimization*, vol. Fourthition. Hoboken, New Jersey: John Wiley and Sons, Inc, 2013.

[108] A. Astolfi, *Optimization: An Introduction*. Imperial College London, 2006.

[109] Y. Rahmat-Samii and E. Michielssen, *Electromagnetic Optimization by Genetic Algorithms*. Wiley, 1999.

[110] T. K. S. K. S. Man, Kim-Fung, *Genetic Algorithms Concepts and Designs*. Springer, 1999.

[111] D. H. W. Randy L. Haupt, *Genetic Algorithms in Electromagnetics*. Wiley, 2007.

[112] C. P. G. W. D. Quagliarella, Jacques Priaux, *Genetic Algorithms and Evolution Strategy in Engineering and Computer Science: Recent Advances and Industrial Applications*. Wiley, 1998.

[113] A. Eiben and J. E. Smith, *Introduction to Evolutionary Computing*. Natural Computing Series, Springer, 2003.

[114] D. Rowell and D. N. Wormley, *System Dynamics: An Introduction*. Pearson, 1996.

[115] G. Smith, "Designing toroidal inductors with dc bias," *NASA Technical Note*, vol. NASA TN-D2320, 1964.

[116] S. Lee, "Practical feedback loop analysis for current-mode boost converter," *Texas Instruments Application Report*, vol. SLVA636, 2014.

[117] R. Sheehan, "Understanding and applying current-mode control theory," *Texas Instruments Application Report*, vol. SNVA555, 2007.

[118] Magnetics, "Magnetics ferrite cores catalog," 2013.

[119] Vishay, "Vishay capacitor catalog 51 v to 100 v," http://www.vishay.com/capacitors/capacitance-1mf-greater/volt-51-100/.

Vita

Mu He

Mu He received his bachelor's degree in Automation from University of Science and Technology Beijing (China). Then he decided to continue his academic studies at Imperial College London (United Kingdom) and received his M.S. in Control Systems in 2008. He worked for Liaoning Wish Information Technology as an embedded system engineer from 2008 to 2010, where he was one of the primary engineers to design four-wheel-independent-drive electric vehicles and participated in the 2010 Beijing International Automotive Exhibition. In the fall of 2010, he joined the Pennsylvania State University and started his Doctoral career with specialization in Power Electronics. At Penn State, he was employed as a graduate assistant and received his Ph.D. in Electrical Engineering in 2016. With all his academic research and professional experience, his areas of expertise and interests include switched power converters, drive for permanent magnet synchronous motor and brushless DC motor, and embedded system design.